



UNIVERSITY OF THESSALY  
SCHOOL OF ENGINEERING  
DEPARTMENT OF MECHANICAL ENGINEERING  
Doctor of Philosophy Dissertation

**NUMERICAL SIMULATION OF JCO-E LINE PIPE  
MANUFACTURING AND ITS INFLUENCE ON THE MECHANICAL  
BEHAVIOR AND STRENGTH OF OFFSHORE PIPELINES**

by

**KONSTANTINOS ANTONIOU**

Diploma of Mechanical Engineering, University of Thessaly, 2016

Supervisor: Dr. Spyros A. Karamanos, Professor

Submitted in partial fulfillment  
of the requirements for the degree  
of Doctor of Philosophy

2021

© 2021 Konstantinos Antoniou

Approval of this doctoral thesis by the Department of Mechanical Engineering, School of Engineering, University of Thessaly, does not constitute in any way an acceptance of the views of the author by the said academic organization (L. 5343/32, art. 202, § 2).

## **Examination Committee:**

Dr. Spyros A. Karamanos (**Supervisor**)

Professor, Department of Mechanical Engineering, University of Thessaly

Dr. Gregory N. Haidemenopoulos

Professor, Department of Mechanical Engineering, University of Thessaly

Dr. Michalis Agoras

Assistant Professor, Department of Mechanical Engineering, University of Thessaly

Dr. Euripidis S. Mistakidis

Professor, Department of Civil Engineering, University of Thessaly

Dr. George-Christopher Vosniakos

Professor, School of Mechanical Engineering, National Technical University of Athens

Dr. Konstantinos V. Spiliopoulos

Professor, School of Civil Engineering, National Technical University of Athens

Dr. Stefanos Aldo Papanicolopoulos

Senior Lecturer, School of Engineering, University of Edinburgh

## **Acknowledgements**

I would first like to express my thanks and appreciation to my supervisor Dr. Spyros A. Karamanos of University of Thessaly, whose supervision during the completion of this thesis enabled me to develop an understanding of the subject. Also, I am grateful to the other members of the examination committee for their remarks. Special thanks to Giannoula Chatzopoulou, Gregory Sarvanis, Dimitris Fappas, Christos Prosgolitis, Nikos Vasileiadis for the scientific collaboration. A substantial part of this research was financially supported by Corinth Pipeworks S.A.; I offer my regards to Dr. Athanasios Tazedakis, Dr. Christos Palagkas and Dr. Efthymios Dourdounis for the close cooperation during the completion of the research. Last but not least, I would like to thank my friends and my family members. Thank you for your support and encouragement.

Konstantinos Antoniou

# **NUMERICAL SIMULATION OF JCO-E LINE PIPE MANUFACTURING AND ITS INFLUENCE ON THE MECHANICAL BEHAVIOR AND STRENGTH OF OFFSHORE PIPELINES**

KONSTANTINOS ANTONIOU

Department of Mechanical Engineering, University of Thessaly, 2021

Supervisor: Dr. Spyros A. Karamanos, Professor of Mechanical Engineering

## **Abstract**

Large-diameter pipelines are increasingly used in deep-water offshore applications. In this context, reliable predictions of the mechanical properties and the collapse pressure of the line pipe product constitute important challenges towards optimization of line pipe fabrication process. The JCO-E line pipe fabrication process, from a flat plate to a circular pipe, is a cost effective method regarding the required forming force tooling [1]. The present study focuses on the numerical modelling of JCO-E process, using information from the fabrication process directly from the pipe mill. The validity of the proposed numerical model is verified by comparing numerical results with actual measurements from JCO-E pipes. Following the modelling of manufacturing process, the collapse performance of as-fabricated JCO-E line pipe is investigated.

In the first part of the PhD thesis, the finite element simulation of JCO-E line pipe fabrication process is presented using a numerical model, developed for the purposes of the present study. The deformation and stresses induced by manufacturing process, namely the edge crimping, the JCO forming, the LSAW welding, and the expansion (E) operation are calculated utilizing finite element simulation tools. In addition to numerical modelling, strip specimens are extracted from the steel plate (raw material) and subjected to monotonic and cyclic uniaxial loading to measure the material properties. Using stress-strain curves obtained from the experiments, an efficient constitutive model is calibrated and incorporated in the finite element model, as a material user subroutine. The elastic-plastic behavior of the steel plate is described by a (combined) kinematic/isotropic hardening plasticity model, which can also take into account the anisotropy of plate. Once the numerical analysis of JCO-E process is completed, the predicted material properties of JCO-E pipe are compared with experimental results from strip specimens extracted from the final line pipe aimed at validation of the numerical model. Following the simulation of the fabrication process, and using the same finite element model, the analysis is continued, so that the mechanical response of JCO-E pipe

under external pressure is obtained, and its collapse pressure is calculated for different values of the manufacturing parameters.

Considering the parameters provided by Corinth Pipeworks S.A., the above methodology is applied on the JCO-E process of (a) a 26-inch-diameter X65 “relatively thin-walled” line pipe and (b) a 30-inch-diameter X60 “thick-walled” line pipe, which are candidates for offshore pipeline applications. The first pipe is used in moderately deep water applications, whereas the latter pipe is candidate for deep-water applications that may exceed 2,000 meters of water depth. Using the finite element model, comparisons of numerical results with geometric characteristics of the pipe, provided by the pipe mill, and material properties of the “actual” pipe are presented, in order to validate the model. The simulation of JCO-E process enables the prediction of ultimate external pressure capacity of the corresponding as-fabricated JCO-E pipe taking into account different values of the manufacturing parameters. In particular, the expansion level and the displacement size of the JCO press are the main parameters under consideration. In the first application of finite element analysis (relatively thin-walled pipe), it was found that the residual stresses induced by welding stage are eliminated after the expansion process, and have minor effect on collapse pressure. Hence, in the second application of finite element analysis, the welding process is modeled through a “simple” no-slip condition activated, after JCO steps, and upon contact of the plate edges. A main conclusion of the above finite element analyzes is that the expansion process reduces ovalization and residual stresses in the pipe. Furthermore, there is an optimum level of expansion corresponding to maximum collapse pressure; beyond that level, the collapse pressure is reduced primarily because of the degradation of circumferential compressive strength, due to Bauschinger effect.

The last part of the PhD thesis presents the development of a simplified semi-analytical methodology of JCO-E forming process, based on plate kinematics and the constitutive model adopted above. This numerical modelling is aimed at better understanding of the forming process and offers a simple and efficient prediction of geometry, residual stresses, mechanical properties, and collapse pressure of JCO-E pipe with respect to the corresponding predictions obtained from finite element modelling.

**ΑΡΙΘΜΗΤΙΚΗ ΠΡΟΣΟΜΟΙΩΣΗ ΤΗΣ ΚΑΤΕΡΓΑΣΙΑΣ  
ΔΙΑΜΟΡΦΩΣΗΣ ΣΩΛΗΝΩΝ ΜΕ ΤΗ ΜΕΘΟΔΟ JCO-E ΚΑΙ ΤΗΣ  
ΕΠΙΡΡΟΗΣ ΤΗΣ ΣΤΗ ΜΗΧΑΝΙΚΗ ΣΥΜΠΕΡΙΦΟΡΑ ΚΑΙ ΑΝΤΟΧΗ  
ΥΠΟΘΑΛΑΣΣΙΩΝ ΑΓΩΓΩΝ**

ΚΩΝΣΤΑΝΤΙΝΟΣ ΑΝΤΩΝΙΟΥ

Πανεπιστήμιο Θεσσαλίας, Τμήμα Μηχανολόγων Μηχανικών, 2021

Επιβλέπων Καθηγητής: Δρ. Σπυρίδων Καραμάνος, Καθηγητής Υπολογιστικών Μεθόδων-  
Πεπερασμένων Στοιχείων των Κατασκευών

**Περίληψη**

Οι αγωγοί με σχετικά μεγάλη διάμετρο χρησιμοποιούνται ευρέως σε υποθαλάσσιες εφαρμογές μεγάλου βάθους. Στις συνθήκες αυτές, η πρόβλεψη της μηχανικής συμπεριφοράς και της αντοχής σε εξωτερική πίεση των επιμέρους σωλήνων, που αποτελούν τα μέρη ενός αγωγού αποτελεί σημαντική παράμετρο για τη βελτιστοποίηση της κατασκευής τους. Η μέθοδος κατασκευής σωλήνα JCO-E είναι αποτελεσματική ως προς το απαιτούμενο φορτίο κατεργασίας [1]. Η πρώτη ύλη από την οποία παράγεται ο σωλήνας JCO-E έχει τη μορφή χαλύβδινης πλάκας (χαλύβδινο φύλλο). Η παρούσα διδακτορική διατριβή επικεντρώνεται στην αριθμητική προσομοίωση της διαδικασίας κατασκευής σωλήνα με τη μέθοδο JCO-E, λαμβάνοντας υπόψη τις παραμέτρους της γραμμής παραγωγής. Η αριθμητική προσομοίωση πιστοποιείται συγκρίνοντας αριθμητικά αποτελέσματα με μετρήσεις που προέρχονται από τη γραμμή παραγωγής. Μετά την ολοκλήρωση της προσομοίωσης JCO-E, προβλέπεται η επίδραση της κατεργασίας στην αντοχή του σωλήνα σε εξωτερική πίεση.

Στο πρώτο μέρος της διατριβής παρουσιάζεται η προσομοίωση της διαδικασίας κατασκευής σωλήνα με τη μέθοδο JCO-E, χρησιμοποιώντας ένα κατάλληλο μοντέλο πεπερασμένων στοιχείων. Με την προσομοίωση πεπερασμένων στοιχείων υπολογίζονται οι τάσεις και οι παραμορφώσεις που αναπτύσσονται κατά τη διάρκεια των σταδίων κατασκευής, τα οποία αποτελούνται από τη διαμόρφωση των άκρων της πλάκας (edge crimping), τη διαμόρφωση JCO (JCO forming), τη συγκόλληση ευθείας ραφής των άκρων (LSAW welding) και τη διαμόρφωση διαστολής (expansion (E) operation). Επιπρόσθετα, δοκίμια εξάγονται από την πρώτη ύλη και υποβάλλονται σε μονοτονική και κυκλική φόρτιση, με σκοπό το χαρακτηρισμό του υλικού. Οι πειραματικές καμπύλες τάσης-παραμόρφωσης χρησιμοποιούνται για τη βαθμονόμηση του καταστατικού μοντέλου της προσομοίωσης. Η ελαστο-πλαστική συμπεριφορά της πλάκας κατά τη διαμόρφωσή της μοντελοποιείται με ένα

καταστατικό μοντέλο μικτής κράτυνσης, με το οποίο μπορεί να ληφθεί υπόψη η πιθανή ανισοτροπία της πλάκας. Μετά το πέρας της προσομοίωσης της διαδικασίας κατασκευής, οι ιδιότητες του υλικού που προκύπτουν από την αριθμητική ανάλυση συγκρίνονται με αντίστοιχες ιδιότητες μετρούμενες από δοκίμια που εξάγονται από το σωλήνα, για λόγους πιστοποίησης του μοντέλου πεπερασμένων στοιχείων. Στο επόμενο στάδιο της προσομοίωσης, η δομική συμπεριφορά και η αντοχή του σωλήνα υπό την επίδραση εξωτερικής πίεσης προσδιορίζεται συναρτησεί διαφόρων αλλαγών στις παραμέτρους της γραμμής παραγωγής.

Σύμφωνα με τις παραμέτρους παραγωγής της Σωληνοουργεία Κορίνθου Α.Ε., η παραπάνω αριθμητική ανάλυση με πεπερασμένα στοιχεία εφαρμόζεται για να προσομοιωθεί η διαδικασία JCO-E, ενός «σχετικά λεπτότοιχου» σωλήνα με διάμετρο 26 ίντσες και ποιότητα χάλυβα X65 και ενός σωλήνα X60 με «παχύ τοίχωμα» και διάμετρο 30 ιντσών, οι οποίοι προορίζονται για υποθαλάσσιες εφαρμογές. Ο πρώτος σωλήνας αφορά σε υποθαλάσσιες εφαρμογές σε σχετικά βαθειά νερά, ενώ ο δεύτερος σωλήνας προορίζεται για χρήση σε βάθη που ενδεχομένως ξεπερνούν τα 2000 μέτρα. Τα γεωμετρικά χαρακτηριστικά και οι ιδιότητες του υλικού του σωλήνα που προβλέπονται από τις αναλύσεις τίθενται σε αντιπαραβολή με τη γεωμετρία και τις ιδιότητες του πραγματικού σωλήνα, για λόγους πιστοποίησης των αναλύσεων. Η παρούσα μέθοδος αριθμητικής προσομοίωσης δίνει τη δυνατότητα πρόβλεψης της αντοχής του σωλήνα σε εξωτερική πίεση, πραγματοποιώντας μεταβολές στις παραμέτρους παραγωγής. Συγκεκριμένα, οι κύριες μεταβολές που εξετάζονται είναι το μέγεθος της επιβαλλόμενης διαστολής (expansion level) και η μετατόπιση της πρέσας κατά τη διαμόρφωση JCO. Στην πρώτη εφαρμογή της αριθμητικής ανάλυσης (σχετικά λεπτότοιχος σωλήνας), προέκυψε ότι οι παραμένουσες τάσεις που αναπτύσσονται κατά τη συγκόλληση μειώνονται αρκετά και η επίδρασή τους στην αντοχή του σωλήνα σε εξωτερική πίεση είναι μικρή. Ως εκ τούτου, η συγκόλληση στη δεύτερη αριθμητική ανάλυση προσομοιώνεται ως μια «απλή» ένωση των άκρων της πλάκας, που δεν επιτρέπει την μεταξύ τους ολίσθηση και λαμβάνει χώρα μετά τη διαμόρφωση JCO. Και στις δύο περιπτώσεις, τα βασικά αποτελέσματα είναι ιδιαίτερα ενδιαφέροντα. Καθώς αυξάνεται το μέγεθος της επιβαλλόμενης διαστολής μειώνεται η οβαλότητα και οι παραμένουσες τάσεις του σωλήνα. Παράλληλα, αυξάνεται η αντοχή του σε εξωτερική πίεση μέχρι ένα συγκεκριμένο επίπεδο διαστολής. Αυτό αναφέρεται ως βέλτιστο επίπεδο διαστολής (optimum level of expansion) και αντιστοιχεί στη μέγιστη αντοχή του σωλήνα σε εξωτερική πίεση. Επιβάλλοντας διαστολή μεγαλύτερη του βέλτιστου μεγέθους, η αντοχή του σωλήνα σε εξωτερική πίεση μειώνεται, λόγω μείωσης της αντοχής του υλικού σε θλίψη, που προκαλείται από το φαινόμενο Bauschinger (Bauschinger effect).

Στο τελευταίο μέρος της διατριβής, αναπτύσσεται μια ημι-αναλυτική μεθοδολογία που απλουστεύει την προσομοίωση πεπερασμένων στοιχείων, της διαδικασίας διαμόρφωσης σωλήνα με τη μέθοδο JCO-E, με βάση την κινηματική της πλάκας και του προαναφερθέντος καταστατικού μοντέλου. Η παρούσα απλοποιημένη μέθοδος στοχεύει στην κατανόηση της διαδικασίας διαμόρφωσης και στην πρόβλεψη της γεωμετρίας, των παραμενουσών τάσεων και των μηχανικών ιδιοτήτων του σωλήνα JCO-E, όπως επίσης και της αντοχής του σε εξωτερική πίεση, απλούστερα και με χαμηλότερο υπολογιστικό κόστος σε σχέση με τη μέθοδο προσομοίωσης με πεπερασμένα στοιχεία.



## Contents

|   |    |
|---|----|
| Chapter 1 - Introduction .....  | 1  |
| 1.1    Introduction .....   | 1  |
| 1.2    JCO-E manufacturing process .....  | 5  |
| 1.3    Literature review.....   | 7  |
| 1.4    Scope of the present dissertation .....  | 9  |
| Chapter 2 - Finite Element Modelling of JCO-E Pipe Fabrication Process .....              | 13 |
| 2.1    Description of the finite element model .....                                      | 13 |
| 2.2    Constitutive model.....  | 15 |
| 2.2.1    Governing equations.....   | 15 |
| 2.2.2    Numerical integration and implementation .....                                   | 20 |
| 2.3    Constitutive model calibration .....   | 23 |
| 2.4    Finite element modelling of Welding (SAW) process .....                            | 24 |
| 2.5    Validation of the numerical model .....  | 27 |
| 2.6    Conclusions .....  | 28 |
| Chapter 3 - Applications of finite element analysis .....                                 | 29 |
| 3.1    Relatively thin-walled JCO-E pipe ( $D/t=34.67$ ).....                             | 29 |
| 3.1.1    Material testing and model calibration .....                                     | 31 |
| 3.1.2    Modelling of pipe fabrication process .....                                      | 36 |
| 3.1.3    Mechanical properties of JCO-E pipe .....  | 42 |
| 3.1.4    Effect of expansion on pipe thickness and residual stresses .....                | 48 |
| 3.1.5    Effect of expansion and welding process on pipe ovality and collapse<br>pressure | 52 |
| 3.1.6    Effect of anisotropy on external pressure capacity.....                          | 57 |
| 3.2    Thick-walled JCO-E pipe .....  | 58 |

|   |   |     |
|---|---|-----|
| 3.2.1   | Material model calibration.....   | 59  |
| 3.2.2   | Modelling of pipe forming process .....                                   | 59  |
| 3.2.3   | Mechanical properties of JCO-E pipe .....                                 | 64  |
| 3.2.4   | Effect of expansion on pipe thickness and residual stresses .....         | 67  |
| 3.2.5   | Effect of expansion on pipe ovality and collapse pressure.....            | 68  |
| 3.2.6   | Effect of JCO punching steps on pipe ovality and collapse pressure .....  | 73  |
| 3.3   | Conclusions .....   | 74  |
| Chapter 4 - Idealized Analytical Modelling of the JCO-E Forming Process ..... |   | 77  |
| 4.1   | Formulation of the idealized analytical model .....                       | 78  |
| 4.1.1   | Kinematics .....  | 78  |
| 4.1.2   | Constitutive model.....   | 81  |
| 4.1.3   | Numerical implementation .....  | 83  |
| 4.2   | Steps of the idealized analytical model .....                             | 87  |
| 4.2.1   | First step: bending .....   | 90  |
| 4.2.2   | Second step: small expansion .....  | 90  |
| 4.2.3   | Third step: unloading.....  | 91  |
| 4.2.4   | Fourth and fifth steps: expansion and unloading.....                      | 92  |
| 4.3   | Pipe material properties .....  | 94  |
| 4.4   | Application of idealized model to relatively thin-walled JCO-E pipe ..... | 97  |
| 4.4.1   | Collapse performance .....  | 102 |
| 4.5   | Application of idealized model to thick-walled JCO-E pipe.....            | 107 |
| 4.5.1   | Collapse performance .....  | 109 |
| 4.6   | Conclusions .....   | 111 |
| Chapter 5 - Summary and Conclusions .....                                     |   | 112 |
| References .....  |   | 116 |

## List of Tables

|   |     |
|---|-----|
| Table 3.1: Material parameters used in modelling the X65 steel material .....                     | 35  |
| Table 3.2: Geometric characteristics of the JCO-E pipe .....                                      | 42  |
| Table 3.3: Yield strength $R_{10.5}$ in the transverse direction of the JCO-E pipe.....           | 46  |
| Table 3.4: Pipe collapse pressure according to design equations.....                              | 57  |
| Table 3.5: Effect of anisotropy on collapse pressure.....   | 58  |
| Table 3.6: Material model parameters .....  | 59  |
| Table 3.7: Pipe inner diameter.....   | 63  |
| Table 3.8: Measured yield strength $R_{10.5}$ in the transverse direction of the JCO-E pipe ..... | 66  |
| Table 3.9: External pressure (collapse) design .....  | 72  |
| Table 4.1: Collapse pressure of the pipe, obtained from the collapse analysis model .....         | 104 |

## List of Figures

|  |    |
|--|----|
| Figure 1.1: Schematic representation of the loading conditions during “J-lay” pipeline installation in deep water. (source: [2]) .....   | 2  |
| Figure 1.2: Schematic representation of half of the ring subjected to uniform external pressure.....   | 3  |
| Figure 1.3: JCO-E pipe manufactured in Corinth Pipeworks S.A. facilities (Thisvi, Greece); (a) Crimping press, (b) JCO press, (c) Inside welding process, (d) Outside welding process, (e) Mechanical expander. .... | 6  |
| Figure 1.4: Schematic representation of the JCO-E manufacturing process; (a) Crimping, (b) J-phase, (c) C-phase, (d) O-phase, (e) Inside welding, (f) Outside welding, (g) Expansion.....                            | 7  |
| Figure 1.5: Schematic representation of the UOE forming process; (a) Crimping, (b) U-phase, (c) O-phase, (d) Expansion. (source: [6]) .....  | 8  |
| Figure 2.1: A schematic of the steel plate showing transverse and longitudinal directions.....   | 17 |
| Figure 2.2: Schematic representation of the double ellipsoidal heat source. ....   | 26 |
| Figure 2.3: Location of the strip specimens extracted from the JCO-E pipe. ....  | 28 |
| Figure 3.1: A part of the finite element mesh of the steel plate, corresponding to 1/6 of the plate width. ....  | 30 |
| Figure 3.2: The finite element mesh of the auxiliary three-dimensional (welding) model. ....   | 30 |
| Figure 3.3: Adopted notation and position of tested specimens with respect to plate geometry. ....   | 31 |
| Figure 3.4: The experimental strain-controlled setup used for cyclic tests. ....   | 32 |
| Figure 3.5: Measured tensile stress-strain response in the transverse direction of the plate. ....   | 33 |
| Figure 3.6: Stress-strain curves of the steel plate in the transverse and longitudinal direction of the plate. ....  | 33 |
| Figure 3.7: Stress-strain curves showing the homogeneity of the steel plate; (a) across the thickness of the plate (IN vs OUT), (b) along the plate length, (c) across the plate width. ....                         | 34 |

|  |    |
|--|----|
| Figure 3.8: Stress-strain diagrams, including reverse loading and re-loading from the steel plate experiments, and the corresponding numerical fitting using (a) MAT1 material properties, (b) MAT2 material properties.....   | 35 |
| Figure 3.9: Plate configuration of the forming process prior to welding (MAT1 set of material parameters). .....   | 37 |
| Figure 3.10: Equivalent plastic strain distribution at the third punching step.....  | 38 |
| Figure 3.11: Plate configuration after the JCO forming; the gap between the two edges is compared with measurements from the pipe mill. ....   | 38 |
| Figure 3.12: Von Mises stress distribution in the auxiliary model: (a) before the outside welding step starts, and at different locations of the heat source during outside welding, namely: (b) $z = L/4$ , (c) $z = L/2$ , (d) $z = 3L/4$ , and (e) at the end of the welding simulation. .... | 39 |
| Figure 3.13: Comparison between the predicted temperature field of the selected weld area cross-section and the weld macrograph provided by Corinth Pipeworks S.A.; (a) first pass, corresponding to inside welding, and (b) second pass, corresponding to outside welding. ....                 | 40 |
| Figure 3.14: Distribution of von Mises stress in the pipe; (a) at initial position of the expander segments (JCO pipe), (b) before unloading from the expansion phase, (c) after unloading from the expansion phase (JCO-E pipe).....  | 41 |
| Figure 3.15: Numbering of elements at 90-degree position, across the pipe thickness. ....  | 42 |
| Figure 3.16: Measured and predicted compressive stress-strain response in the transverse direction of the pipe.....  | 44 |
| Figure 3.17: Measured and predicted compressive stress-strain response in the longitudinal direction of the pipe.....  | 45 |
| Figure 3.18: Transverse stress-strain response of the plate material in comparison with the JCO-E pipe material tested in compression, as obtained from (a) experiments and (b) MAT1 material model. ....  | 45 |
| Figure 3.19: Measured and predicted tensile stress-strain response in the transverse direction of the pipe. ....   | 46 |

|   |    |
|---|----|
| Figure 3.20: Stress-strain response of the pipe; predictions obtained from the MAT2 material properties compared with experimental results. ....  | 47 |
| Figure 3.21: Predicted tensile stress-strain response of the JCO pipe (non-expanded) and the JCO-E pipe. ....   | 48 |
| Figure 3.22: Predicted compressive stress-strain response of the JCO pipe and the JCO-E pipe. ....  | 48 |
| Figure 3.23: Average pipe thickness $t_{\text{average}}$ in terms of expansion strain. ....   | 50 |
| Figure 3.24: Calculated circumferential residual stress distribution of the JCO-E pipe at 180-degree position, for different values of expansion strain; the first picture (top-left) refers to the stage after welding, where no expansion is applied (JCO pipe). ....   | 51 |
| Figure 3.25: Calculated circumferential residual stress distribution of the JCO-E pipe at 90-degree position, for four expansion levels. ....   | 52 |
| Figure 3.26: Effect of expansion on collapse pressure $P_{\text{co}}$ and the corresponding initial ovalization $\Delta_0$ . ....   | 55 |
| Figure 3.27: Predicted response of the pipe under external pressure with respect to cross-sectional ovalization. ....   | 56 |
| Figure 3.28: Deformed cross-sectional shape of the JCO-E pipe subjected to external pressure for the case of $\varepsilon_E = 1.02\%$ ; (a) configuration at maximum external pressure corresponding to ovalization $\Delta = 0.80\%$ ; (b) post-buckling configuration corresponding to ovalization $\Delta = 8.00\%$ . .... | 56 |
| Figure 3.29: Steel plate material; (a) monotonic and (b) cyclic stress-strain response. ....  | 60 |
| Figure 3.30: Plate configuration during the crimping and the JCO forming process. ....  | 61 |
| Figure 3.31: Gap-closing process with finishing press. ....   | 62 |
| Figure 3.32: Expansion of the JCO pipe. ....  | 63 |
| Figure 3.33: Measured and predicted stress-strain responses in the longitudinal direction of the pipe. ....   | 64 |

|  |    |
|--|----|
| Figure 3.34: Measured and predicted compressive stress-strain response in the transverse direction of the pipe.....  | 65 |
| Figure 3.35: Measured and predicted tensile stress-strain response in the transverse direction of the pipe.....  | 66 |
| Figure 3.36: Effect of the expansion strain $\varepsilon_E$ on the average thickness $t_{\text{average}}$ of JCO pipe. ....  | 67 |
| Figure 3.37 Calculated circumferential (residual) stress distribution of the JCO-E pipe at 180-degree position, for different expansion levels.....  | 68 |
| Figure 3.38: Ultimate external pressure capacity $P_{CO}$ and the corresponding initial ovalization $\Delta_0$ of JCO-E pipe for different values of expansion strain $\varepsilon_E$ . ....   | 70 |
| Figure 3.39: Predicted pressure-ovalization response of the pipe. ....   | 71 |
| Figure 3.40: Cross-sectional shapes of the JCO-E pipe expanded with $\varepsilon_E = 1.70\%$ after the application of external pressure; (a) configuration at maximum external pressure corresponding to ovalization $\Delta = 0.33\%$ ; (b) post-buckling configuration corresponding to ovalization $\Delta = 6.00\%$ . .... | 71 |
| Figure 3.41: Cross-sectional shapes of the JCO-E pipe expanded with $\varepsilon_E = 2.22\%$ after the application of external pressure; (a) configuration at maximum external pressure corresponding to ovalization $\Delta = 0.41\%$ ; (b) post-buckling configuration corresponding to ovalization $\Delta = 6.00\%$ . .... | 72 |
| Figure 3.42: Variation of (a) initial ovalization $\Delta_0$ and (b) collapse pressure $P_{CO}$ in terms of expansion strain. ....   | 74 |
| Figure 4.1: Steps used in the idealized modelling of the JCO-E forming process.....  | 80 |
| Figure 4.2: Flowchart of the computer code representing the idealized forming steps.....   | 89 |
| Figure 4.3: Deformation of a material element of the idealized pipe due to (uniform) expansion. ....   | 94 |
| Figure 4.4: Flowchart of the code corresponding to the one-dimensional model. ....   | 97 |
| Figure 4.5: Predicted thickness of the relatively thin-walled JCO-E pipe in terms of expansion strain, obtained from equation (4.56) and from finite element model.....  | 98 |

|  |     |
|--|-----|
| Figure 4.6: Stress-strain history in the transverse direction of JCO-E pipe ( $\epsilon_E = 1.33\%$ ), calculated at (a) the inner and (b) the outer points of pipe wall. .... | 99  |
| Figure 4.7: Stress-strain history during the JCO-E forming process in the longitudinal direction; the value of expansion strain $\epsilon_E$ is 1.33%. ....                    | 100 |
| Figure 4.8: Predicted compressive stress-strain responses in the transverse direction of pipe. ....  | 101 |
| Figure 4.9: Predicted tensile stress-strain responses in the transverse direction of pipe. ....  | 102 |
| Figure 4.10: The un-deformed geometry and the finite element mesh used in collapse analysis model. ....  | 103 |
| Figure 4.11: Stress-strain paths in the transverse direction of pipe during the application of external pressure. ....   | 105 |
| Figure 4.12: Predicted compressive stress-strain response of the inner point of the idealized JCO-E pipe wall for three cases of expansion strain. ....                        | 106 |
| Figure 4.13: Predicted thickness of the thick-walled JCO-E pipe for different values of expansion strain, obtained from equation (4.56) and from finite element model. ....    | 107 |
| Figure 4.14: Calculated stress-strain history of the inner point of pipe wall in transverse direction for $\epsilon_E = 1.70\%$ . ....   | 108 |
| Figure 4.15: Transverse stress-strain responses of the inner point of JCO-E pipe wall; (a) under compressive, and (b) under tensile uniaxial loading. ....                     | 109 |
| Figure 4.16: The geometry and the finite element mesh adopted in collapse analysis model. ....   | 110 |



# **Chapter 1 - Introduction**

## **1.1 Introduction**

The installation of offshore pipelines constitutes a critical stage in offshore pipeline design. A combination of external pressure, bending and tension is applied on the pipeline during pipeline installation, as schematically illustrated in Figure 1.1, especially at the “sagbend” region, near the sea bottom, that may cause buckling, in the form of collapse. The collapsed configuration of pipeline refers to a “flattened” pattern, in the form of a “dogbone” shape and is often associated with propagation of this pattern, referred to as “buckle propagation”. This phenomenon is quite dangerous, because it may destroy a very long part of the pipeline with catastrophic consequences. In this framework, external pressure is the primary load parameter in the design of offshore pipelines; pipelines are usually installed empty and, during their operation, they are sometimes internally depressurized for maintenance.

The mechanical response of a metal circular pipe under external pressure is shortly presented herein by means of buckling theory [2]. Upon application of external pressure, a uniform circumferential contraction of the pipe cross-section mainly occurs. Increasing the external pressure, when the critical level of pressure is reached, the pipe exhibits structural instability, with a buckling mode in the form an oval shape of the pipe cross-section. If the pipe has an initial cross-sectional ovalization, upon application of external pressure, this initial ovalization grows leading to non-linear response associated with hoop bending and stresses. The combined effect of hoop (circumferential) stresses and bending causes yielding of material, and reduction of ring stiffness, leading to a pressure maximum, which is often referred to as collapse pressure and expresses the resistance of the pipe against external pressure. Beyond the maximum (collapse) pressure, significant stresses develop at four equally-spaced points of the ovalized ring cross-section, associated with the development of

plastic strains at those points, and as a result, a four-hinge plastic mechanism is formed, leading to pipe cross-section collapse.

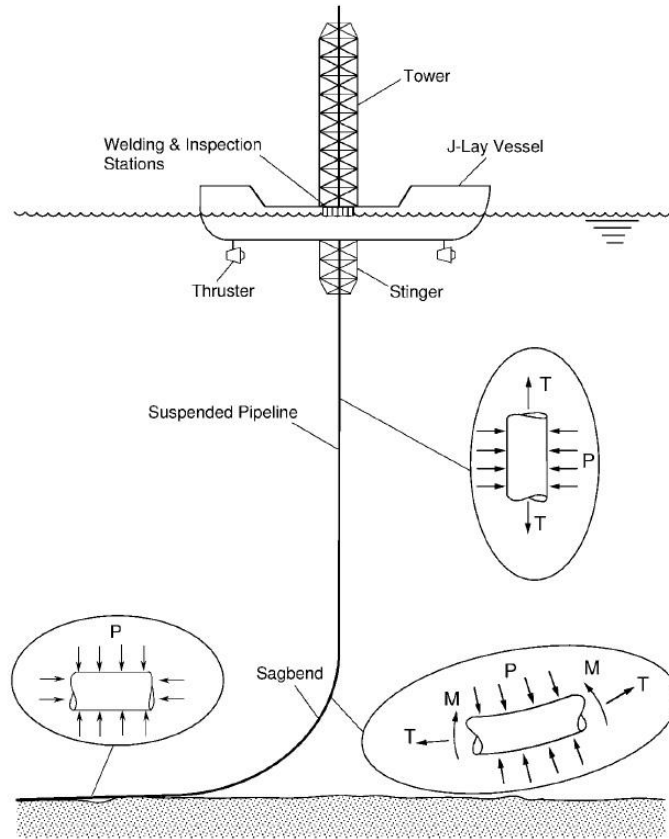


Figure 1.1: Schematic representation of the loading conditions during “J-lay” pipeline installation in deep water. (source: [2])

Many researchers studied the buckling of a cylindrical (steel) tube under external pressure and proposed theoretical formulas for the calculation of collapse (critical) pressure. In the book of Timoshenko *et al.* [3], the critical buckling pressure of an elastic circular ring, which is subjected to uniform external pressure, is expressed by the following equation:

$$P_e = \frac{3EI}{R^3} \quad (1.1)$$

where  $E$  is the modulus of elasticity,  $I$  denotes the moment of inertia of the ring’s cross-section, and  $R$  is the radius of the center line of the ring. Equation (1.1) is derived from the theory of elasticity, considering a slight deflection produced from the circular form of equilibrium. The buckling pressure  $P_e$  corresponds to that value, so that the ring is in

equilibrium in the assumed slightly deformed shape. In Figure 1.2, half of the ring is schematically shown.

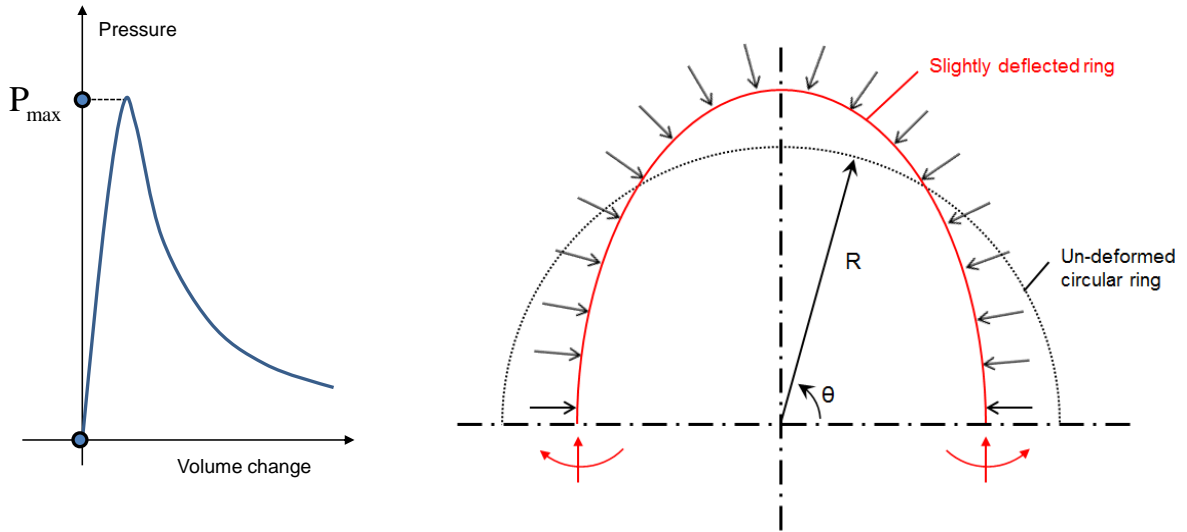


Figure 1.2: Schematic representation of half of the ring subjected to uniform external pressure.

If the ring constitutes a portion of a quite long tube (e.g. the length of long tube resembles the length of offshore pipeline), the uniform external pressure is applied to the ring in plane strain conditions. Therefore, using Hooke's law in three-dimensions, due to those plane strain conditions, the Young's modulus  $E$  in equation (1.1) has to be replaced by the term  $E/(1-\nu^2)$ . Finally, taking into account the above modification, and substituting in equation (1.1) the term  $I$  with  $t^3/12$ , where a unit length of the ring is considered, one results in the following expression for the critical elastic buckling pressure, as follows:

$$P_e = \frac{2E}{1-\nu^2} \left( \frac{t}{D} \right)^3 \quad (1.2)$$

where  $\nu$  is the Poisson's ratio,  $t$  is the wall thickness, and  $D$  is the mean diameter of the ring.

Furthermore, one can easily obtain the following relation for the compressive stress developed in the circumferential (hoop) direction of the ring.

$$\sigma_\theta = \frac{pD}{2t} \quad (1.3)$$

Radial stress  $\sigma_r$  is also present to balance the external pressure  $p$ . However, the circumferential stress is equal to “ $p$ ” times the ratio  $(D/2t)$ . In practical applications this ratio is usually larger than 10, and as a result, the radial stress can be neglected in comparison with the circumferential stress. Considering elastic-plastic behavior of the ring material, and only hoop stress, the plastification of ring wall occurs at the following pressure level, known as yield pressure

$$P_y = 2\sigma_y \frac{t}{D} \quad (1.4)$$

where  $\sigma_y$  is the yield stress of the material. For plane strain conditions and using Von Mises yield criterion, one readily obtains that the pressure that causes yielding of ring wall is approximately 15% higher compared to the value of pressure calculated from equation (1.4).

According to Murphey *et al.* [4], a first estimate of collapse pressure  $P_{CO}$  can be obtained by the following formula

$$P_{CO} = \frac{P_e P_y}{\sqrt{P_e^2 + P_y^2}} \quad (1.5)$$

where  $P_e$  and  $P_y$  are identified by equations (1.2) and (1.4), respectively. However, equation (1.5) does not account for factors that may influence the collapse pressure. Previous works (e.g. [5], [6]) on external pressure capacity have shown that the resistance of offshore pipelines against external pressure is affected by initial geometric deviations from the ideal circular shape (initial ovality) and by the presence of residual stresses, both introduced during the line pipe manufacturing process. In relevant design standards ([7], [8]), for calculating the external pressure capacity of offshore pipelines, equations (1.2) and (1.4) are applicable employing appropriate safety factors that account for the effects of line pipe process, such as initial imperfections and residual stresses. Therefore, quantifying the size and shape of initial geometric imperfections, as well as the amplitude and distribution of residual stresses, with respect to the fabrication parameters constitutes a key issue towards predicting the collapse pressure of the pipe under consideration.

## 1.2 JCO-E manufacturing process

The JCO-E method is a high-quality and efficient method for manufacturing large-diameter steel line pipes of significant thickness, candidates for offshore applications, with diameter-to-thickness ratio ( $D/t$ ) which is usually less than 60. Herein, the basic stages of JCO-E manufacturing process are described. The first stage of JCO-E process is the plate edge milling phase, where the plate edges are trimmed and beveled to accommodate the welding. In the second stage, the plate moves to the crimping press, as shown in Figure 1.3a, where the plate edges are formed into circular arcs. Subsequently, the JCO punching press progressively deforms the plate into a round shape (Figure 1.3b). Subsequently, the ends of the deformed plate are mechanically joined and welded. The welding process consists of tack welding followed by submerged arc welding (SAW) method, where two multi-electrode passes perform welding, first on the inside and then on the outside of the pipe (Figure 1.3c and Figure 1.3d, respectively). The pipe product just after welding is referred to as JCO pipe. After the welding process, the last forming step, called “expansion”, is performed on the JCO pipe using a mechanical expander, as shown in Figure 1.3e, to improve and control its geometry. The pipe resulting after unloading from the expansion phase is considered as the final product of this fabrication process, and it is referred to as JCO-E pipe.

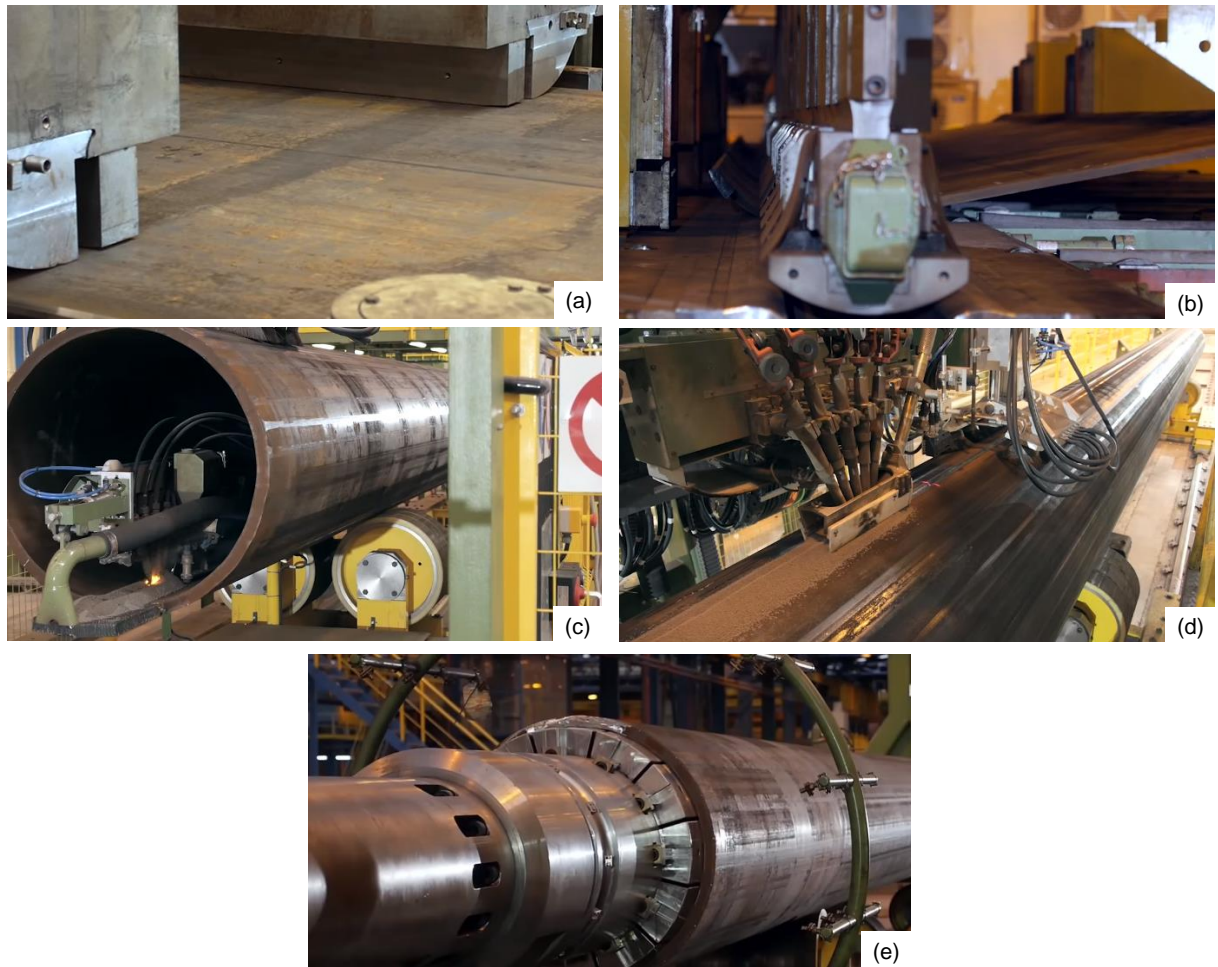


Figure 1.3: JCO-E pipe manufactured in Corinth Pipeworks S.A. facilities (Thisvi, Greece); (a) Crimping press, (b) JCO press, (c) Inside welding process, (d) Outside welding process, (e) Mechanical expander.

The JCO-E manufacturing process, described above, is shown schematically in Figure 1.4. During the above forming process, the steel plate undergoes significant cold bending and tension. This cold forming induces residual stresses and strains in the deformed plate and constitutes an important factor, which may affect the ovality of final line pipe product and its external pressure capacity. In this perspective, modelling of the manufacturing process of JCO-E pipes, may contribute to reliable prediction of their geometry, material properties and structural response, towards optimizing the manufacturing process.

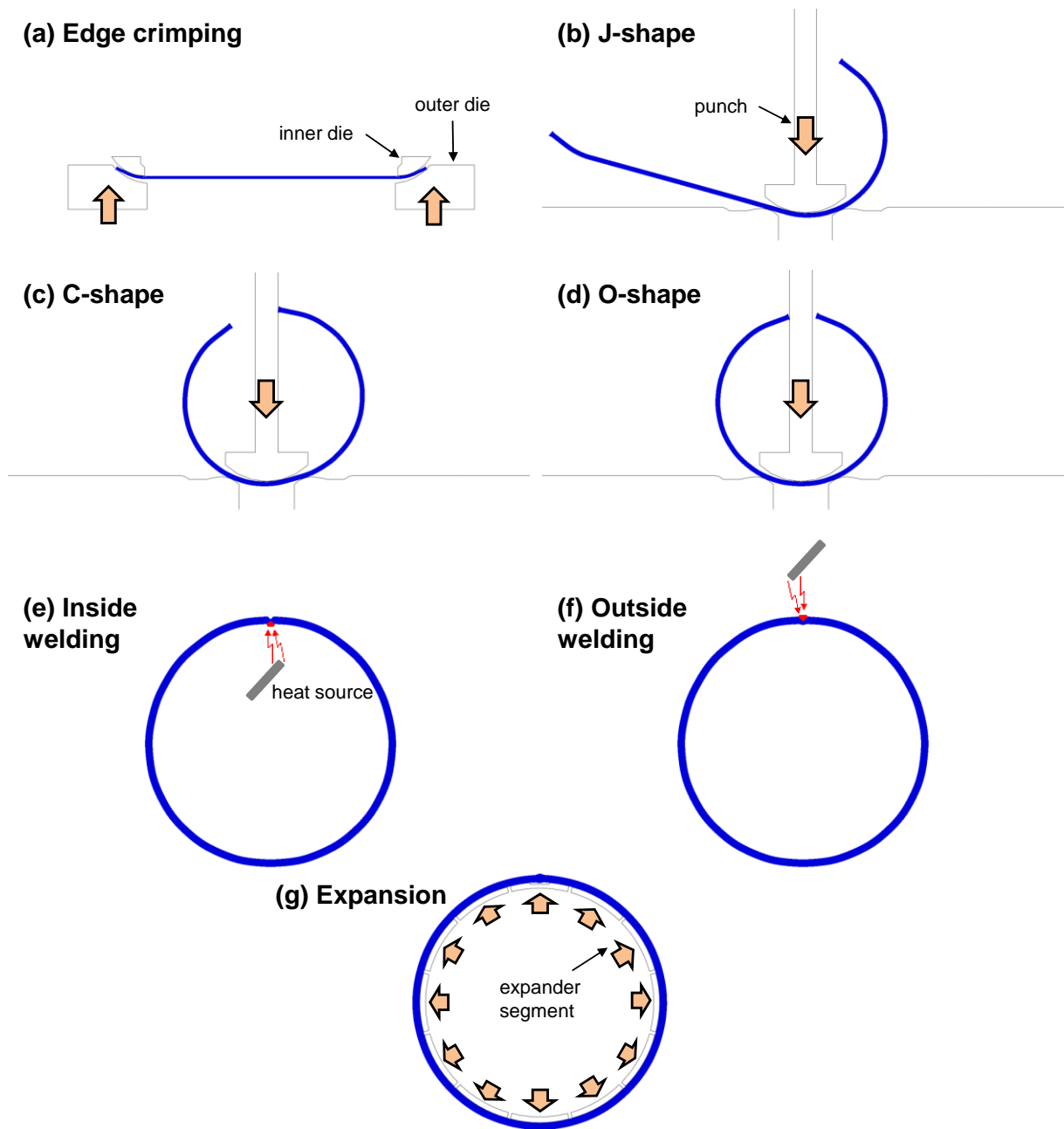


Figure 1.4: Schematic representation of the JCO-E manufacturing process; (a) Crimping, (b) J-phase, (c) C-phase, (d) O-phase, (e) Inside welding, (f) Outside welding, (g) Expansion.

### 1.3 Literature review

The existing literature that refers to JCO-E pipe process and its effect on geometry, material properties and collapse performance of the pipe is limited. In contrast, the UOE line pipe fabrication process, and its effect on the mechanical response of the pipe product has been studied more extensively. The UOE process, schematically shown in Figure 1.5, is an

alternative to the JCO-E process, where the JCO forming steps are replaced by the U and O steps. Following, some important publications referred to UOE manufacturing process are mentioned. An initial study on the effects of UOE process on the mechanical behavior has been reported by Kyriakides *et al.* [5] using a simple analytical model. It has been shown for the first time that the cold forming of line pipes has a significant effect in determining the level of residual stresses in a line pipe, and should be taken into consideration for the prediction of ultimate external pressure and pressurized bending capacity. Similar conclusions have been reported in the experimental works [9], [10]. A finite element study has been reported on the effect of UOE cold bending process on the collapse pressure by Herynk *et al.* [11], employing an advanced two-surface cyclic-plasticity model with nonlinear kinematic hardening. Chatzopoulou *et al.* [6] examined the effect of UOE cold bending process on pipes subjected to combined loading, extending the work reported in [11]. Toscano *et al.* [12] have simulated UOE processes using finite element models and more traditional plasticity models, and predicted the ultimate external pressure capacity of the pipes.

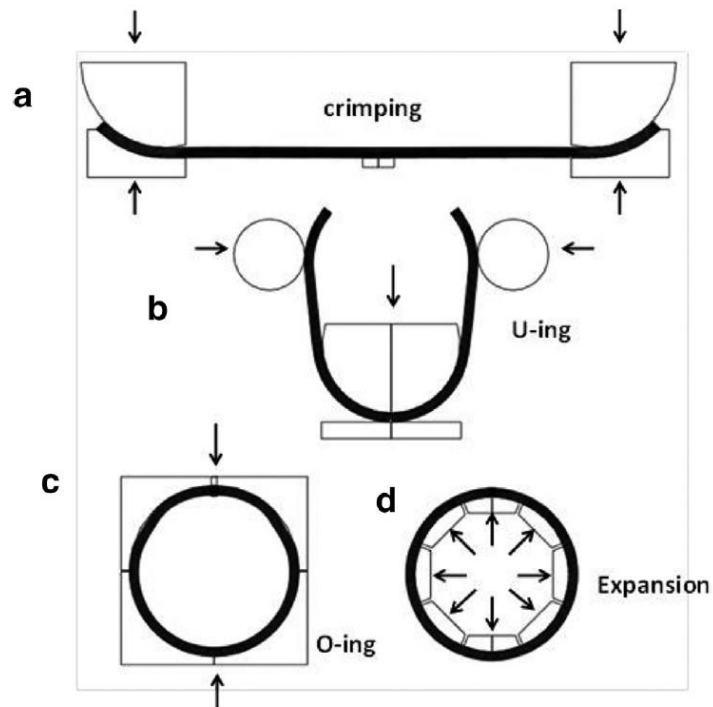


Figure 1.5: Schematic representation of the UOE forming process; (a) Crimping, (b) U-phase, (c) O-phase, (d) Expansion. (source: [6])



On the other hand, the JCO-E manufacturing process has received less attention in the literature. Chandel *et al.* [1] have simulated the JCO-E manufacturing process and concluded that during line pipe forming, the radius of forming tools and dies play a critical role in forming a geometrical accepted final line pipe. Fan *et al.* [13] have applied a finite element model to simulate a JCO-E experiment and presented the consecutive deformation characteristics of its JCO-E forming process. Gao *et al.* [14] have examined numerically the effect of punch displacement on opening width after the JCO steps and found its value that results to an opening width within the accepted range determined by the pipe mill. Kathayat *et al.* [15] have presented numerical studies conducted on JCO-E pipes pointing out key steps to be considered during manufacturing, and studied (both numerically and experimentally) ring collapse tests showing that coating increases the collapse pressure. Krishnan and Baker [16] examined JCO-E and JCO-C manufacturing processes, and their effect on the collapse pressure of the line pipe; the latter manufacturing process consists of uniformly compressing instead of expanding the JCO pipe (final forming step), as an attempt to overcome the Bauschinger effect. Reichel *et al.* [17] presented a more detailed investigation on the effect of JCO-C manufacturing process on the material properties of the formed pipe and its collapse pressure.

#### **1.4 Scope of the present dissertation**

The aforementioned studies on JCO-E pipes have mainly focused on the prediction of collapse pressure: (a) taking into account plasticity models that are not able to capture effectively the plate material behavior during fabrication, and excluding the simulation of welding process, or (b) using a numerical model, which accounts for the measured geometry and measured material properties of the pipe, as an attempt to bypass the simulation of JCO-E process. In the present thesis, the collapse pressure of a JCO-E pipe can be evaluated: (a) performing a finite element analysis that simulates the entire manufacturing process (i.e. forming and SAW welding stages) with the use of a suitable plasticity model, or (b) performing a “simple” collapse analysis, which employs the geometry, the residual stresses and the material properties of pipe, obtained from the proposed idealized modelling of JCO-E forming process. Following, the aim and key features of the present thesis are reported more extensively.

The present study aims at developing efficient numerical tools for the simulation of JCO-E process, capable of predicting the geometry and the mechanical properties of JCO-E pipes, as well as their structural response and collapse resistance under external pressure. The main novelty of the present study is that both the simulation of JCO-E process and the prediction of structural behavior of JCO-E pipe under external pressure are investigated, so that the correlation between the process and its effect on collapse performance is achieved. Therefore, the outcomes of the simulation can be used for the optimization of JCO-E process; optimization of pipe geometry, pipe material properties, and strength of pipe against external pressure. Initially, a finite element methodology is developed for the above predictions. The intermediate innovative steps consist of: (a) the use of a material model that takes into account the anisotropy of steel plate, (b) the simulation of the entire JCO-E fabrication process and the response under external pressure in a single finite element model, and (c) the comparison of geometric and mechanical properties of JCO-E pipe obtained from the finite element simulation with actual measurements and experimental results, respectively. The development and calibration of an efficient constitutive model that accounts for the evolution of the yield surface with respect to plastic deformation is a target, so that reliable predictions of JCO-E pipe properties and its collapse pressure are obtained. Furthermore, key feature of the present thesis constitutes the development of a simplified model that simulates the forming process of a JCO-E pipe enabling “quicker” prediction of the residual stresses and the material properties of pipe, for various expansion levels, with respect to the finite element model. Subsequently, the predictions obtained from simplified model can be used to predict the collapse pressure performing a “simple” ring collapse analysis.

A short outline of the thesis contents is given below. In Chapter 2, the development of a simulation methodology of JCO-E manufacturing process is presented using a finite element model, capable of predicting the geometry and the mechanical properties of JCO-E pipe, as well as its structural response under external pressure until collapse, in a unified approach. More specifically, using a two-dimensional generalized plane strain model, the crimping phase and the JCO steps are simulated first. Subsequently, the welding process is simulated using an auxiliary three-dimensional solid model, which communicates directly with the two-dimensional model. Upon completion of the welding simulation, the stress-strain field in the weld area (weld metal and heat-affected zone) obtained from the auxiliary model is transferred to the two-dimensional model, and the analysis continues for simulating the

expansion stage. To model the plate material behavior during forming process, a rigorous constitutive model is presented and incorporated in the finite element model. This model is based on that introduced elsewhere [6], which is capable of modelling special features of steel elastic-plastic plate behavior, such as the yield plateau at initial yielding and the Bauschinger effect upon reverse plastic loading. In the present study, an improvement of the above constitutive model is presented and adopted, aiming at the further ability of the model to take into account the anisotropy of raw material. It is calibrated through available experimental data on monotonic and cyclic uniaxial loading of coupons extracted from the plate material. Finally, at the end of manufacturing process, geometrical deviations and mechanical properties of the pipe are evaluated and the numerical results are compared with available measurements and experimental data, respectively.

The above finite element method is applied to a “relatively thin-walled” with  $D/t=34.67$  and a “thick-walled” JCO-E pipe with  $D/t=19.69$ , as described in detail in Chapter 3. In the first application, it is concluded that the residual stresses induced by welding process are reduced after the expansion stage, and their presence does not affect the collapse pressure of JCO-E pipe significantly. For that reason, the second application focuses on simulating the JCO-E forming stages (not the welding process) and its effect on collapse pressure. In both pipes, the simulations take into account the manufacturing parameters provided by the pipe mill. At the end of numerical simulations, predictions of the pipe geometry and material properties are compared with actual measurements from the pipe mill and experimental data performed in the course of the present thesis, respectively. After unloading from the expansion phase and completion of the fabrication process the analysis proceeds, using the same finite element model, applying uniform external pressure to the JCO-E pipe, so that the ultimate pressure capacity is determined. A similar procedure has also been employed for UOE pipes in previous publications [11], [6], [12]. The above concept of combining the JCO-E process with the structural response in one single analysis, apart from determining the mechanical properties of line pipe, offers a powerful tool for evaluating the structural performance of line pipe in the offshore environment, accounting in a straightforward manner for the residual stresses and the geometric features after its fabrication process. Finally, parametric studies are conducted to examine the influence of forming parameters on ultimate external pressure capacity of the as-fabricated final product.

In Chapter 4, the development of an idealized model is presented for the simple and efficient simulation of JCO-E forming process. The main purpose of this simplified model is to overcome the computational cost of the corresponding finite element modelling. This idealized model predicts the residual stresses of JCO-E pipe, and is also coupled with a one-dimensional model that provides prediction of the material behavior of JCO-E pipe in transverse direction. Using numerical results from the above idealized model, the collapse pressure of JCO-E pipe can be predicted performing a collapse analysis in a simple finite element program, considering geometric characteristics and residual stresses calculated from the idealized model, and material properties computed from the one-dimensional model. The computational efficiency of the idealized model is demonstrated by comparing its results with the corresponding predictions obtained from the rigorous finite element simulation.

Finally, in Chapter 5, the main conclusions of the present thesis are summarized and recommendations for future work are proposed.

## **Chapter 2 - Finite Element Modelling of JCO-E Pipe Fabrication Process**

### **2.1 Description of the finite element model**

A quasi two-dimensional model has been developed to describe the steel plate deformation during the manufacturing process. The model describes the cross-sectional deformation of steel plate, assuming generalized plane strain conditions. This allows for the simulation of forming process from the flat plate configuration to the circular shape of the pipe, as well as for the subsequent application of external pressure, in a sequence of analysis steps, accounting for the manufacturing process in a straightforward manner. The use of generalized plane strain conditions, instead of simple plane strain conditions, allows for controlling the out-of-plane deformation in a way compatible with the conditions imposed in the pipe mill. The geometry of steel plate, including the geometry of filler material induced in its beveled edges at the welding stage, the geometry of forming dies, the number of punching steps along the plate width, the geometry of punch, the number and the geometry of expander segments, as well as their initial positions and displacements, have been provided by the pipe mill and used as input parameters for the finite element model.

Crimping of the plate edges constitutes an important step of JCO-E manufacturing process that influences the final dimensions close to the weld area [1]. During the crimping stage, the inner die is fixed, while the outer die is moved upwards forcing the plate edges to obtain the desired radius of bending (Figure 1.4a). Subsequently, the outer die is retracted and the plate unloads elastically. The analysis proceeds by simulating JCO forming process (Figure 1.4b, Figure 1.4c, Figure 1.4d), where the plate is subjected to progressively local bending and unloading conditions by applying punching steps along the plate width from one crimped edge (J-shape) to the other crimped edge (C-shape), and to the final punching step at the center of the plate, to obtain an O-shape. After the punch is removed, the two plate edges

come together by applying an appropriate mechanical loading to their surfaces, and the welding process (Figure 1.4e, Figure 1.4f) is simulated through an auxiliary model that “communicates” with this model, and it is presented in detail in Section 2.4. At the end of welding process, the pipe is referred to as “JCO pipe”. Subsequently, taking into account the stress-strain field developed in the weld area, the analysis proceeds by simulating the expansion stage. The expander segments (Figure 1.4g) are displaced radially in the outward direction forcing the pipe to obtain the desired geometric characteristics. The expander segments are not initially in contact with the internal surface of JCO pipe. When the expander segments start to move radially with the same amount of displacement, the JCO pipe accommodates itself into the new position of the segments. A quasi-circular shape of the pipe is obtained at the stage where all expander segments establish contact with the internal surface of the pipe. Further outward displacement of the expander segments, causes pipe expansion and, as a result, the pipe diameter comes closer to its nominal value. The pipe, after expansion and the corresponding unloading, is considered as the final product of JCO-E manufacturing process, and it is called “JCO-E pipe”. Upon reaching the final configuration of JCO-E pipe, and using the same two-dimensional model, uniform external pressure is applied on the external surface of the pipe and a nonlinear analysis is performed using Riks' continuation method, so that the maximum pressure, referred to as “collapse pressure” or “buckling pressure”, is obtained, together with the pipe post-buckling response.

The model employs analytical rigid surfaces to simulate forming tools and dies. A strict “master-slave” algorithm has been used for the contact between forming dies and the steel plate; the master surface refers to the forming dies and the slave surface refers to the steel plate. The contact pairs allow for “finite sliding” between the two surfaces, while contact of the surfaces is assumed to be frictionless. Furthermore, there is no contact between the top or the bottom surface of the weld area and the forming tools. During the JCO steps, it is assumed that no slip occurs between the punching press and the top of the steel plate to avoid relative motion between the two surfaces. The analysis is implicit and is performed with ABAQUS/Standard. The steel plate is discretized using four-node, reduced-integration generalized plane strain continuum elements, denoted as CPEG4R.

## 2.2 Constitutive model

During JCO-E manufacturing process the steel plate material is deformed well into the plastic range and is subjected to reverse plastic loading, where the Bauschinger effect appears. A small anisotropic behavior of the steel plate may also occur at the plastic region due to its rolling production process at the steel mill. This anisotropy implies different yield stresses at different directions of the plate material. Therefore, it is important to use a model capable of describing adequately the steel plate material behavior during the elastic-plastic loading and reverse loading conditions, considering this anisotropic behavior in order to predict the final properties and the collapse pressure of the JCO-E pipe. The model should also be able to describe the plastic plateau of the steel material upon initial yielding and the Bauschinger effect under reverse loading conditions. Such a model does not exist in the ABAQUS library of constitutive models, which necessitates the development of a special-purpose user material subroutine, using the differential equations described below. In the present thesis, these equations are numerically integrated and implemented in the finite element model via a user-defined UMAT subroutine; the numerical integration is presented in detail in Section 2.2.2.

### 2.2.1 Governing equations

An enhancement of the cyclic plasticity material model, employed and implemented by Chatzopoulou *et al.* [6] and later by Antoniou *et al.* [18], is developed in the present thesis to account for anisotropic material behavior, following a procedure similar to the one reported in [19]. Hill's anisotropic yield condition, which accounts for orthotropic perfect plasticity [20], is adopted to include the changes in size and position of the yield surface due to workhardening of the material as follows:

$$f_y = \frac{1}{2}(\mathbf{s} - \mathbf{a}) \cdot [\mathbf{N}(\mathbf{s} - \mathbf{a})] - \frac{k^2(\varepsilon_q)}{3} = 0 \quad (2.1)$$

where  $\mathbf{s}$  is the deviatoric stress tensor,  $\mathbf{a}$  is the deviatoric back stress tensor,  $k(\varepsilon_q)$  is a function of the equivalent plastic strain  $\varepsilon_q$  that defines the size of the yield surface and  $\mathbf{N}$  is a fourth-order tensor of material coefficients representing material anisotropy.

The components of the anisotropy tensor  $\mathbf{N}$  are calculated using (a) the tensile yield stresses in the transverse direction  $\sigma_{0,x}$ , in the through-thickness direction  $\sigma_{0,y}$ , in the rolling direction  $\sigma_{0,z}$ , and (b) the yield stresses in pure shear in the (x,y), (y,z), and (x,z) planes denoted as  $\sigma_{0,xy}$ ,  $\sigma_{0,yz}$ ,  $\sigma_{0,xz}$ , respectively. The transverse and the longitudinal directions of the steel plate with respect to the coordinate system are depicted in Figure 2.1. For the purposes of numerical implementation of this model, tensors  $\mathbf{s}$  and  $\mathbf{a}$  are written in vector form:

$$\begin{aligned}\mathbf{s} &= (s_{xx}, s_{yy}, s_{zz}, s_{xy}, s_{yz}, s_{xz}) \\ \mathbf{a} &= (a_{xx}, a_{yy}, a_{zz}, a_{xy}, a_{yz}, a_{xz})\end{aligned}\quad (2.2)$$

and tensor  $\mathbf{N}$  is expressed in the following matrix form:

$$\mathbf{N} = \begin{bmatrix} N_1 + N_2 & -N_1 & -N_2 & 0 & 0 & 0 \\ -N_1 & N_1 + N_3 & -N_3 & 0 & 0 & 0 \\ -N_2 & -N_3 & N_2 + N_3 & 0 & 0 & 0 \\ 0 & 0 & 0 & 2N_{xy} & 0 & 0 \\ 0 & 0 & 0 & 0 & 2N_{yz} & 0 \\ 0 & 0 & 0 & 0 & 0 & 2N_{xz} \end{bmatrix}\quad (2.3)$$

which means that the yield condition in equation (2.1) is written as:

$$f_y = \frac{1}{2}(\mathbf{s} - \mathbf{a})^T \cdot [\mathbf{N}(\mathbf{s} - \mathbf{a})] - \frac{k^2(\varepsilon_q)}{3} = 0\quad (2.4)$$

The elements of the tensor  $\mathbf{N}$  are related to the yield stresses in tension and in shear as follows:

$$N_1 = \left( \frac{1}{\sigma_{0,x}^2} + \frac{1}{\sigma_{0,y}^2} - \frac{1}{\sigma_{0,z}^2} \right) \frac{k^2(0)}{3}\quad (2.5)$$

$$N_2 = \left( \frac{1}{\sigma_{0,z}^2} + \frac{1}{\sigma_{0,x}^2} - \frac{1}{\sigma_{0,y}^2} \right) \frac{k^2(0)}{3}\quad (2.6)$$

$$N_3 = \left( \frac{1}{\sigma_{0,y}^2} + \frac{1}{\sigma_{0,z}^2} - \frac{1}{\sigma_{0,x}^2} \right) \frac{k^2(0)}{3}\quad (2.7)$$



$$N_{xy} = \frac{1}{\sigma_{0,xy}^2} \frac{k^2(0)}{3} \quad (2.8)$$

$$N_{yz} = \frac{1}{\sigma_{0,yz}^2} \frac{k^2(0)}{3} \quad (2.9)$$

$$N_{xz} = \frac{1}{\sigma_{0,xz}^2} \frac{k^2(0)}{3} \quad (2.10)$$

It is assumed that the above components are calculated at the initial yielding stage and do not change during the inelastic deformation history. For an isotropic steel plate material, Hill's yield criterion results in the well-known isotropic von Mises yield criterion. In such a case:

$$\begin{aligned} \sigma_{0,x} = \sigma_{0,y} = \sigma_{0,z} = \sigma_{0,ij} \sqrt{3} = k \\ N_1 = N_2 = N_3 = N_{ij}/3 = 1/3 \end{aligned} \quad (2.11)$$

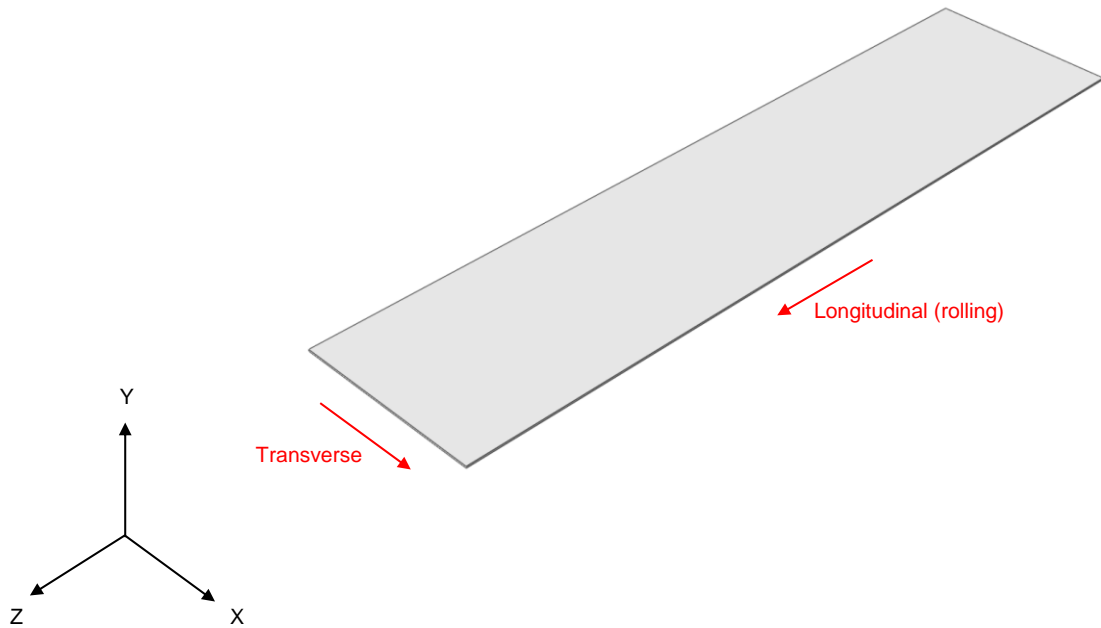


Figure 2.1: A schematic of the steel plate showing transverse and longitudinal directions.

Considering the value of  $\sigma_{0,x}$  as a reference for the size of the yield surface, defining  $Q$  as the maximum change in yield surface size and considering  $b$  as the rate at which the size of the yield surface changes as plastic straining develops, the following equation for function  $k(\varepsilon_q)$  is adopted:

$$k(\varepsilon_q) = \sigma_{0,x} + Q(1 - e^{-b\varepsilon_q}) \quad (2.12)$$

Assuming associated plastic flow, and differentiating the yield function  $f_y$  in equation (2.1) in terms of stress  $\boldsymbol{\sigma}$ , the plastic strain rate tensor  $\dot{\boldsymbol{\varepsilon}}^p$  can be expressed as:

$$\dot{\boldsymbol{\varepsilon}}^p = \dot{\lambda} \frac{\partial f_y}{\partial \boldsymbol{\sigma}} = \dot{\lambda} \mathbf{N}(\mathbf{s} - \mathbf{a}) \quad (2.13)$$

The corresponding equivalent plastic strain rate is defined as:

$$\dot{\varepsilon}_q = \sqrt{\frac{2}{3} \dot{\boldsymbol{\varepsilon}}^p \cdot (\mathbf{N}^{-1} \dot{\boldsymbol{\varepsilon}}^p)} \quad (2.14)$$

Equivalently, taking into account equations (2.13) and (2.14), it is possible to express the rate of plastic multiplier  $\dot{\lambda}$  in terms of  $\dot{\varepsilon}_q$ :

$$\dot{\lambda} = \frac{3}{2} \frac{\dot{\varepsilon}_q}{k(\varepsilon_q)} \quad (2.15)$$

The nonlinear kinematic hardening rule is considered for the evolution of the back stress tensor, initially proposed by Armstrong and Frederick [21]:

$$\dot{\mathbf{a}} = C(\varepsilon'_q) \dot{\boldsymbol{\varepsilon}}^p - \gamma \mathbf{a} \dot{\varepsilon}_q \quad (2.16)$$

where  $\gamma$  is a parameter that determines the rate at which the kinematic hardening modulus decreases with increasing plastic deformation and  $C(\varepsilon'_q)$  is a function of the equivalent cumulative strain  $\varepsilon'_q$ , accumulated during a plastic event. An enhanced version of the classical Armstrong-Frederic model [21] is adopted for  $C(\varepsilon'_q)$ , defined as:

$$C(\varepsilon'_q) = C_0 + Q_b (1 - e^{-c_b \varepsilon'_q}) \quad (2.17)$$

for describing more efficiently the Bauschinger effect and the stress plateau. In the above expression,  $C_0$  is the kinematic hardening modulus at initial yielding,  $Q_b$  is a parameter representing the maximum change of the initial hardening modulus and  $c_b$  is an exponent representing the rate of this change. For positive values of  $c_b$ , negative values of  $Q_b$  and increasing plastic deformation, the value of function  $C(\varepsilon'_q)$  decreases exponentially, which is

consistent with the Bauschinger effect. The stress plateau appears upon initial yielding and extends up to a threshold strain value usually between 0% and 2%; its exact value is determined by experimental data. In the material model, if the equivalent plastic strain is less than this threshold value, function  $C(\varepsilon'_q)$  and parameter  $\gamma$  obtain constant small values, representing the very low hardening of the stress plateau.

Enforcing the consistency condition  $\dot{f}_y = 0$ , the following expression is obtained:

$$\frac{\partial f_y}{\partial \boldsymbol{\sigma}} \cdot \dot{\boldsymbol{\sigma}} + \frac{\partial f_y}{\partial \mathbf{a}} \cdot \dot{\mathbf{a}} + \frac{\partial f_y}{\partial k} \cdot \dot{k} = 0 \quad (2.18)$$

where

$$\dot{k} = \frac{dk(\varepsilon_q)}{d\varepsilon_q} \dot{\varepsilon}_q \quad (2.19)$$

Using equations (2.13), (2.15), (2.16), (2.18), (2.19), and defining tensor  $\boldsymbol{\xi}$  as the tensor difference  $\mathbf{s} - \mathbf{a}$ , one results in the following expression for the equivalent plastic strain rate  $\dot{\varepsilon}_q$ :

$$\dot{\varepsilon}_q = \frac{1}{\left[ \frac{3C(\varepsilon'_q)}{2k(\varepsilon_q)} (\mathbf{N}\boldsymbol{\xi}) \cdot (\mathbf{N}\boldsymbol{\xi}) - \gamma (\mathbf{N}\boldsymbol{\xi}) \cdot \mathbf{a} + \frac{2}{3} k(\varepsilon_q) \frac{dk(\varepsilon_q)}{d\varepsilon_q} \right]} (\mathbf{N}\boldsymbol{\xi}) \cdot \dot{\mathbf{s}} \quad (2.20)$$

Furthermore, using the elasticity equation  $\boldsymbol{\sigma} = \mathbf{D}\boldsymbol{\varepsilon}^e$ , where  $\mathbf{D}$  is the elastoplastic rigidity tensor, and considering that the total strain is the sum of its elastic and plastic part:  $\boldsymbol{\varepsilon} = \boldsymbol{\varepsilon}^e + \boldsymbol{\varepsilon}^p$ , the rate form of the elasticity equation can be written as:

$$\dot{\boldsymbol{\sigma}} = \mathbf{D}(\dot{\boldsymbol{\varepsilon}} - \dot{\boldsymbol{\varepsilon}}^p) \quad (2.21)$$

or equivalently,

$$\dot{\boldsymbol{\sigma}} = \mathbf{D}\dot{\boldsymbol{\varepsilon}} - \dot{\lambda}\mathbf{D}(\mathbf{N}\boldsymbol{\xi}) \quad (2.22)$$

One can readily show that  $\text{tr}(\mathbf{N}\boldsymbol{\xi}) = 0$ , so that  $\mathbf{N}\boldsymbol{\xi}$  is a deviatoric tensor. Therefore,

$$\mathbf{D}(\mathbf{N}\boldsymbol{\xi}) = 2GN\boldsymbol{\xi} \quad (2.23)$$

where  $G$  is the shear modulus. Using the tensor property of equation (2.23) and equation (2.15), equation (2.22) can be expressed as:

$$\dot{\boldsymbol{\sigma}} = \mathbf{D}\dot{\boldsymbol{\varepsilon}} - \frac{3G}{k(\varepsilon_q)} \dot{\varepsilon}_q \mathbf{N}\boldsymbol{\xi} \quad (2.24)$$

Finally, the tangent elastoplastic moduli  $\mathbf{D}^{\text{ep}}$  is calculated by multiplying both sides of equation (2.24) with the  $\mathbf{N}\boldsymbol{\xi}$  term. Subsequently, using equation (2.20), the following expression of the equivalent plastic strain rate  $\dot{\varepsilon}_q$  is obtained:

$$\dot{\varepsilon}_q = \frac{1}{\mathbf{B}} (\mathbf{D}\dot{\boldsymbol{\varepsilon}}) \cdot (\mathbf{N}\boldsymbol{\xi}) \quad (2.25)$$

where

$$\mathbf{B} = 3 \left( \frac{C(\varepsilon_q')}{2k(\varepsilon_q)} + \frac{G}{k(\varepsilon_q)} \right) (\mathbf{N}\boldsymbol{\xi}) \cdot (\mathbf{N}\boldsymbol{\xi}) - \gamma (\mathbf{N}\boldsymbol{\xi}) \cdot \mathbf{a} + \frac{2}{3} k(\varepsilon_q) \frac{dk(\varepsilon_q)}{d\varepsilon_q} \quad (2.26)$$

Combining equations (2.24) and (2.25), and denoting the fourth-order tensor product of two-second order tensors with symbol  $\otimes$ , the incremental stress-strain relation can be written as:

$$\dot{\boldsymbol{\sigma}} = \left[ \mathbf{D} - \frac{1}{\mathbf{B}} \frac{6G^2}{k(\varepsilon_q)} (\mathbf{N}\boldsymbol{\xi}) \otimes (\mathbf{N}\boldsymbol{\xi}) \right] \dot{\boldsymbol{\varepsilon}} \quad (2.27)$$

and the tangent elastoplastic rigidity tensor is

$$\mathbf{D}^{\text{ep}} = \mathbf{D} - \frac{1}{\mathbf{B}} \frac{6G^2}{k(\varepsilon_q)} (\mathbf{N}\boldsymbol{\xi}) \otimes (\mathbf{N}\boldsymbol{\xi}) \quad (2.28)$$

## 2.2.2 Numerical integration and implementation

Following the above formulation of the constitutive model, an implicit integration is developed, based on an “elastic predictor – plastic corrector” scheme suitable for its implementation in a finite element environment. The incremental problem can be stated as follows. At the start of the time  $t = t_n$ , for a given state of the known quantities  $(\mathbf{s}_n, \mathbf{a}_n, \varepsilon_{q,n})$  and a given strain increment  $\Delta\boldsymbol{\varepsilon}$ , the new state parameters at the end of the increment  $(\mathbf{s}_{n+1}, \mathbf{a}_{n+1}, \varepsilon_{q,n+1})$  are sought.

Assuming  $\Delta \boldsymbol{\varepsilon} = \Delta \boldsymbol{\varepsilon}^e$ , elastic prediction takes place first; this process does not involve plastic loading of the material. Following a direct integration of the elasticity equation, the new state parameters at the end of the time increment  $t_{n+1}$  can be written as:

$$\begin{aligned}\mathbf{s}_{n+1} &= \mathbf{s}^{(e)} = \mathbf{s}_n + \mathbf{D}\Delta \boldsymbol{\varepsilon} \\ \mathbf{a}_{n+1} &= \mathbf{a}_n \\ \varepsilon_{q,n+1} &= \varepsilon_{q,n} \\ \varepsilon'_{q,n+1} &= \varepsilon'_{q,n}\end{aligned}\tag{2.29}$$

If the yield criterion is satisfied at the end of the increment “n+1” ( $f_{y,n+1} \leq 0$ ), then elastic prediction is valid and the time increment is elastic. Otherwise, plastic correction needs to be performed based on the following procedure.

Substituting the  $\dot{\lambda}$  term of equation (2.15) into equation (2.13) and integrating over the increment using an Euler-backward integration scheme, one results in the following expression:

$$\Delta \boldsymbol{\varepsilon}^p = \frac{3}{2} \frac{\Delta \varepsilon_q}{k(\varepsilon_{q,n+1})} \mathbf{N} \boldsymbol{\xi}_{n+1}\tag{2.30}$$

Therefore, integrating equation (2.24), the following expression is obtained:

$$\Delta \boldsymbol{\sigma} = \mathbf{D}\Delta \boldsymbol{\varepsilon} - \frac{3G}{k(\varepsilon_{q,n+1})} \Delta \varepsilon_q \mathbf{N} \boldsymbol{\xi}_{n+1}\tag{2.31}$$

which can also be written as:

$$\boldsymbol{\sigma}_{n+1} = \boldsymbol{\sigma}_n + \mathbf{D}\Delta \boldsymbol{\varepsilon} - \frac{3G}{k(\varepsilon_{q,n+1})} \Delta \varepsilon_q \mathbf{N} \boldsymbol{\xi}_{n+1}\tag{2.32}$$

or equivalently,

$$\boldsymbol{\sigma}_{n+1} = \boldsymbol{\sigma}^{(e)} - \frac{3G}{k(\varepsilon_{q,n+1})} \Delta \varepsilon_q \mathbf{N} \boldsymbol{\xi}_{n+1}\tag{2.33}$$

The deviatoric part of the final stress in equation (2.33) is written as:

$$\mathbf{s}_{n+1} = \mathbf{s}^{(e)} - \frac{3G}{k(\varepsilon_{q,n+1})} \Delta \varepsilon_q \mathbf{N} \boldsymbol{\xi}_{n+1}\tag{2.34}$$

Furthermore, integrating the nonlinear kinematic rule, at the end of the time increment, equation (2.16) results in:

$$\mathbf{a}_{n+1} = \frac{1}{1 + \gamma \Delta \varepsilon_q} \left( \mathbf{a}_n + \frac{3C(\varepsilon'_{q,n+1})}{2k(\varepsilon_{q,n+1})} \Delta \varepsilon_q \mathbf{N} \xi_{n+1} \right) \quad (2.35)$$

Combining equations (2.34) and (2.35), the stress difference at the end of the increment  $\xi_{n+1} = \mathbf{s}_{n+1} - \mathbf{a}_{n+1}$  can be expressed as follows:

$$\xi_{n+1} = \left[ \mathbf{W}(\Delta \varepsilon_q) \right] \left( \mathbf{s}^{(e)} - \frac{1}{1 + \gamma \Delta \varepsilon_q} \mathbf{a}_n \right) \quad (2.36)$$

where

$$\left[ \mathbf{W}(\Delta \varepsilon_q) \right] = \left[ \mathbf{I} + \left( \frac{3\Delta \varepsilon_q}{k(\varepsilon_{q,n+1})} \left( \mathbf{G} + \frac{C(\varepsilon'_{q,n+1})}{2(1 + \gamma \Delta \varepsilon_q)} \right) \right) \mathbf{N} \right]^{-1} \quad (2.37)$$

and  $\mathbf{I}$  is the identity tensor. Finally, enforcing the consistency condition of flow rule, the yield condition (2.1) should be satisfied with the new state parameters at the end of the increment “n+1”. Using equation (2.36), the yield condition (2.1) can be written as follows:

$$\begin{aligned} & \left\{ \left[ \mathbf{W}(\Delta \varepsilon_q) \right] \left( \mathbf{s}^{(e)} - \frac{1}{1 + \gamma \Delta \varepsilon_q} \mathbf{a}_n \right) \right\} \cdot \left\{ \mathbf{N} \left( \left[ \mathbf{W}(\Delta \varepsilon_q) \right] \left( \mathbf{s}^{(e)} - \frac{1}{1 + \gamma \Delta \varepsilon_q} \mathbf{a}_n \right) \right) \right\} = \\ & = \frac{2k^2(\varepsilon_{q,n+1})}{3} \end{aligned} \quad (2.38)$$

The above equation is solved in terms of the unknown equivalent plastic strain increment  $\Delta \varepsilon_q$  using the secant iteration method, which constitutes a simplified approximation of the Newton-Raphson scheme. Hence, the unknown  $\Delta \varepsilon_q$  is calculated as:

$$\Delta \varepsilon_{q(i+1)} = \Delta \varepsilon_{q(i)} - f_y(\Delta \varepsilon_{q(i)}) \frac{\Delta \varepsilon_{q(i)} - \Delta \varepsilon_{q(i-1)}}{f_y(\Delta \varepsilon_{q(i)}) - f_y(\Delta \varepsilon_{q(i-1)})} \quad (2.39)$$

The following two initial values are used to initiate this iterative process: (a) zero value for

$\Delta \varepsilon_{q(-1)}$  and (b)  $\Delta \varepsilon_{q(0)} = \frac{\boldsymbol{\sigma}_v^{(e)} - k(0)}{3G + H}$  corresponding to an integration procedure of isotropic

plasticity model with kinematic hardening;  $\sigma_v$  denotes the von Mises stress and  $H$  is the hardening modulus. The above nonlinear procedure is continued until  $\frac{\Delta \varepsilon_{q(i+1)}}{\Delta \varepsilon_{q(i)}} < e$ , where  $e$  is the desired tolerance. The equivalent plastic strains  $\varepsilon_{q,n+1}$  and  $\varepsilon'_{q,n+1}$  at the end of the increment are equal to:

$$\begin{aligned}\varepsilon_{q,n+1} &= \varepsilon_{q,n} + \Delta \varepsilon_q \\ \varepsilon'_{q,n+1} &= \varepsilon'_{q,n} + \Delta \varepsilon_q\end{aligned}\tag{2.40}$$

Finally, substituting the equivalent plastic strain increment  $\Delta \varepsilon_q$  into equations (2.34) and (2.35), and taking into account equation (2.40), the new state of stresses  $\mathbf{s}_{n+1}$  and  $\mathbf{a}_{n+1}$  at the end of the increment are calculated.

### 2.3 Constitutive model calibration

During JCO steps, the steel plate is subjected mainly to bending, which involves tension in the outer part of the plate and compression in the inner part of the plate, and subsequently to pure tension during the expansion step. Considering the following application of external pressure, a loading path consisting of a sequence of tension-compression-tension is considered adequate to describe the loading history.

To calibrate the material model, strip specimens are extracted from both the longitudinal and transverse direction of the steel plate and subjected to tension-compression-tension. These tests are simulated numerically using a “unit cube” finite element model (a single “brick” element), which consist three analysis steps that represent the above cyclic loading, and considering uniaxial stress conditions, by applying appropriate boundary conditions. The material model parameters are appropriately chosen, so that the stress-strain curves obtained from the simulation fit quite well with the corresponding experimental curves in both the longitudinal and transverse direction. The values of material parameters referring to isotropic and kinematic hardening are obtained from cyclic experimental stress-strain curves, following a procedure similar to that described in Abaqus Analysis User’s Guide (Chapter: Models for metals subjected to cyclic loading) [22].

## 2.4 Finite element modelling of Welding (SAW) process

Previous work on the modelling of multi-pass welding process for a LSAW line pipe has been reported by Wen *et al.* [23], where a three-dimensional welding model was used, focusing on the global distortion in the longitudinal (welding) direction, which can be minimized by adjusting the process parameters. In the more recent work by Horn [24], it was concluded that the heat flow in the welding direction is important for the heating and cooling-rate calculations.

In the present thesis, at the end of O-phase and after contact of the two opposite edges is achieved, a three-dimensional thermo-mechanical analysis is performed to simulate the welding process through an auxiliary three-dimensional model, which “communicates” with the main analysis model. This is aimed at providing a more accurate simulation of the material behavior at the vicinity of the weld area, and offering a more realistic description of heat flux than a two-dimensional thermo-mechanical model, for analyzing the welding process. The auxiliary model represents a pipe length, which ensures that the temperature field during the welding passes has reached a steady state. Due to symmetry, only half of the pipe is modeled, using appropriate symmetry boundary conditions on the symmetry plane, as pipe geometry and the welding process are symmetric with respect to the welding line. Modelling of the welding process is carried out by simulating the two multi-electrode welding passes (inside and outside), using a transient coupled temperature-displacement analysis, which comprises the following steps: (a) first pass (inside welding), (b) cooling down to room temperature, (c) second pass (outside welding), and (d) cooling down to room temperature. Thermo-mechanical coupled analysis ensures that in each step during thermal analysis, a mechanical analysis is also simultaneously performed and the corresponding residual stresses are calculated. The pipe is discretized using eight-node, reduced-integration thermally-coupled brick elements, denoted as C3D8RT in ABAQUS/Standard. At the weld area, the size and the number of elements in every cross-section along the pipe is chosen equal to those of the two-dimensional model. At the end of the welding simulation, this enables the auxiliary analysis to “communicate” with the main analysis by transferring the stresses-strains of a weld area cross-section, in which the field of temperatures during welding becomes steady, to the corresponding weld area of the quasi two-dimensional model.



In an arc welding process, the heat source is derived from the welding arc and is quantified by arc power [25]. The power of a single power source is computed by:

$$Q_p = \eta VI \quad (2.41)$$

where the efficiency of welding (SAW) process  $\eta$  is taken equal to 1, according to ISO/TR 17671-1 document [26], and  $V$ ,  $I$  are the arc voltage and the arc current, respectively. For the multi-electrode welding (SAW) process under consideration, the total power (heat input) applied in welding passes is considered equal to the sum of the corresponding electrodes power. It is represented in the form of a double-ellipsoid distribution [27], schematically illustrated in Figure 2.2, and describes the volumetric heat flux traveling along the welding line. The heat source model is implemented via a user-defined DFLUX subroutine. Considering a fixed Cartesian coordinate system  $(x, y, z)$  and a moving Cartesian coordinate system along the  $z$  axis  $(x, y, \zeta)$ , where  $\zeta = z - vt$ , the description of the welding heat source, traveling along welding direction with constant velocity  $v$ , includes the front ( $q_f$ ) part and the rear ( $q_r$ ) part and is expressed as follows:

$$\begin{aligned} q_f(x, y, \zeta) &= \frac{6\sqrt{3}f_f \eta Q_T}{abc_f \pi \sqrt{\pi}} \exp\left(-\frac{3x^2}{a^2} - \frac{3y^2}{b^2} - \frac{3\zeta^2}{c_f^2}\right) \forall (x, y, \zeta \geq 0) \\ q_r(x, y, \zeta) &= \frac{6\sqrt{3}f_r \eta Q_T}{abc_r \pi \sqrt{\pi}} \exp\left(-\frac{3x^2}{a^2} - \frac{3y^2}{b^2} - \frac{3\zeta^2}{c_r^2}\right) \forall (x, y, \zeta < 0) \end{aligned} \quad (2.42)$$

where  $\eta$  is the welding efficiency, and  $Q_T$  is the total heat input. Parameters  $a, b, c_f, c_r$  are associated with the dimension of the heat source and are chosen using a weld macrograph of the pipe, so that the size of the desired melted zone is accurately obtained. The fractions of deposited heat, denoted as  $f_f$  and  $f_r$ , are the heat input proportions in the front and rear quadrants, respectively, where  $f_f + f_r = 2$ , as proposed by Goldak *et al* [27]. During the welding process, the pipe temperature increases due to the thermal load input, but meanwhile, heat losses including natural convection and radiation to the environment from the pipe surfaces are considered in the model.

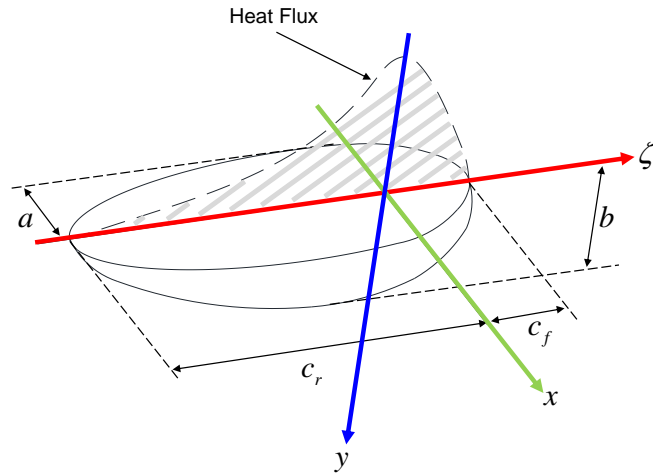


Figure 2.2: Schematic representation of the double ellipsoidal heat source.

The auxiliary three-dimensional model employs the  $J_2$ -flow theory of plasticity with isotropic hardening, where the total strain can be decomposed into three components, namely elastic strain, plastic strain, and thermal strain. The corresponding welding residual stresses are affected by the value of thermal expansion [28]. SAW process is associated with high heat input and high dilution [29] and, as a result, the properties of the filler material are assumed to be same as those of the base metal. During inside welding, the elements corresponding to the not-yet-deposited filler material (outside welding) are considered as thermally and mechanically “inactive” (or “invisible”), and are practically non-existent in the model until the outside welding step starts. Thermal “invisibility” means that the material cannot store and conduct heat, which is obtained by setting specific heat and thermal conductivity equal to zero, while mechanical “invisibility” means that mechanical strength and rigidity of the material are almost zero, so that these elements are mechanically non-existent and cannot sustain any stress. During the thermo-mechanical analysis, to prevent stress being applied to the melted metal, the thermal expansion coefficient is set to be zero above the melting temperature [30]. Furthermore, temperatures exceeding melting temperature cause the effect of stress-free annealing, which resets the accumulated plastic strain and, therefore, the material work-hardening [24]. This stress-free annealing effect is taken into account in the present finite element analysis by setting the accumulated plastic strain equal to zero at a particular element if its temperature reaches or exceeds the melting temperature.

## 2.5 Validation of the numerical model

During the JCO-E cold forming process, stresses and deformations are introduced into the pipe material. As a result, the stress-strain response of JCO-E pipe material is substantially modified with respect to the one of plate material. At the end of the JCO-E process, the mechanical properties of line pipe material are evaluated experimentally. Strip specimens for compressive and tensile testing are extracted from the outer (OUT) and the inner (IN) parts of pipe wall, from both the longitudinal (L) and transverse (T) direction, as shown in Figure 2.3. Sampling is performed at 90-degree, 180-degree and 270-degree position. In order to avoid any kind of misleading information during the material characterization, special care was taken regarding the traceability of the specimens. Namely, the longitudinal direction of the JCO-E pipe coincides always with the longitudinal direction of the initial steel plate (Figure 2.1), as well as the inner and the outer surface of the pipe coincide always with the corresponding inner and the outer surface of the initial steel plate.

To perform the validation of the finite element model with a fair comparison with the experimental results, a numerical simulation of the above experimental procedure is attempted for the corresponding locations, considering a “unit cube” finite element model with uniaxial stress conditions. Input for this “unit cube” model is provided by the finite element model, which simulates the manufacturing process. Throughout the finite element simulation of manufacturing process, the stress-strain history at various locations is recorded. After unloading from the expansion phase, the (residual) stress, strain and all solution-dependent variables at a specific integration point, which is near the through thickness location where specimen is extracted from, are used as initial variables in the “cube” model. In this model, a first step with zero external loading is performed in order to simulate the strip specimen extraction from the line pipe, which is associated with “stress release”. At this step, the plastic deformations developed during the manufacturing process are maintained, but the residual stresses are released representing the exact conditions after the extraction of specimen from the pipe. Subsequently, uniaxial loading is applied in the “unit cube” in longitudinal or in transverse direction, and the corresponding stress-strain curve is obtained. The predicted response at the 270-degree position is the same with the one at the 90-degree, due to the symmetry of forming process.

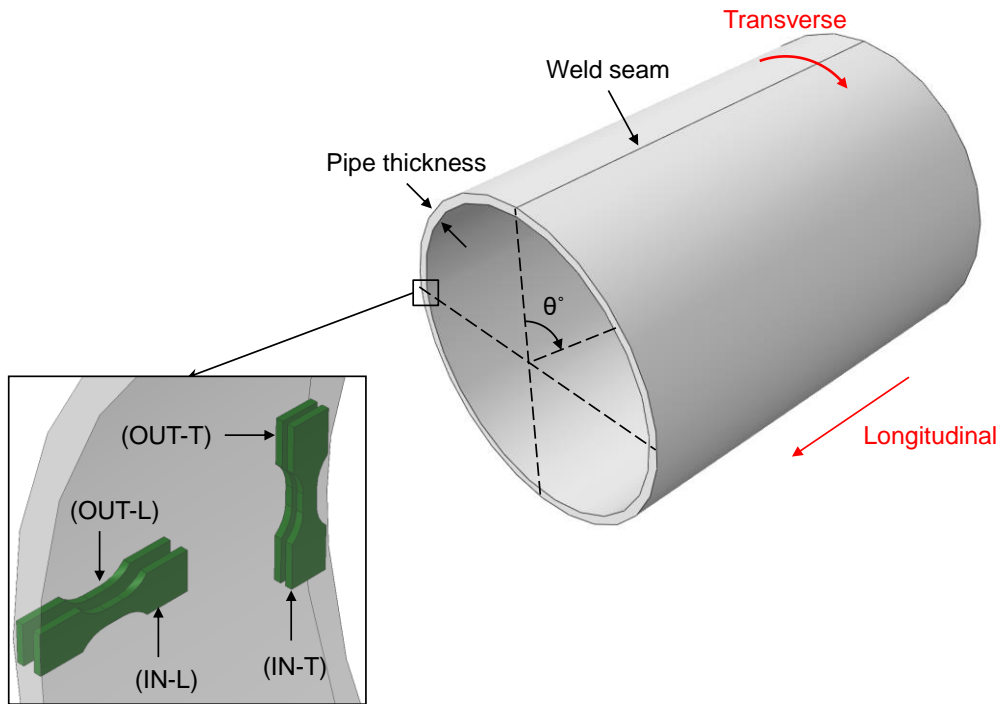


Figure 2.3: Location of the strip specimens extracted from the JCO-E pipe.

## 2.6 Conclusions

A generalized plane strain finite element model of the JCO-E manufacturing process is described, which takes into account the entire deformation history of the pipe, from the initial steel plate configuration to the final JCO-E pipe product. An anisotropic combined-hardening constitutive model is presented to incorporate a description of the steel plate material behavior under the finite element modelling of JCO-E forming process. The welding process is also simulated and the corresponding welding residual stresses-strains are calculated using an auxiliary thermo-mechanical analysis. At the end of simulation of JCO-E process, the finite element model is validated by comparing material properties of the actual pipe with corresponding ones obtained numerically. Finally, the finite element model is capable of predicting the response of the pipe under uniform external pressure and calculating its collapse pressure, accounting rigorously for the residual stresses and the geometric configuration of the line pipe after fabrication.

## **Chapter 3 - Applications of finite element analysis**

### **3.1 Relatively thin-walled JCO-E pipe ( $D/t=34.67$ )**

The methodology for simulating the JCO-E manufacturing process (Chapter 2) is applied first to a 26-inch-diameter X65 line pipe with nominal thickness of 19.05mm, manufactured by Corinth Pipeworks S.A and designed for offshore applications. The line pipe has a diameter-to-thickness ratio equal to 34.67, and it is considered as a relatively thin-walled pipe. Specimens are extracted from the steel plate material and cyclic test results are used to calibrate the constitutive model. Following the data provided by the pipe mill, including the steel plate characteristics, the forming and the welding parameters, the JCO-E process is simulated. Geometric characteristics and material properties of the line pipe obtained from the numerical analysis are compared with corresponding measurements from the pipe mill and experimental results of the pipe material, respectively.

Figure 3.1 shows a part of the finite element mesh employed for both the main part of the plate and the weld area. For the main part of the plate, eight elements are employed through the plate wall thickness, while the size of elements along the plate width (W) is selected to be 1/4 of the plate wall thickness (WT). The finite element mesh at the weld area is shown with different color in Figure 3.1. It corresponds to the size and the number of elements at the weld area of the auxiliary model and is quite dense for increasing the accuracy of the welding process simulation. The finite element mesh for the numerical simulation of welding (SAW) process is shown in Figure 3.2.

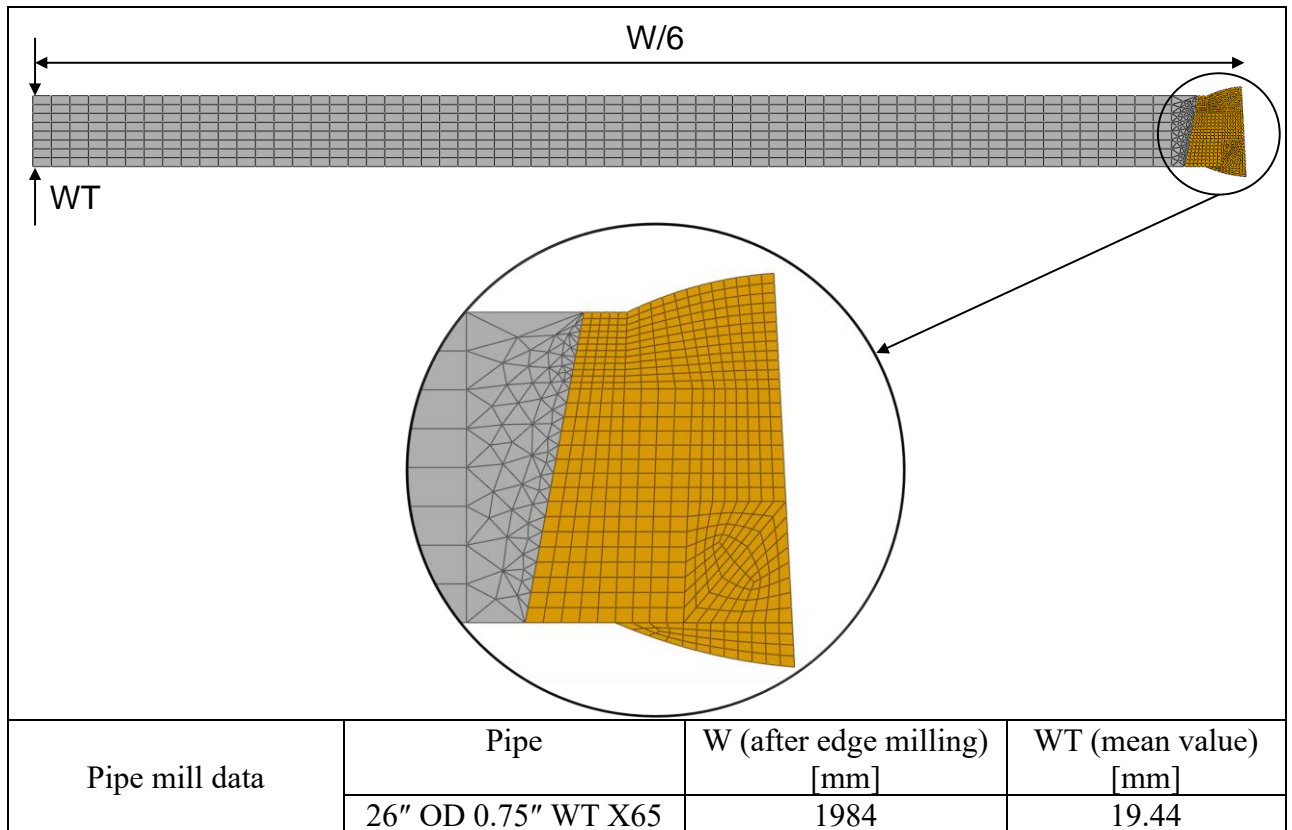


Figure 3.1: A part of the finite element mesh of the steel plate, corresponding to 1/6 of the plate width.

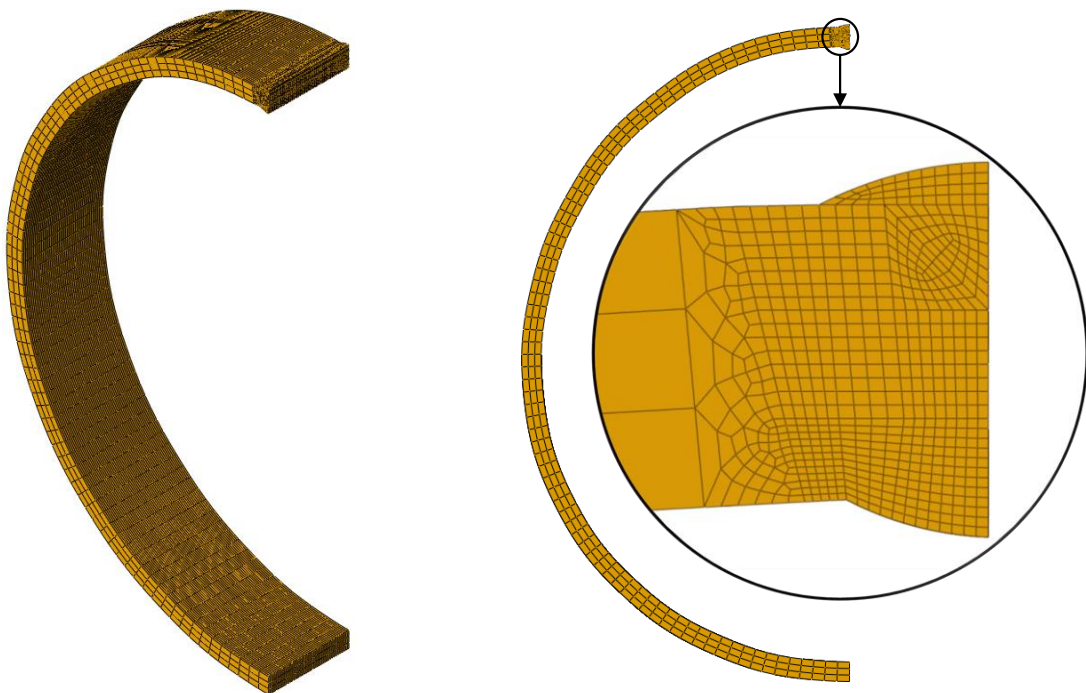


Figure 3.2: The finite element mesh of the auxiliary three-dimensional (welding) model.

### 3.1.1 Material testing and model calibration

Twenty test specimens are extracted from both the inner (IN) and the outer (OUT) part of plate wall, in the longitudinal (L) and the transverse (T) direction, at different locations along the plate length and across the plate width (W), as shown in Figure 3.3. These specimens are subjected to tension-compression-tension testing. In the present research, this testing has been conducted at University of Thessaly, following the provisions of SEP 1240 guideline [31] for the fabrication of specimens. Figure 3.4 shows the experimental setup, where the applied strain is measured with a dynamic extensometer, as well as an anti-buckling device is used to prevent buckling during testing.

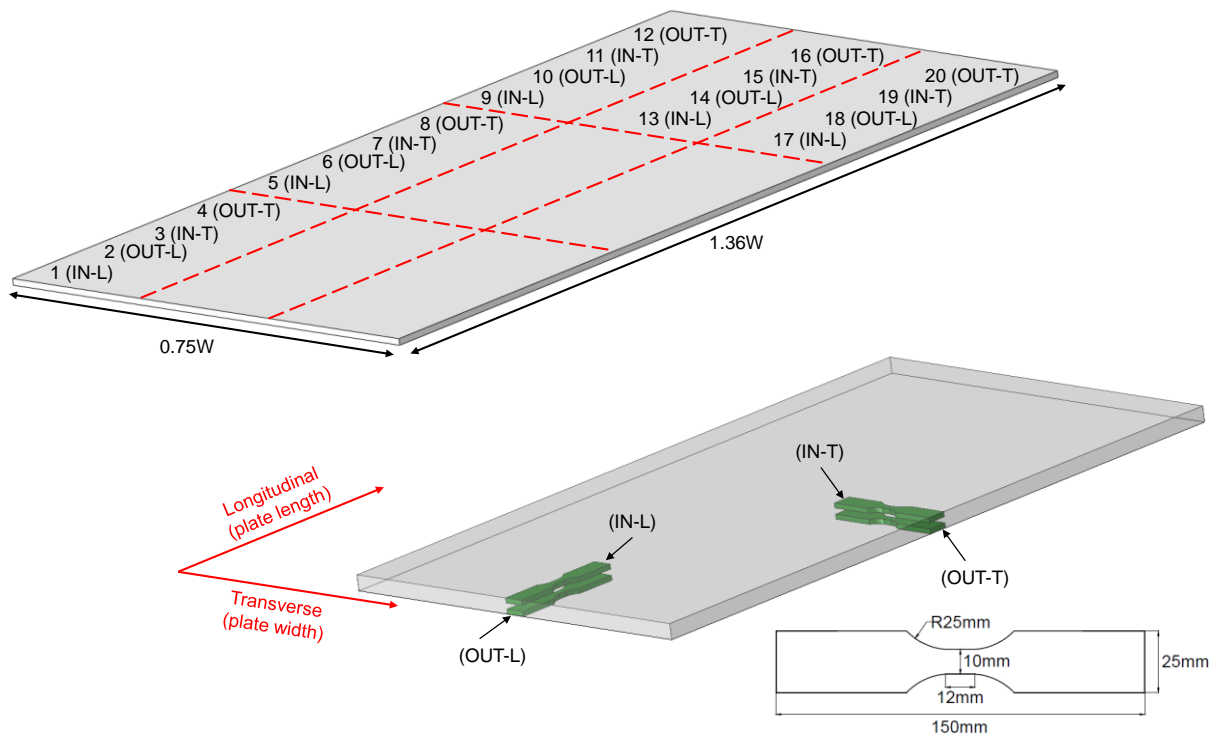


Figure 3.3: Adopted notation and position of tested specimens with respect to plate geometry.

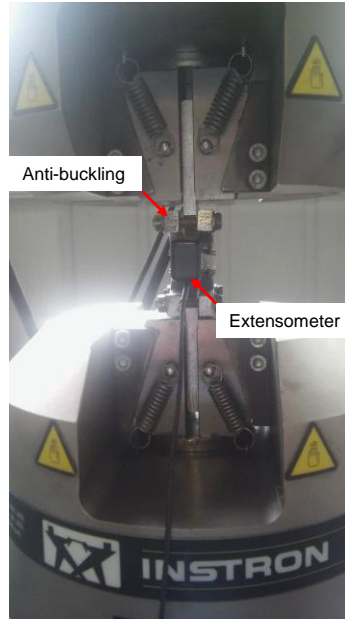


Figure 3.4: The experimental strain-controlled setup used for cyclic tests.

Typical experimental results referred to the tensile yield stress of the material at initial yielding of the coupon (before the application of reverse plastic loading) are presented in Figure 3.5; a stress-strain curve from a full-thickness tensile specimen, fabricated according to the recommendations of ISO 6892-1 [32], is also included to compare with the non-full-thickness test specimens. The plate material does not exhibit a significant variation in terms of anisotropy; an example of this negligible anisotropic response is depicted in Figure 3.6. Furthermore, experimental results from different locations along plate width and length are presented in Figure 3.7. The main observations from those tests are that (a) the yield stress of steel plate material in the longitudinal direction is slightly lower compare to the corresponding yield stress in the transverse direction, (b) from the variations occurred between the longitudinal and the transverse direction, the plate can be considered homogeneous in respect to its physical tensile properties.

After initial yielding, the coupon is subjected to reverse plastic loading and re-loading, where the Bauschinger effect appears. Two sets of material parameters denoted as MAT1 and MAT2, are considered for the description of steel plate material behavior during elastic-plastic loading conditions, assuming that the yield stress in the thickness direction ( $\sigma_{0,y}$ ) is equal to the yield stress in the longitudinal direction ( $\sigma_{0,z}$ ). In both sets, the Young's modulus is 210GPa and the Poisson's ratio equals to 0.30. Material parameters are also listed in Table



3.1, where anisotropy is expressed in terms of the anisotropy constants  $S_y = \sigma_{0,y}/\sigma_{0,x}$  and  $S_z = \sigma_{0,z}/\sigma_{0,x}$ . The corresponding material models exhibit different description of the Bauschinger effect. Stress-strain curves as obtained from the coupon experiments and the calibration of the material models (MAT1, MAT2) are shown in Figure 3.8.

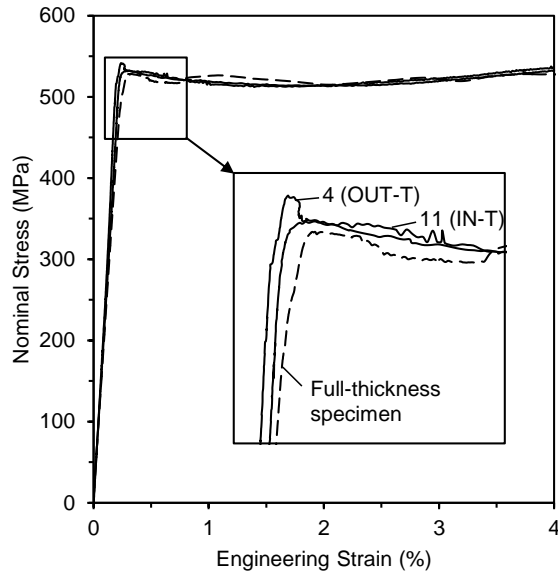


Figure 3.5: Measured tensile stress-strain response in the transverse direction of the plate.

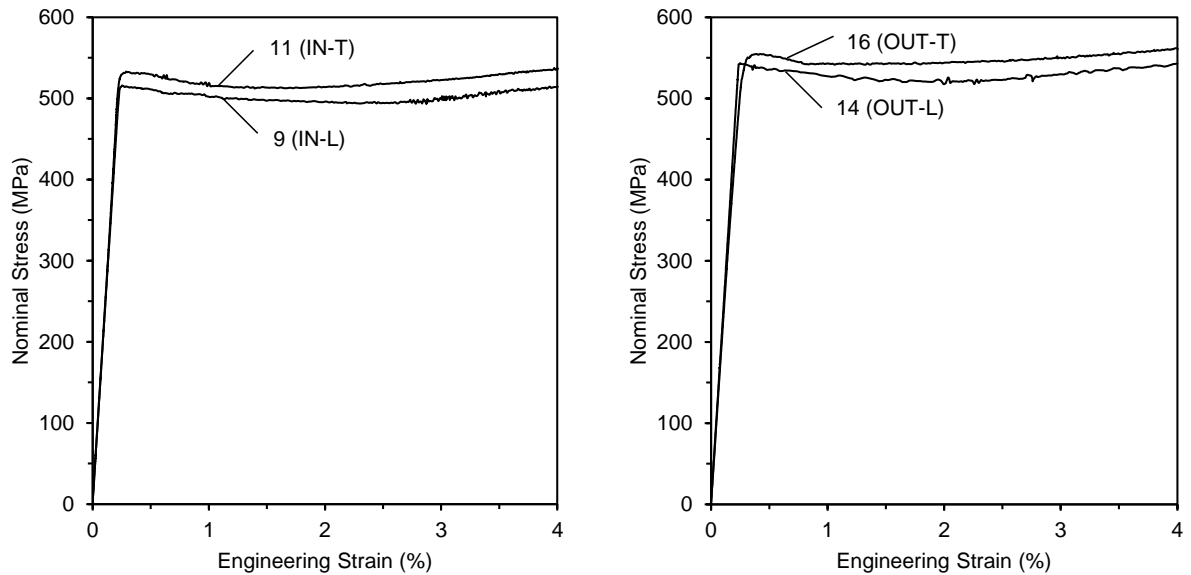


Figure 3.6: Stress-strain curves of the steel plate in the transverse and longitudinal direction of the plate.

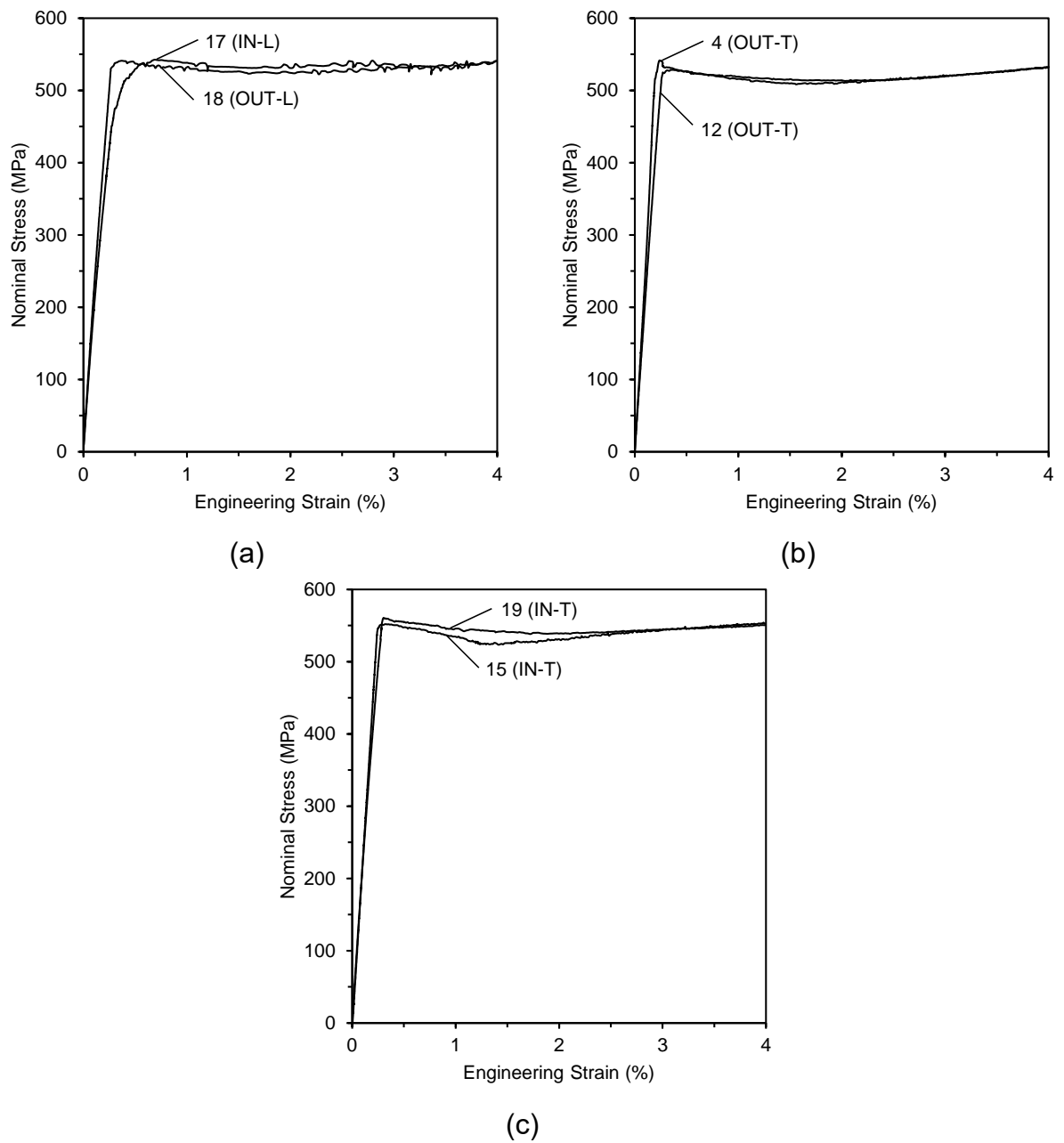


Figure 3.7: Stress-strain curves showing the homogeneity of the steel plate; (a) across the thickness of the plate (IN vs OUT), (b) along the plate length, (c) across the plate width.

Table 3.1: Material parameters used in modelling the X65 steel material

| model | $\sigma_{0,x}$<br>(MPa) | $S_y$ | $S_z$ | Q<br>(MPa) | b   | $\gamma$ | $C_0$<br>(MPa) | $Q_b$<br>(MPa) | $c_b$ |
|-------|-------------------------|-------|-------|------------|-----|----------|----------------|----------------|-------|
| MAT1  | 520                     | 0.94  | 0.94  | -30        | 60  | 30       | 10,000         | -7,500         | 150   |
| MAT2  |                         |       |       | -180       | 100 | 180      | 120,000        | -90,000        | 600   |

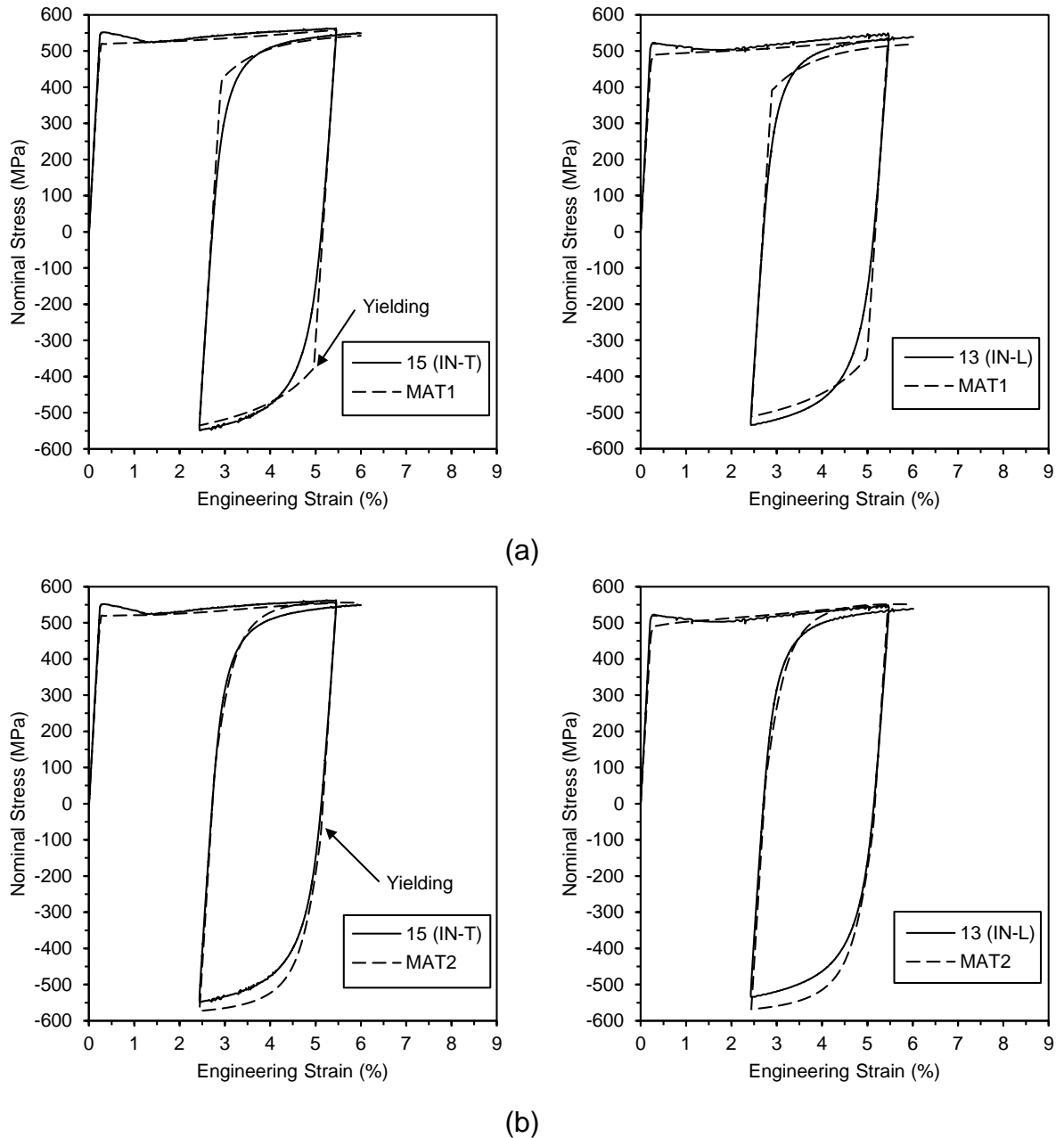


Figure 3.8: Stress-strain diagrams, including reverse loading and re-loading from the steel plate experiments, and the corresponding numerical fitting using (a) MAT1 material properties, (b) MAT2 material properties.

### 3.1.2 Modelling of pipe fabrication process

The crimping and JCO forming process induce non-uniform stresses in the plate material; the JCO process consists of fifteen punching steps. The corresponding values of von Mises stress for the MAT1 set of material parameters, during these stages of fabrication, are shown in Figure 3.9. Before unloading from the third punching step, the corresponding plastically-deformed region in the plate material, obtained from the forming process, is illustrated in Figure 3.10. Upon simulation of JCO forming process, the opening width or “gap” between the two plate edges, depicted in Figure 3.11, for the two sets of material parameters (MAT1 and MAT2) is in accordance with the corresponding measurements resulted from the pipe mill production line. Subsequently, the gap between the two plate edges is closed by applying mechanical loading at the exterior of their surfaces.

The pipe geometry obtained after the closure of “gap” is used to develop the auxiliary three-dimensional model for the simulation of welding (SAW) process. The auxiliary model communicates directly with the quasi two-dimensional model and refers to a pipe length  $L$  equal to 100mm. The following welding process parameters, provided by the pipe mill, are used as input in the heat source model:  $Q = 3.88 \text{ KJ/mm}$ ,  $v = 1.91 \text{ m/min}$  for the first pass and  $Q = 5.04 \text{ KJ/mm}$ ,  $v = 2.00 \text{ m/min}$  for the second pass. The temperature-dependent thermo-mechanical properties of X65 steel used in the present study are similar to those reported in [30]. Based on the work of Nezamdost *et al.* [33], the melting point of X65 steel is  $1493^\circ\text{C}$  and the heat-affected zone (HAZ) refers to a non-melted area of metal, where material has been heated to temperatures in the range of  $715\text{-}1440^\circ\text{C}$ . To model the solid-liquid transformation, the latent heat of fusion  $2.10 \text{ GJ/m}^3$  is used, a value suggested by Bang *et al.* [30]. The heat losses at the free surfaces of pipe have been modeled by prescribing a convective heat coefficient of  $20 \text{ W/m}^2\text{K}$ , an emissivity of 0.8 and setting the room/ambient temperature at  $25^\circ\text{C}$ .

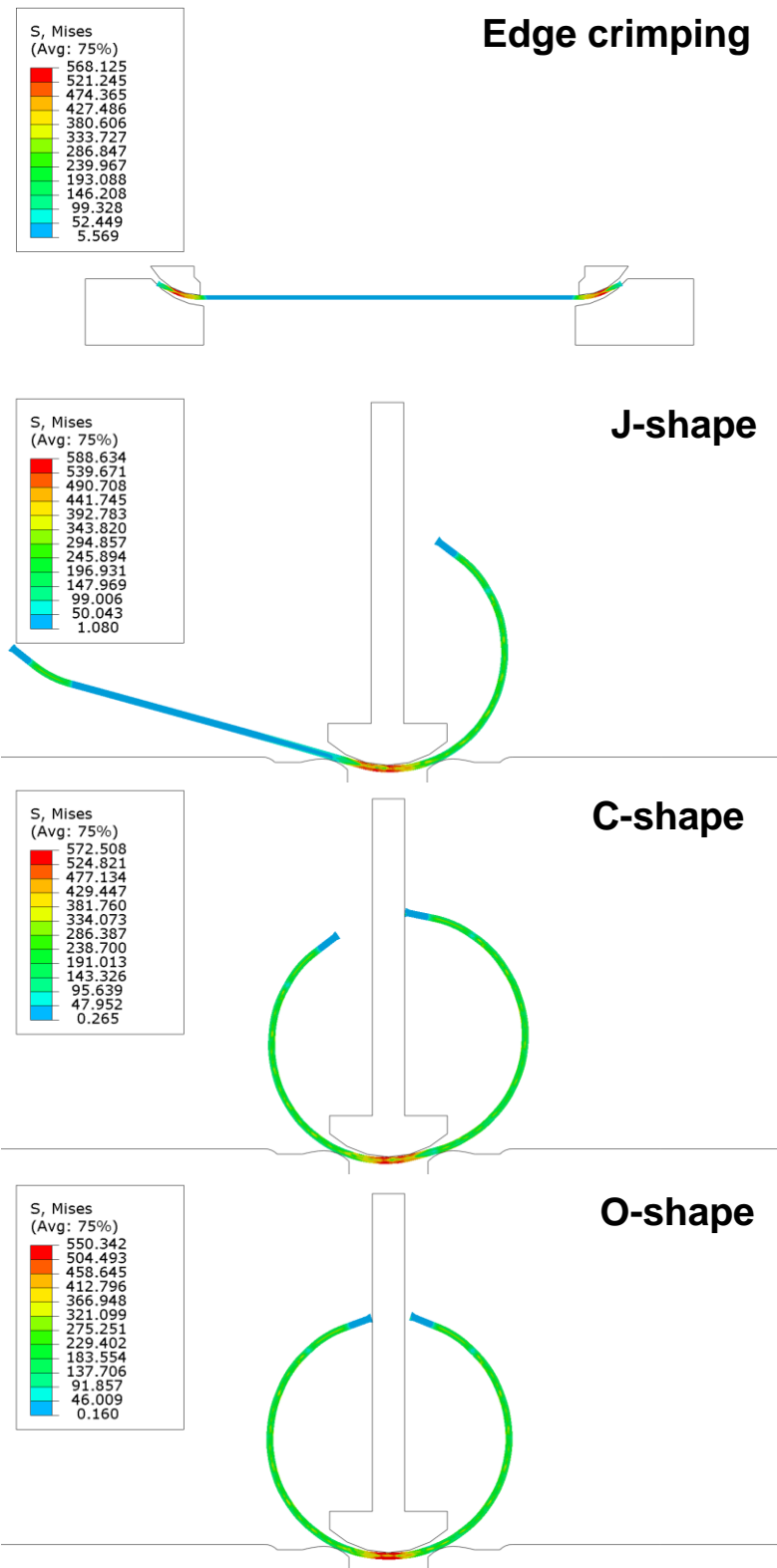


Figure 3.9: Plate configuration of the forming process prior to welding (MAT1 set of material parameters).

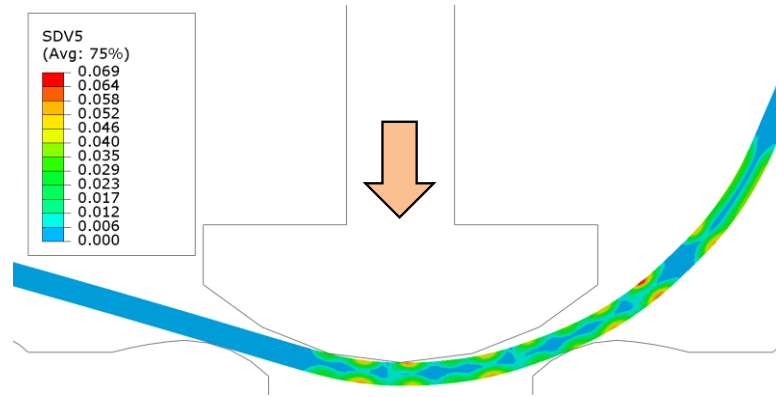


Figure 3.10: Equivalent plastic strain distribution at the third punching step.

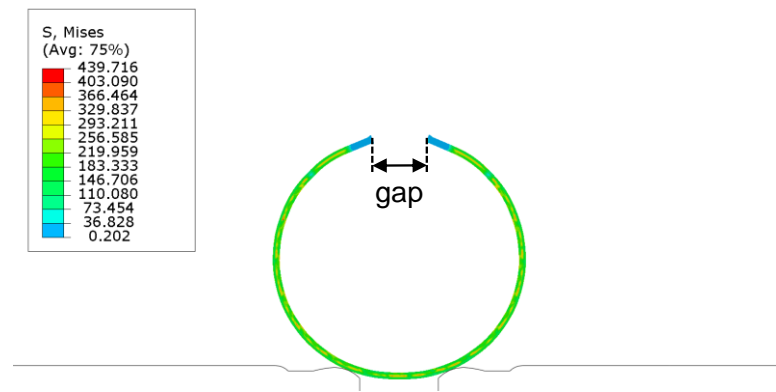


Figure 3.11: Plate configuration after the JCO forming; the gap between the two edges is compared with measurements from the pipe mill.

The distribution of von Mises stress during the second pass (outside welding) is depicted in Figure 3.12. Upon completion of the stage of welding, with the auxiliary three-dimensional analysis, the residual stresses and strains computed at the weld area cross-section shown in Figure 3.12e with black solid lines are transferred to the two-dimensional model for continuing the simulation of cold forming process. The temperature distribution of the selected weld area cross-section obtained by the finite element analysis at the first and the second pass is illustrated in Figure 3.13.

Upon completion of the welding process simulation, the expansion stage of the line pipe is simulated using twelve segments in the expander. During the expansion stage, the von Mises stress distribution, and the corresponding circumferential stresses at 90 degrees from the weld seam, calculated at the integration points across the pipe thickness, are shown in Figure 3.14 for: (a) the JCO pipe, where the expander segments are not in contact with the

inner surface of the pipe and considering that their displacement is equal to zero, (b) the pipe before unloading from the expansion stage, and (c) the JCO-E pipe (after removing of the expander segments). The stresses in JCO pipe are increased during the outward displacement of the segments, due to the imposed tensile deformation, while after unloading, there is a significant reduction and homogenization of these stresses, so that the net tension in the pipe wall is zero.

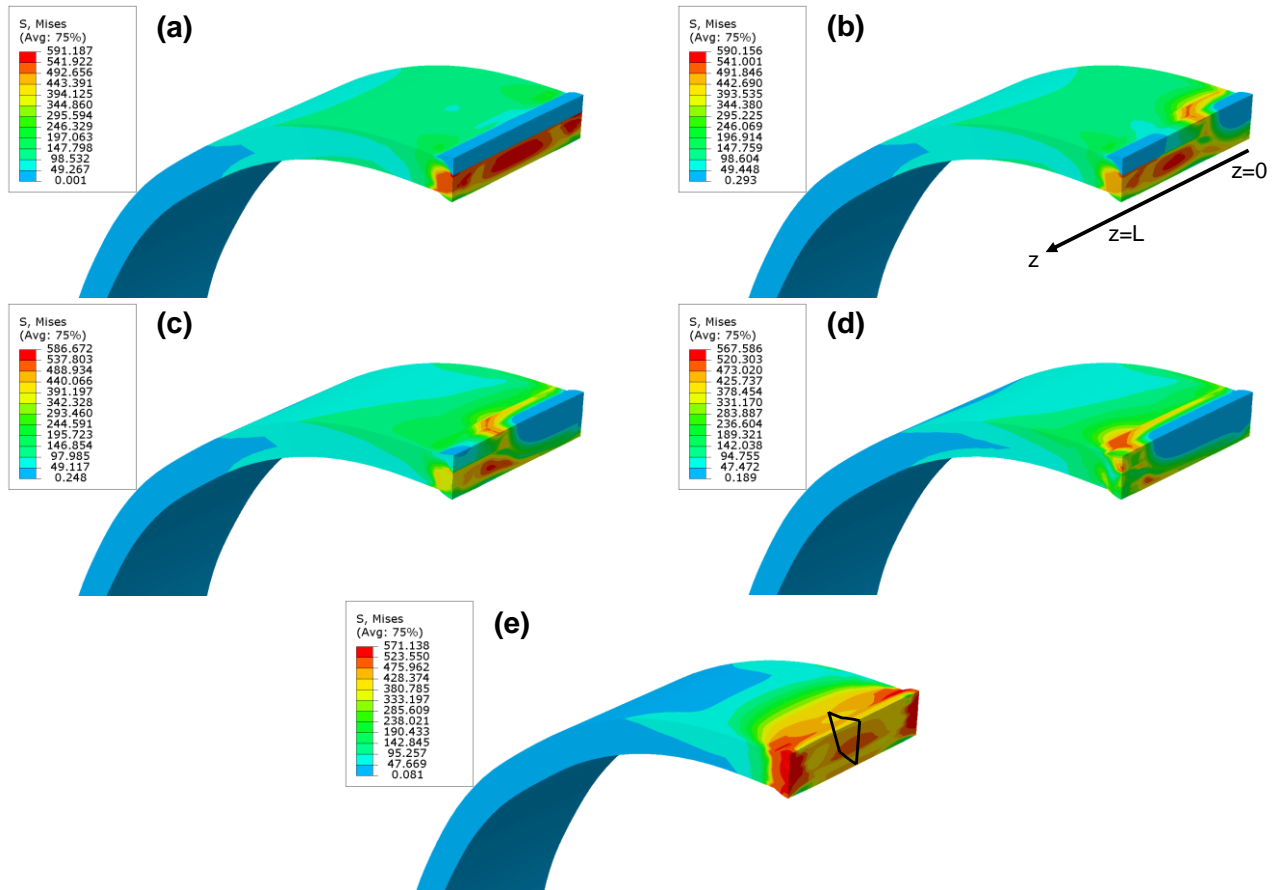


Figure 3.12: Von Mises stress distribution in the auxiliary model: (a) before the outside welding step starts, and at different locations of the heat source during outside welding, namely: (b)  $z = L/4$ , (c)  $z = L/2$ , (d)  $z = 3L/4$ , and (e) at the end of the welding simulation.

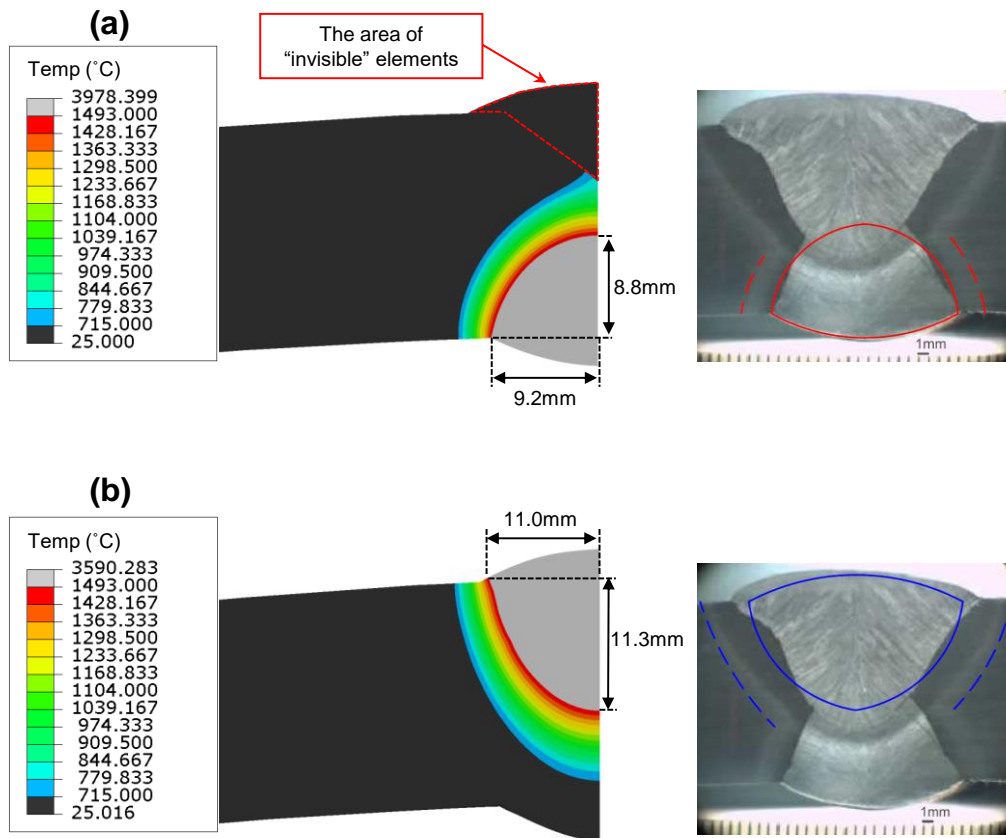


Figure 3.13: Comparison between the predicted temperature field of the selected weld area cross-section and the weld macrograph provided by Corinth Pipeworks S.A.; (a) first pass, corresponding to inside welding, and (b) second pass, corresponding to outside welding.

The geometric configuration of pipe at the end of JCO-E manufacturing process obtained numerically is summarized in Table 3.2 and is compared with the corresponding measurements provided by the pipe mill; the predicted value of JCO-E pipe diameter (inside or outside) refers to the mean value of the diameters calculated at 30, 60, 90, 120, and 150 degrees from the weld seam. Both MAT1 and MAT2 material properties result in a final product with geometric characteristics in a very good agreement with the pipe mill measurements.



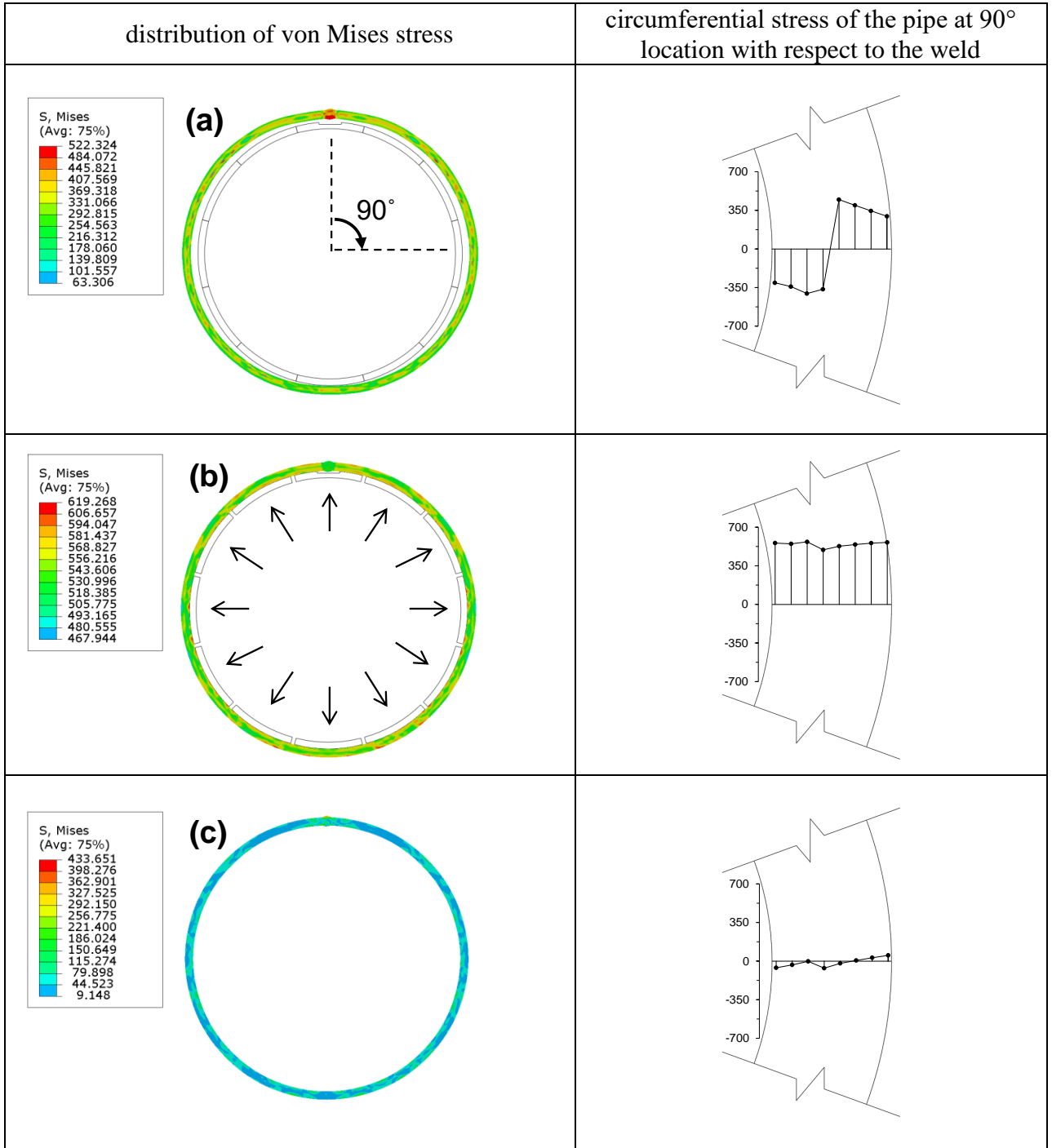


Figure 3.14: Distribution of von Mises stress in the pipe; (a) at initial position of the expander segments (JCO pipe), (b) before unloading from the expansion phase, (c) after unloading from the expansion phase (JCO-E pipe).

Table 3.2: Geometric characteristics of the JCO-E pipe

|   | pipe mill | FEM<br>MAT1 material<br>properties | FEM<br>MAT2 material<br>properties |
|---|-----------|------------------------------------|------------------------------------|
| wall thickness 90° from the weld seam (mm)  | 19.17     | 19.23                              | 19.21                              |
| wall thickness 180° from the weld seam (mm) | 19.20     | 19.26                              | 19.23                              |
| outer diameter of the pipe (mm)             | 661.70    | 661.79                             | 661.87                             |
| inner diameter of the pipe (mm)             | 623.30    | 623.29                             | 623.36                             |

### 3.1.3 Mechanical properties of JCO-E pipe

Using the experimental setup shown in Figure 3.4, monotonic uniaxial tests are conducted on specimens extracted from JCO-E pipe; the anti-buckling device is attached to the specimen in case of compressive testing to prevent structural instability (buckling) of the specimen. In the present thesis, the geometry of these specimens follows the provisions of SEP 1240 guideline [31]. A corresponding numerical procedure, which simulates the extraction of specimens and their subsequent uniaxial loading as described in Section 2.5, is performed in elements located across the thickness of pipe, at 90-degree, 180-degree and 270-degree position. The elements at the 90-degree position are depicted in Figure 3.15; “1, 2, 3, 4” refer to the elements at the inner half and “5, 6, 7, 8” refer to the elements at the outer half of the pipe wall. This numbering is the same for the corresponding elements at 180-degree and 270-degree position.

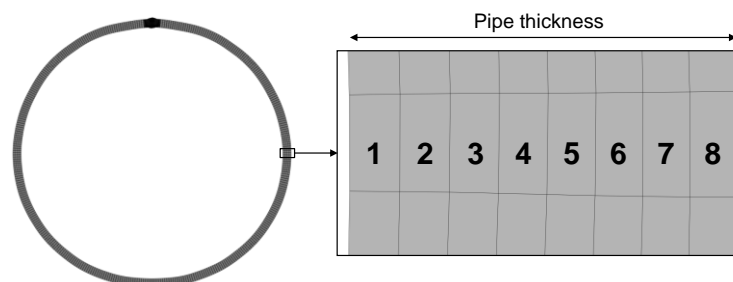


Figure 3.15: Numbering of elements at 90-degree position, across the pipe thickness.

The compressive stress-strain response of JCO-E pipe material, as obtained from the experiments on strip specimens and the corresponding predictions using the MAT1 material properties, in the transverse and the longitudinal direction are depicted in Figure 3.16 and Figure 3.17, respectively. In both longitudinal and transverse direction, the value of yield strength  $R_{10.5}$  at the inner part of pipe wall is higher compared to the corresponding value at the outer part. Furthermore, the cold-forming process, and in particular the expansion stage, degrades the compressive properties of JCO-E pipe material in the transverse direction, as shown in Figure 3.18. In this figure, the stress-strain curves of steel plate material, presented in Section 3.1.1, are compared with corresponding compressive stress-strain curves of JCO-E pipe material. In addition, there exists a certain non-homogeneity with respect to the pipe thickness, attributed to the forming process.

Measured and predicted tensile stress-strain curves in the transverse direction of JCO-E pipe are depicted in Figure 3.19. The predicted curves are obtained using the MAT1 material properties. The measured yield strength  $R_{10.5}$  at the 270-degree position exhibits higher value at the inner part with respect to the corresponding value at the outer part of the pipe wall, while for the 90-degree and 180-degree the variation is insignificant. Furthermore, post-yield hardening is smaller with respect to the corresponding one observed in the compressive response (Figure 3.16). In the longitudinal direction, the tension response of the pipe material at the inner and the outer part of pipe wall is quite similar to the corresponding compression response presented in Figure 3.17. The comparison between the predicted and measured stress-strain curves (tensile and compressive) is considered satisfactory. In the transverse direction, the measured values of yield strength  $R_{10.5}$  for both compression and tension are summarized in Table 3.3.

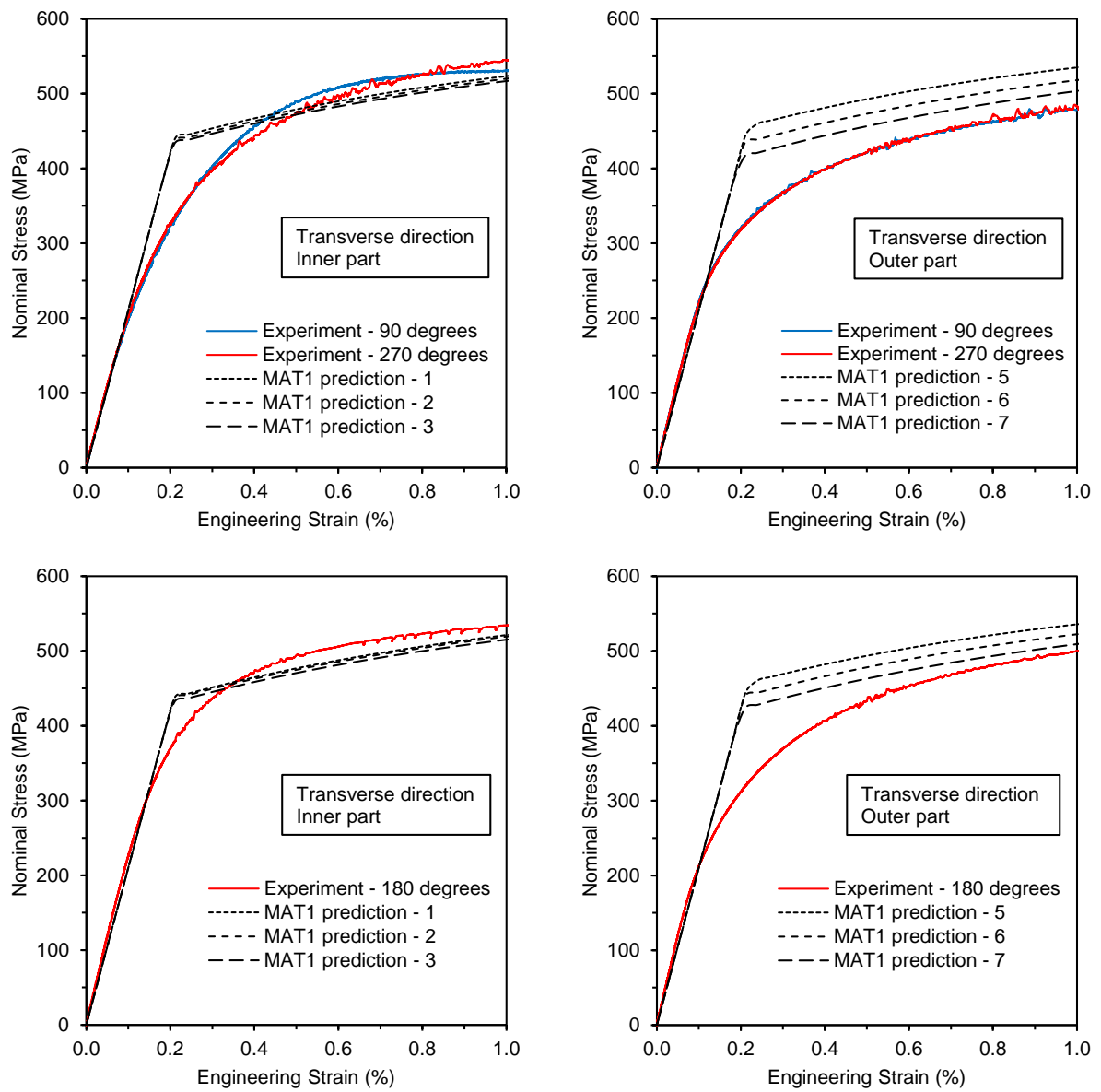


Figure 3.16: Measured and predicted compressive stress-strain response in the transverse direction of the pipe.

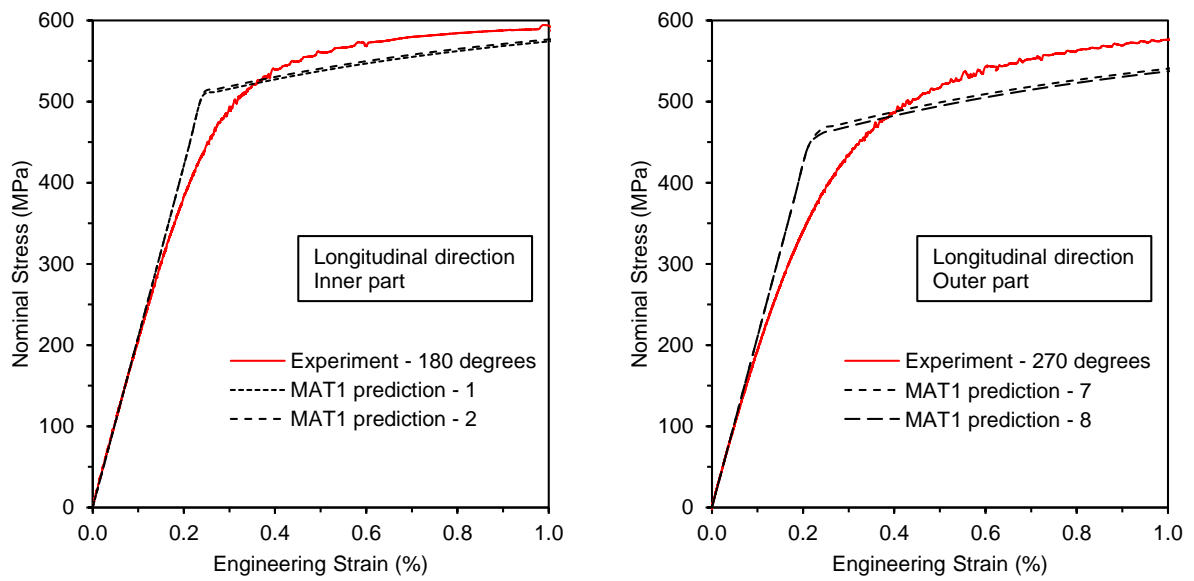


Figure 3.17: Measured and predicted compressive stress-strain response in the longitudinal direction of the pipe.

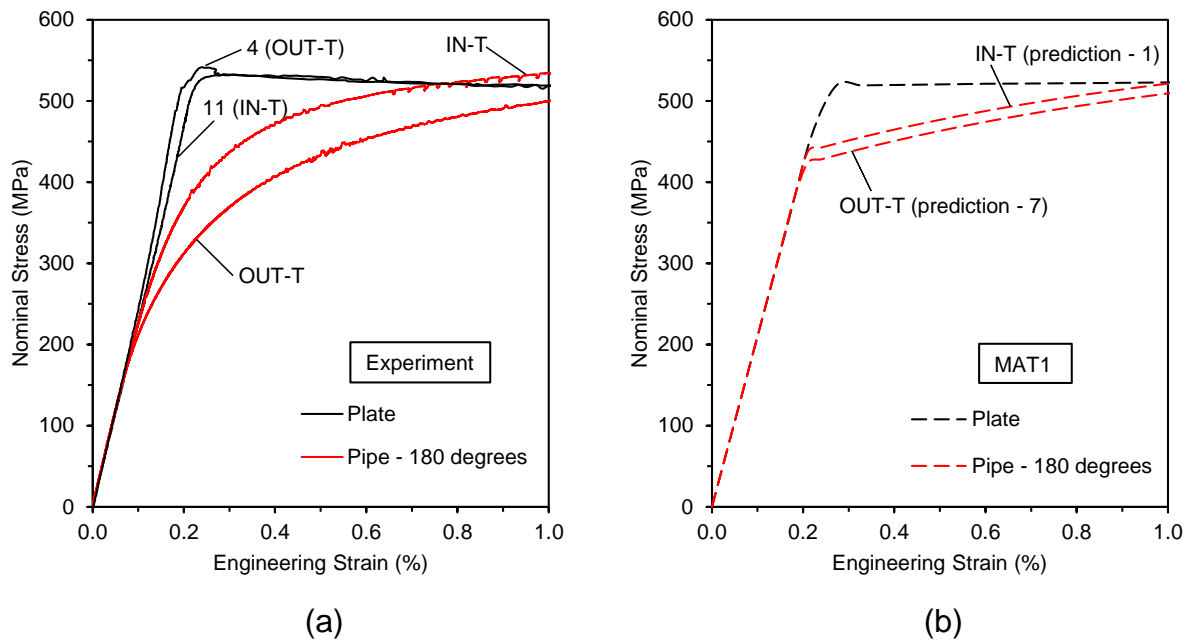


Figure 3.18: Transverse stress-strain response of the plate material in comparison with the JCO-E pipe material tested in compression, as obtained from (a) experiments and (b) MAT1 material model.

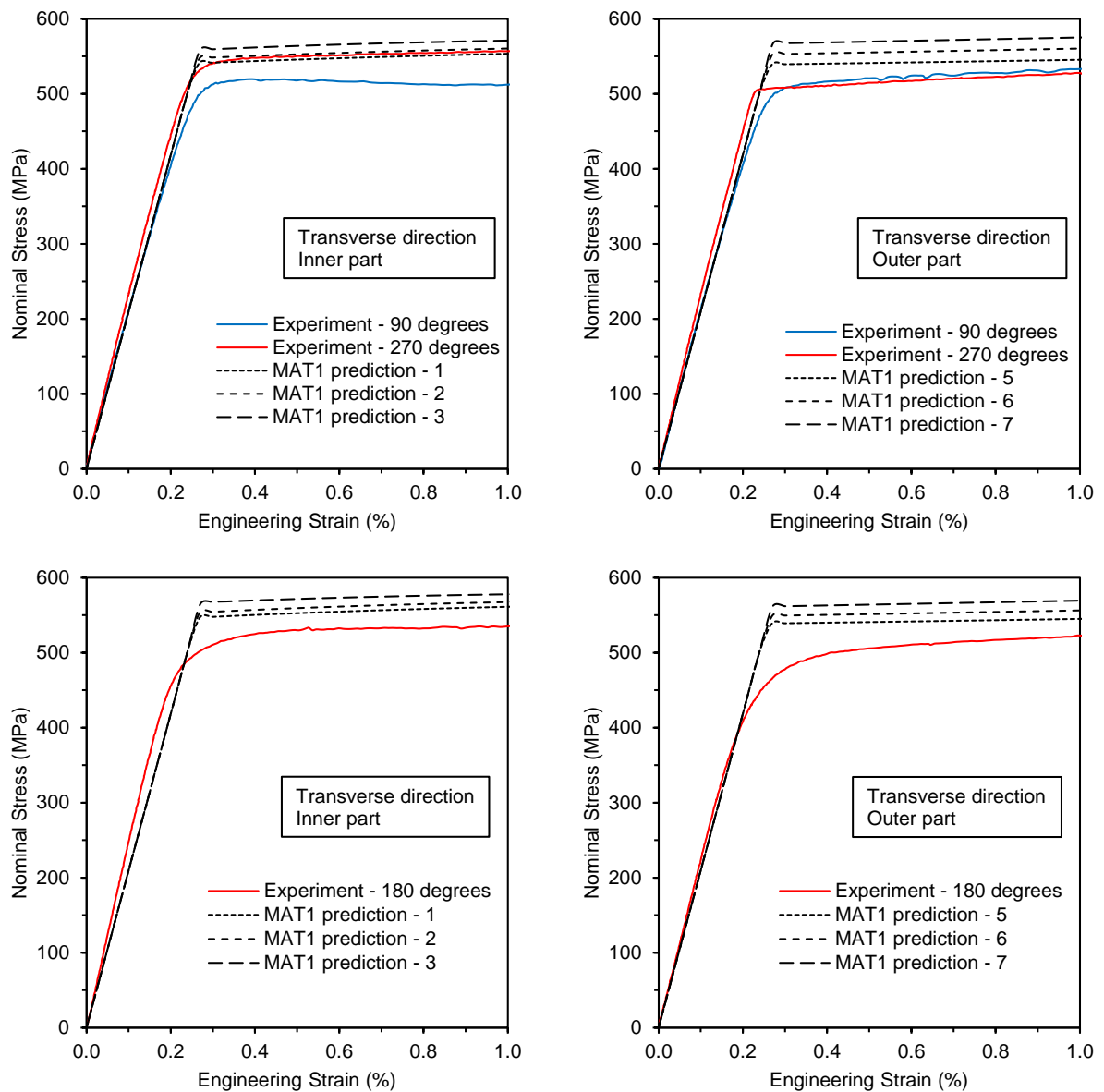


Figure 3.19: Measured and predicted tensile stress-strain response in the transverse direction of the pipe.

Table 3.3: Yield strength  $R_{t0.5}$  in the transverse direction of the JCO-E pipe

| JCO-E pipe          | yield strength $R_{t0.5}$ (MPa) in transverse (T) direction |             |            |             |
|---------------------|---|-------------|------------|-------------|
|                     | compression   |             | tension    |             |
|                     | inner (IN)  | outer (OUT) | inner (IN) | outer (OUT) |
| 90-degree position  | 490   | 421         | 518        | 521         |
| 180-degree position | 495   | 434         | 530        | 506         |
| 270-degree position | 475   | 422         | 550        | 515         |
| mean value          | 487   | 426         | 533        | 514         |

Stress-strain curves at the inner part of JCO-E pipe wall, obtained from MAT2 material parameters at 90-degree position, are depicted in Figure 3.20. Based on the calculated value of the yield strength  $R_{t0.5}$ , the corresponding stress-strain curve obtained using the MAT1 material properties provides superior prediction of the experimental curve. Following, all numerical predictions are obtained using MAT1 material parameters exclusively.

During the expansion stage, the movement of the expander segments is mainly associated with transverse (hoop) tensile loading of the JCO pipe. In Figure 3.21, transverse tensile stress-strain responses as predicted from the finite element model at the 90-degree position are compared with the corresponding predicted responses of the pipe subjected to zero expansion (JCO pipe). Similar calculations are also conducted to obtain compressive stress-strain responses of the JCO and JCO-E pipe material, which are shown in Figure 3.22. The results show that the application of expansion increases the tensile strength and degrades the compressive strength in the transverse direction of pipe, an observation consistent with the one reported in [11].

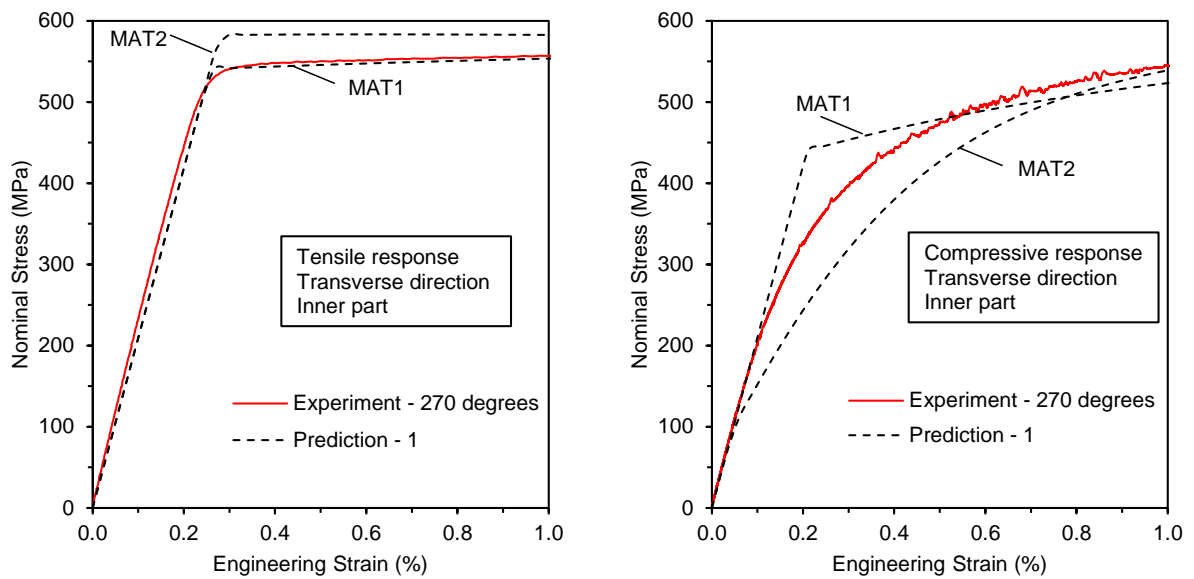


Figure 3.20: Stress-strain response of the pipe; predictions obtained from the MAT2 material properties compared with experimental results.

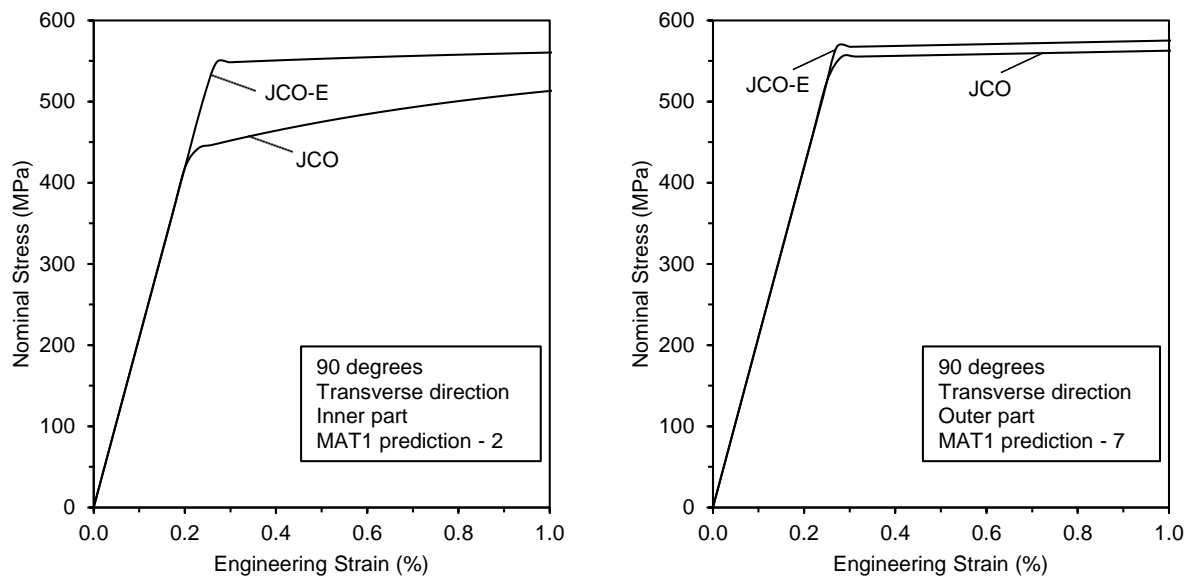


Figure 3.21: Predicted tensile stress-strain response of the JCO pipe (non-expanded) and the JCO-E pipe.

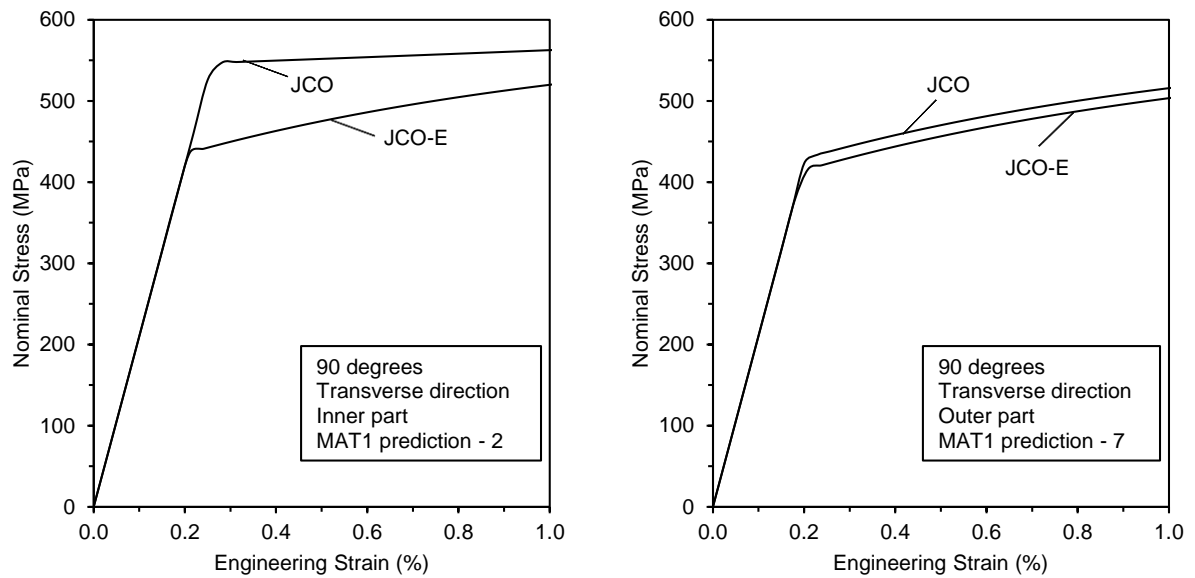


Figure 3.22: Predicted compressive stress-strain response of the JCO pipe and the JCO-E pipe.

### 3.1.4 Effect of expansion on pipe thickness and residual stresses

Employing the approach used in a previous work [18], the following measure of pipe expansion is adopted, considering the so-called “expansion strain” and it is denoted as  $\epsilon_E$  :



$$\varepsilon_E = \frac{C_E - C_W}{C_W} \quad (3.1)$$

In the above expression,  $C_E$  and  $C_W$  are the mid-surface lengths of the pipe circumference after the expansion phase (and removal of the expander segments) and after unloading from the welding stage, respectively. A similar definition for the circumferential expansion strain has also been adopted by Herynk *et al.* [11] and by Chatzopoulou *et al.* [6]. Since the value of  $C_E$  is measured after the removal of the expander segments, the expansion strain value  $\varepsilon_E$  can be considered as a “permanent” expansion strain, where the small “elastic rebound” at the end of the expansion is also taken into account. It is important to underline though that the expansion strain  $\varepsilon_E$  is quite different than the local circumferential strain at a specific location of the pipe. In other words, the value of expansion strain  $\varepsilon_E$  should be regarded as a “macroscopic” or “global” expansion strain and constitutes a useful parameter in order to quantify the expansion size.

During the JCO-E manufacturing process, the plate is subjected mainly to circumferential bending and expansion and, as a result, the thickness of pipe at the end of JCO-E process is different than the initial plate thickness. A parametric study is conducted to examine the effect of expansion on pipe thickness. Both average thickness and expansion strain refer to the stage after unloading from the expansion phase. The average thickness  $t_{\text{average}}$  of the pipe, obtained from the predicted measurements at 90-degree, 180-degree and 270-degree position, is presented in Figure 3.23 with respect to the value of the permanent expansion strain  $\varepsilon_E$ . The numerical results show that the average thickness  $t_{\text{average}}$  decreases with increasing values of expansion strain  $\varepsilon_E$  in a quasi linear manner. For zero expansion (JCO pipe), the average thickness is equal to 19.38mm, a value very close to the steel plate thickness. This negligible reduction is mainly attributed to the JCO forming process, which is mainly associated with bending deformation. As the expansion level increases, the wall thickness of the pipe is reduced mainly due to circumferential expansion obtained from the net tension induced in the pipe wall. For expansion strain  $\varepsilon_E = 2.09\%$ , the average thickness is equal to 19.20mm, a 1.23% reduction with respect to the initial plate thickness (19.44mm).

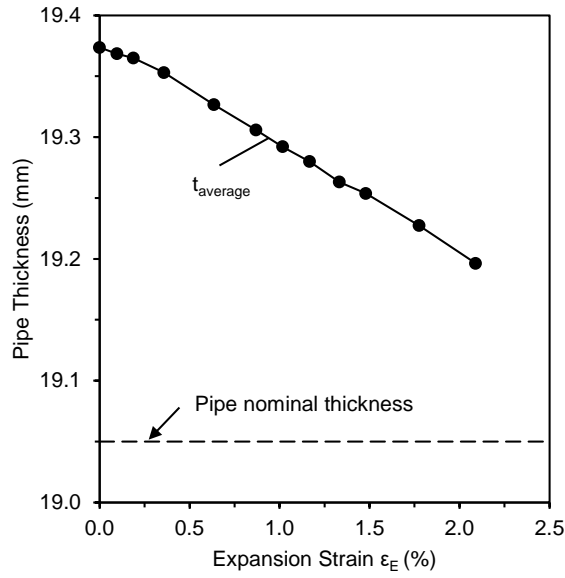


Figure 3.23: Average pipe thickness  $t_{\text{average}}$  in terms of expansion strain.

For four values of expansion strain, the (residual) circumferential stresses of JCO-E pipe at the 180-degree and 90-degree position are presented in Figure 3.24 and Figure 3.25, respectively, where  $\sigma_{c,\text{max}}$  denotes the maximum value of the circumferential stress and  $\sigma_y$  is equal to 523MPa, corresponding to the mean value of the yield strength  $R_{t0.5}$  measured in the tensile tests on coupon specimens, extracted from the transverse direction of JCO-E pipe. For expansion strain  $\epsilon_E = 0.36\%$ , the maximum residual circumferential stress at 90-degree position of the pipe is 111.67MPa, which is 21% of yield stress  $\sigma_y$ . Using the MAT2 material properties, the corresponding maximum residual circumferential stress is 115.02MPa (22% of yield stress  $\sigma_y$ ). The numerical results in Figure 3.24 and Figure 3.25 clearly demonstrate that the increase of expansion reduces the residual stresses, which has also shown in Figure 3.14, and for the JCO-E pipe under consideration, this reduction is observed up to expansion strain value of  $\epsilon_E = 1.02\%$ .

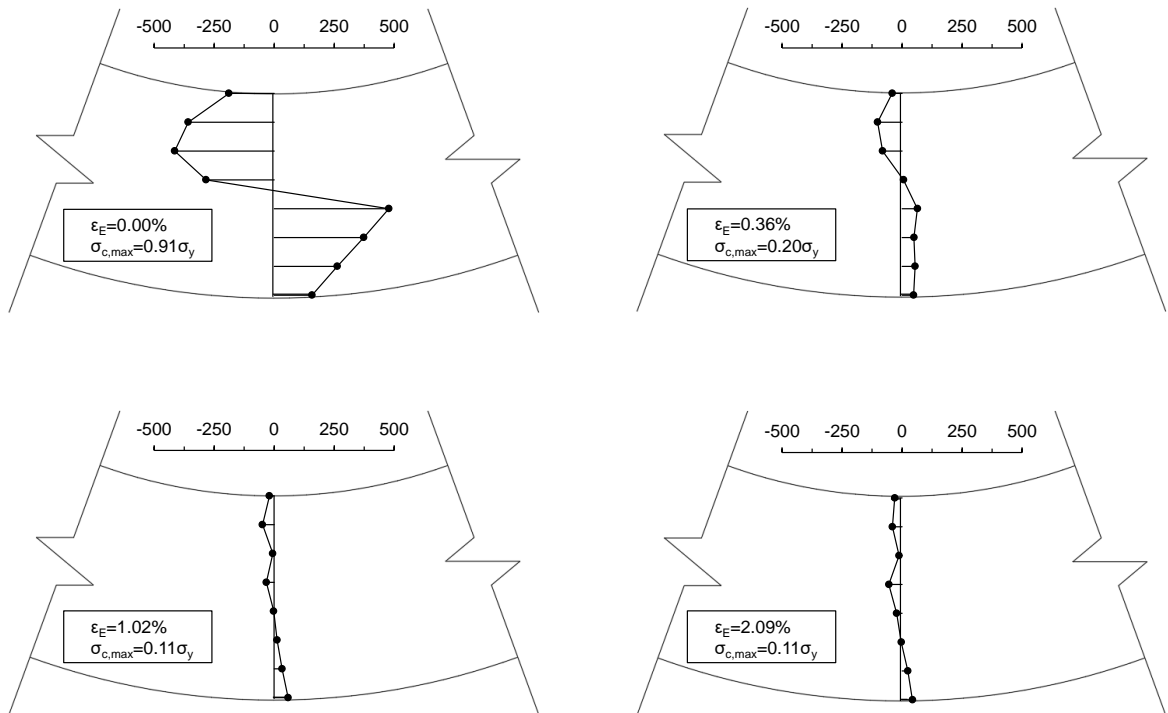


Figure 3.24: Calculated circumferential residual stress distribution of the JCO-E pipe at 180-degree position, for different values of expansion strain; the first picture (top-left) refers to the stage after welding, where no expansion is applied (JCO pipe).

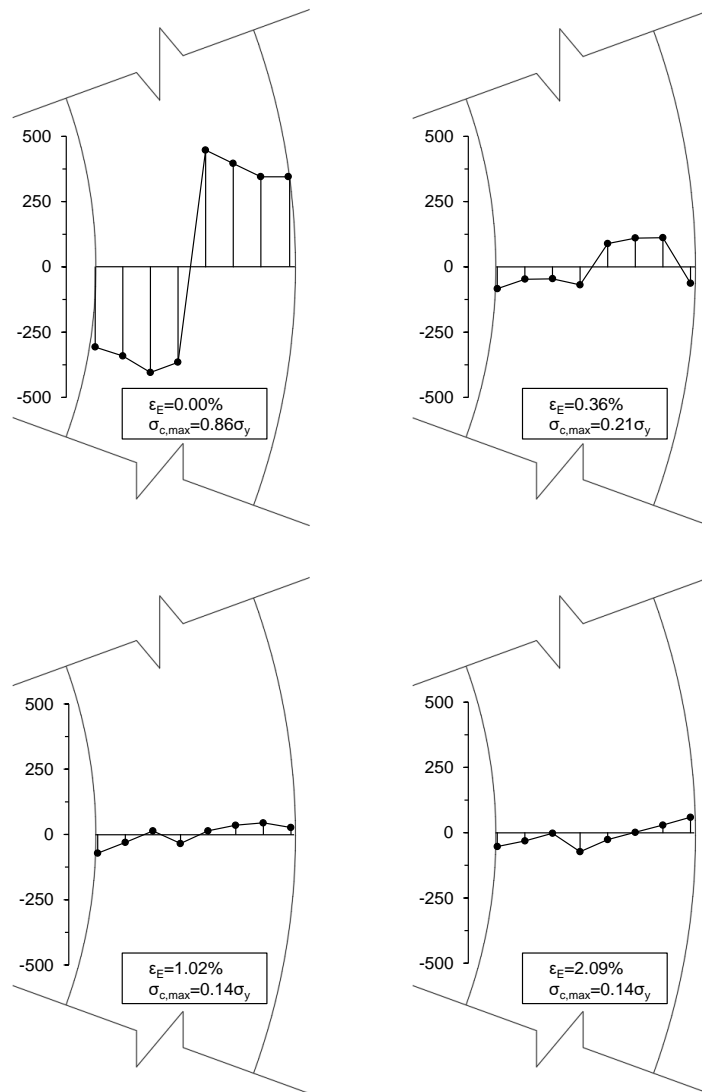


Figure 3.25: Calculated circumferential residual stress distribution of the JCO-E pipe at 90-degree position, for four expansion levels.

### 3.1.5 Effect of expansion and welding process on pipe ovality and collapse pressure

Apart from the simulation of JCO-E manufacturing process and the prediction of line pipe properties, the present model is capable of predicting the influence of manufacturing process on structural performance. Using the same two-dimensional model, the analysis continues beyond manufacturing and uniform external pressure is applied on the JCO-E pipe to calculate its collapse pressure and post-buckling response.

An important geometric feature with immense influence on the external pressure response of the pipe refers to the ovalization of pipe cross-section. At any stage of pipe deformation, a quantification of pipe cross-sectional ovalization  $\Delta$  is defined using the following formula:

$$\Delta = \frac{D_{\max} - D_{\min}}{D_{\max} + D_{\min}} \quad (3.2)$$

where  $D_{\max}$  and  $D_{\min}$  are the maximum and minimum outer diameters of the pipe cross-section, respectively, excluding the height of weld bead. Upon completion of JCO-E manufacturing process and before external pressure is applied, the corresponding value of ovalization parameter in equation (3.2) is referred to as “initial ovalization”; it is denoted as  $\Delta_0$  and expresses the residual ovalization of the pipe cross-section. Sometimes, it is also referred to as “cross-sectional ovality” or simply “pipe ovality”. This initial ovalization constitutes a geometric imperfection of the line pipe, which affects significantly its ultimate external pressure capacity [2].

A numerical study is performed to examine the effects of expansion level (i.e. the value of expansion strain  $\varepsilon_E$ ) on the initial ovalization parameter  $\Delta_0$  and the corresponding ultimate external pressure capacity of the pipe. Figure 3.26 presents the predicted collapse pressure, denoted as  $P_{CO}$ , and the corresponding initial ovalization parameter  $\Delta_0$  in terms of the applied (permanent) expansion strain  $\varepsilon_E$ . It is worth noting that pressurizing the JCO-E pipe under plane strain conditions, instead of generalized plane strain conditions, there is an insignificant increase in the values of collapse pressures shown in Figure 3.26; it is smaller than 0.13%. The above comparison is interpreted to show that the collapse of this JCO-E pipe ( $D/t > 34$ ) is not affected by the restriction of its axial strain, during the application of external pressure loading. For a small value of expansion strain ( $\varepsilon_E = 0.10\%$ ), the corresponding initial ovalization is  $\Delta_0 = 0.16\%$ , and the corresponding collapse pressure  $P_{CO}$  is equal to 11.31MPa. With increasing expansion, the value of initial ovalization  $\Delta_0$  drops sharply, causing a significant increase of  $P_{CO}$ . More specifically, the value of  $\Delta_0$  decreases quite rapidly with increasing  $\varepsilon_E$ , until a value of  $\varepsilon_E$  equal to 0.64%. Upon additional outward movement of the expander segments, the value of the initial ovalization  $\Delta_0$  remains

unaffected. Furthermore, the initial ovalization at expansion strain  $\varepsilon_E = 1.02\%$  is equal to 0.03%, and the corresponding collapse pressure  $P_{CO}$  (12.38MPa) is highest with respect to the expansion strain  $\varepsilon_E$ ; as a consequence, the value of  $\varepsilon_E = 1.02\%$  can be considered as the optimum expansion for this specific line pipe. The observation that a maximum collapse pressure exists, corresponding to an optimum expansion level, is in accordance with the results reported in [1], [18]. On the other hand, increasing the expansion strain beyond the value of  $\varepsilon_E = 1.02\%$ , the corresponding collapse pressure decreases, despite the fact that a minimum has been reached both for the value of the maximum circumferential residual stress (e.g. Figure 3.24) and the pipe (initial) ovality (Figure 3.26). In this case, the reduction of the JCO-E pipe external pressure capacity is attributed to the degradation of the compressive mechanical properties, because of the Bauschinger effect. It is worth mentioning that using the MAT2 material properties, similar calculations resulted in a maximum value of  $P_{CO}$  19.88% lower than the 12.38MPa value calculated with the MAT1 material properties, where the corresponding optimum expansion  $\varepsilon_E$  is equal to 0.19%. The significantly low value of collapse pressure predicted by the MAT2 material properties is attributed to the early compressive yielding of this material model under reverse plastic loading (Figure 3.8). Application of external pressure results in a progressive increase of initial ovalization  $\Delta_0$  to a current value  $\Delta$ , and the resulting pressure-ovalization ( $P-\Delta$ ) responses for three cases of the applied expansion are depicted in Figure 3.27. The corresponding deformed shapes of the JCO-E pipe for expansion strain  $\varepsilon_E = 1.02\%$ , at maximum pressure and at post-buckling, are shown in Figure 3.28.

In an attempt to interpret the influence of the JCO-E fabrication process on the collapse pressure of the final product, a “fictitious” pipe subjected to uniform external pressure, under generalized plane strain conditions, is considered. This fictitious pipe refers to a two-dimensional pipe model, which has zero residual stresses-strains before the application of external pressure, so that the loading history during its fabrication process is neglected. Furthermore, the elastic-plastic material behavior is assumed to be described by the MAT1 set of material parameters (description of the plate material). The cross-section of the fictitious pipe is an ellipse, the initial ovalization of which corresponds to the minimum initial ovalization of the JCO-E pipe ( $\Delta_0 = 0.03\%$ ). The thickness of this pipe is equal to the plate

thickness, i.e.  $t=19.44\text{mm}$ , and the outer diameter equals to the nominal outer diameter of JCO-E pipe (26 inches). Finally, applying uniform external pressure, the predicted collapse pressure of the fictitious pipe is  $12.72\text{MPa}$ , while the collapse pressure of JCO-E pipe for the optimum expansion ( $\varepsilon_E = 1.02\%$ ) is  $12.38\text{MPa}$ ; the difference is  $2.75\%$ . Therefore, the effect of fabrication process may not be essential for the collapse pressure of this JCO-E pipe, when the level of expansion is close to the optimum value  $\varepsilon_E = 1.02\%$ .

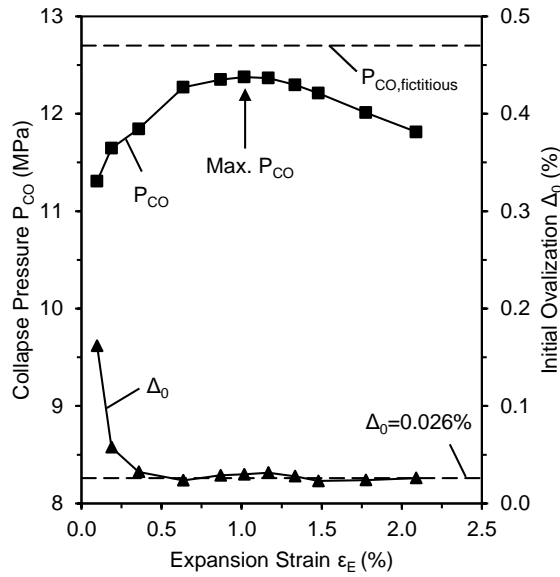


Figure 3.26: Effect of expansion on collapse pressure  $P_{CO}$  and the corresponding initial ovalization  $\Delta_0$ .

The maximum collapse pressure of JCO-E pipe computed numerically is compared with the corresponding predictions of the DNVGL-ST-F101 [7] and API 1111 [8] standards. The DNVGL-ST-F101 formula considered in the present calculation adopts an ovality parameter equal to  $0.5\%$  and fabrication factor  $\alpha_{fab} = 0.85$ . This value of  $\alpha_{fab}$  refers to UOE pipes, and it is used herein because of the absence of relevant value for JCO-E pipes. The material and geometric parameters considered in the corresponding equations and the predictions from the two standards are shown in Table 3.4. In those calculations, safety factors/margins suggested by the standards are not taken into account, in order to conduct a fair comparison with the finite element results. The collapse pressure predictions from [7] and [8] are approximately  $16\%$  lower with respect to the maximum collapse pressure obtained from the numerical analysis results, which is a very satisfactory result.

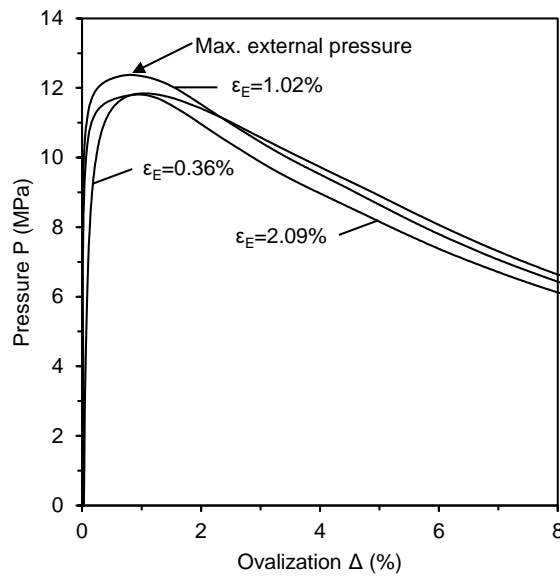


Figure 3.27: Predicted response of the pipe under external pressure with respect to cross-sectional ovalization.

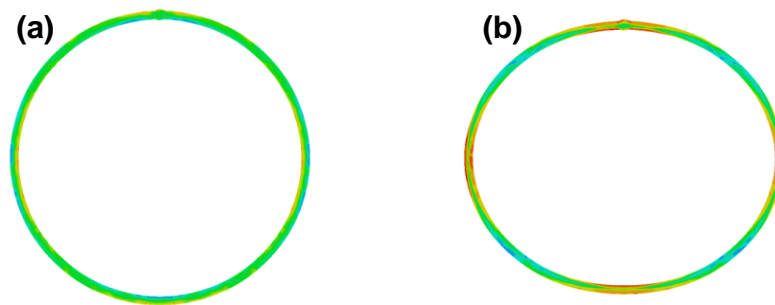


Figure 3.28: Deformed cross-sectional shape of the JCO-E pipe subjected to external pressure for the case of  $\varepsilon_E = 1.02\%$  ; (a) configuration at maximum external pressure corresponding to ovalization  $\Delta = 0.80\%$  ; (b) post-buckling configuration corresponding to ovalization  $\Delta = 8.00\%$  .

Finally, the effect of welding process on the external pressure resistance of JCO-E pipe is also examined. A similar analysis of the JCO-E manufacturing process is performed using only the forming data provided by the pipe mill, so that the thermo-mechanical simulation of the welding process is excluded (Section 2.4). This analysis is referred to as “mechanical analysis” and involves a purely “mechanical” connection between the two edges of the pipe after the O-phase, using appropriate kinematic conditions. Performing this



mechanical analysis,  $P_{CO}$  is greater by only 0.14MPa than the corresponding collapse pressure value obtained by the full thermo-mechanical model (1.17% difference). This is a clear indication that, although the cold forming stages of JCO-E process are essential for the collapse strength of the JCO-E pipe, the residual stresses induced by the welding process have a negligible effect on collapse pressure, since they are limited to a small part of the pipe cross-section.

Table 3.4: Pipe collapse pressure according to design equations

| JCO-E pipe parameters  | collapse pressure equation |          |
|--|----------------------------|----------|
|  | DNVGL-ST-F101              | API 1111 |
| <ul style="list-style-type: none"> <li>• <math>E=210\text{GPa}</math>, <math>\nu=0.3</math></li> <li>• for DNVGL-ST-F101 calculations: <math>\alpha_{fab} = 0.85</math>, <math>O_0 = 0.5\%</math></li> <li>• yield strength <math>R_{t0.5}</math>: 520MPa (value measured in the tensile experiments of coupons obtained from the transverse direction of the plate)</li> <li>• pipe wall thickness: 19.19mm (mean value measured in the pipe mill)</li> <li>• measured outer diameter of the pipe: 661.7mm</li> </ul> | 10.33MPa                   | 10.55MPa |

### 3.1.6 Effect of anisotropy on external pressure capacity

Considering the “mechanical analysis” described above, a short parametric study of the effect of anisotropy on the collapse pressure is conducted. The anisotropic parameters adopted correspond to three cases of steel plate material description. For each case, the corresponding initial ovalization  $\Delta_0$  and the normalized value of collapse pressure  $P_{CO} / P_y$  are listed in Table 3.5 and refer to the JCO-E pipe with expansion strain  $\varepsilon_E = 1.02\%$  (optimum expansion).

Table 3.5: Effect of anisotropy on collapse pressure

| <b>steel plate</b> ( $\sigma_{0,x} = 520$ MPa) | <b>JCO-E pipe</b> |                                    |
|--|-------------------|------------------------------------|
| anisotropy constants                           | $P_{CO} / P_y$    | initial ovalization $\Delta_0$ (%) |
| $S_y = S_z = 0.94$                             | 0.415             | 0.030                              |
| $S_y = 1.00, S_z = 0.94$                       | 0.416             | 0.027                              |
| $S_y = S_z = 1.00$                             | 0.417             | 0.031                              |

The first case is included for comparison purposes and corresponds to the anisotropy constants calibrated using the coupon tests of the plate, adopted and used throughout the present work, assuming that the yield stress in the thickness direction is equal to the yield stress in the longitudinal direction. Considering the same JCO-E process, the additional two cases show that anisotropy of the steel plate, within the range indicated by the material tests, have a slight influence on the value of collapse pressure. In addition, the corresponding value of initial ovalization at the end of the fabrication process may not be significantly affected. This may imply that the JCO-E forming process of the line pipe under consideration could have been modeled with reasonable accuracy using the cyclic plasticity model with isotropic (von Mises) yield criterion, employed in a previous publication [18].

### 3.2 Thick-walled JCO-E pipe

Taking into account the methodology presented in detail in Chapter 2, a generalized plane-strain finite element model is developed to simulate the cold forming of a 39mm thick plate through the JCO-E process, based on the forming parameters provided by pipe mill. The plate width equals to 2242mm. The JCO-E pipe product is a 30-inch-diameter X60 line pipe, its D/t ratio is 19.69 (thick-walled pipe) and is designed for deep-water offshore applications. The steel plate is discretized using twelve elements across the thickness direction. The size of an element in the transverse direction is selected to be 16% of plate thickness. The modelling of welding (SAW) process is excluded from the present analysis. This decision is based on the findings of the last part of Section 3.1.5, and the argument proposed in [16]. More specifically, it was found that the residual stresses due to welding have small influence on the collapse pressure of a JCO-E pipe. In the following paragraphs, numerical results on this JCO-E pipe are obtained, supported by experimental results that refer to the plate material

properties. The numerical results focus on (a) the geometry, (b) the material properties of JCO-E pipe and (c) the collapse performance of JCO-E pipe.

### 3.2.1 Material model calibration

Similar to Section 3.1.1, monotonic and cyclic tests have been performed on steel specimens extracted from the steel plate (raw) material, in transverse and longitudinal direction. In particular, the specimens have been extracted from three plates (plate-16, plate-17, plate-21), and refer to: (a) full-thickness strips subjected to tension or compression, and (b) parts of the plate wall, which are subjected to cyclic loading. Stress-strain curves obtained from the experiments and the material calibration (model) are depicted in Figure 3.29. The Young's modulus is considered equal to 200GPa, the Poisson's ratio is 0.30, while the parameters associated with the plastic behavior of plate material are shown in Table 3.6.

Table 3.6: Material model parameters

|       | $\sigma_{0,x}$<br>(MPa) | $S_y$ | $S_z$ | Q<br>(MPa) | b   | $\gamma$ | $C_0$<br>(MPa) | $Q_b$<br>(MPa) | $c_b$ |
|-------|-------------------------|-------|-------|------------|-----|----------|----------------|----------------|-------|
| model | 440                     | 1.00  | 1.00  | -15        | 558 | 250      | 21,303         | -3,759         | 100   |

### 3.2.2 Modelling of pipe forming process

Representative contour plots during the crimping stage and the JCO forming process are shown in Figure 3.30; fifteen punching steps are applied during JCO process. In the pipe mill, after JCO punch removal, the gap is too large for welding the edges. To this effect, a secondary forming press, referred to as finishing press, is used to reduce the gap to a minimum by means of two bending steps. These two targeted bending steps are taken into account in the finite element model and depicted in Figure 3.31. The gap remained between the edges, both after the simulation of JCO forming process (gap 1), and after the simulation of “finishing” process (gap 2), is in accordance with the data provided by pipe mill. The analysis proceeds in the gap-closing, where the edges come together by applying appropriate mechanical loading to their surfaces. Subsequently, the modelling of expansion process is performed, as shown in Figure 3.32; the expansion process accounts for twelve expander segments. At three positions around the circumference, values of the inner diameter of JCO

and JCO-E pipe are shown in Table 3.7 and compared with corresponding ones provided by pipe mill.

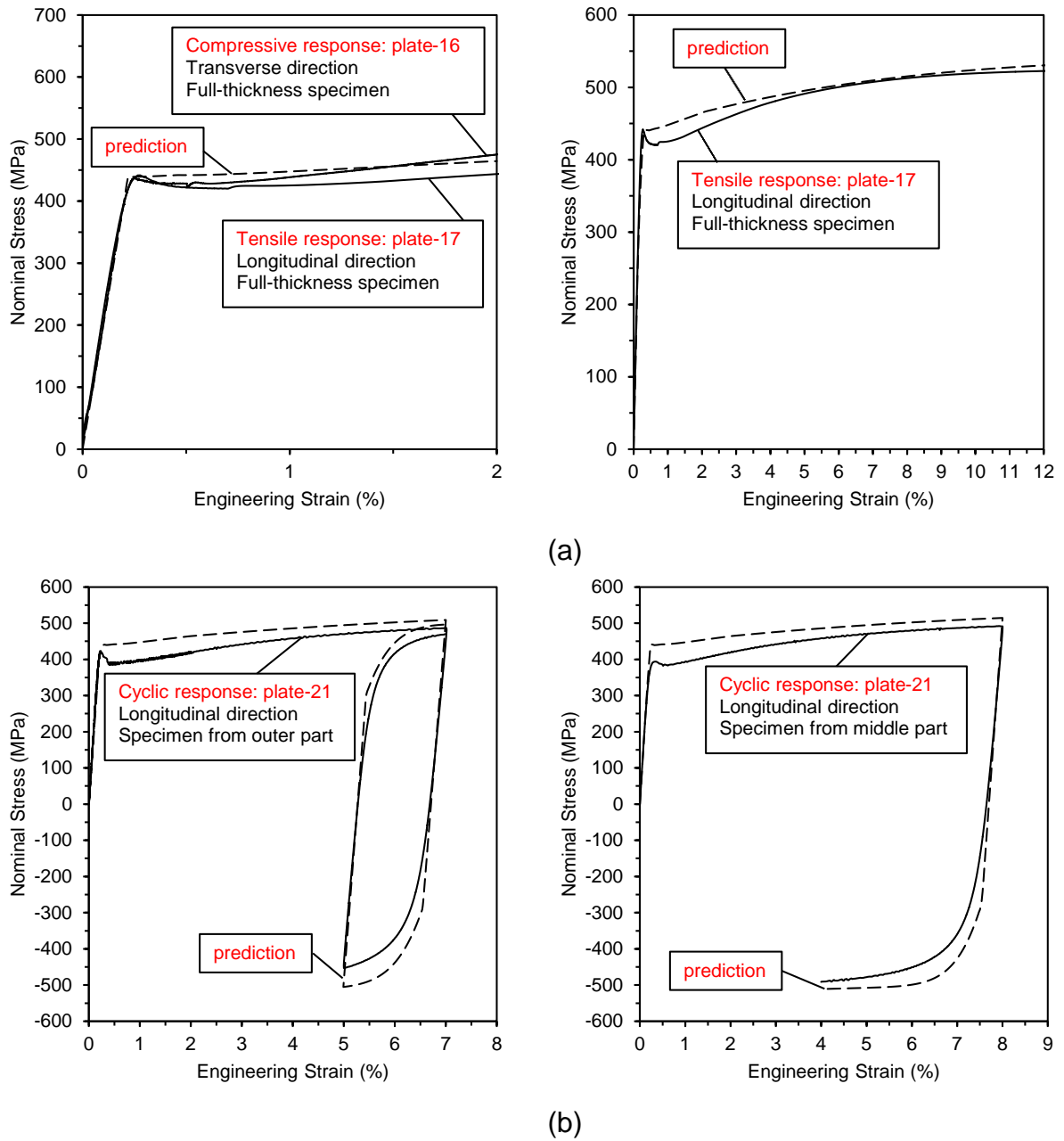


Figure 3.29: Steel plate material; (a) monotonic and (b) cyclic stress-strain response.

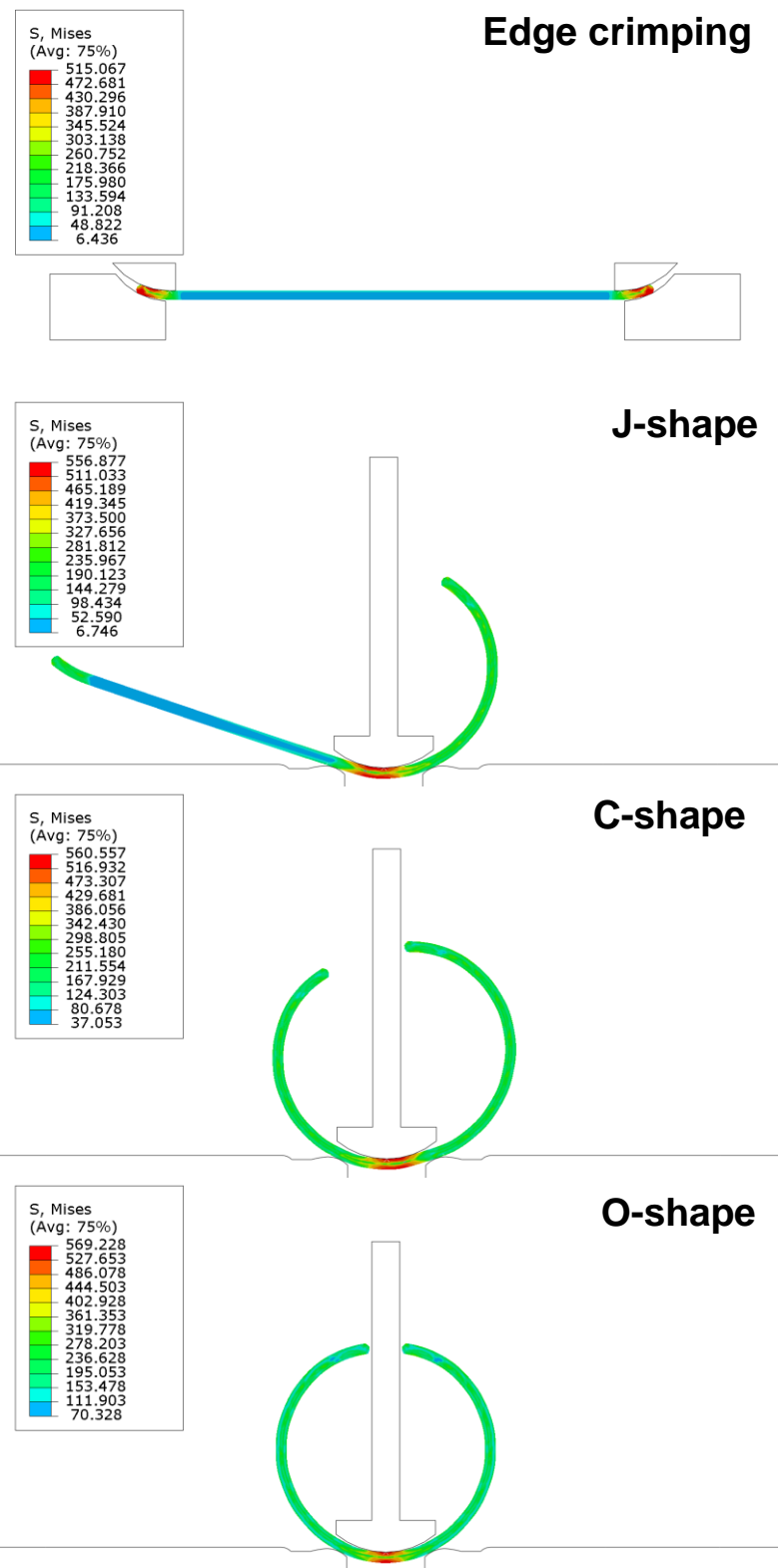


Figure 3.30: Plate configuration during the crimping and the JCO forming process.

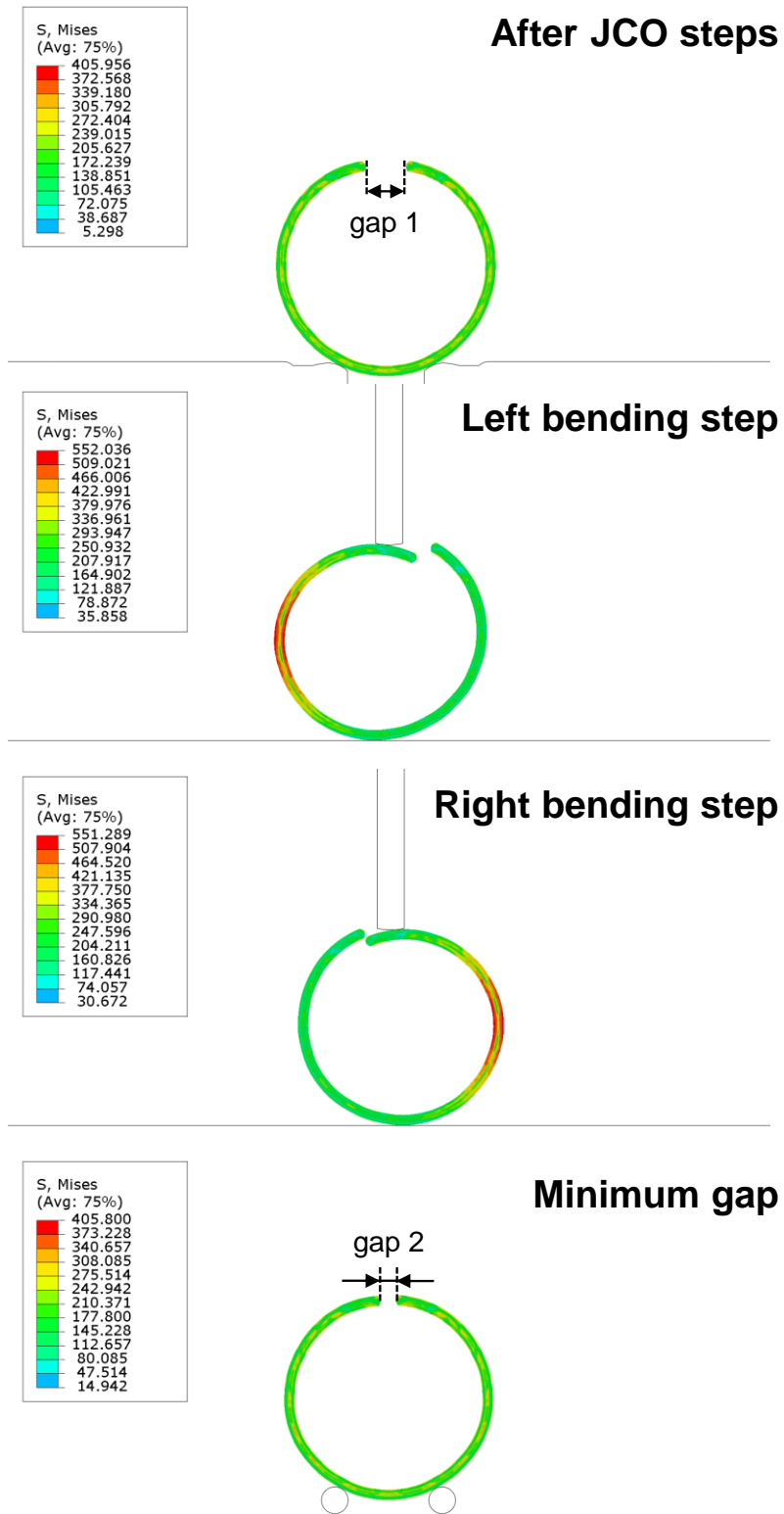


Figure 3.31: Gap-closing process with finishing press.

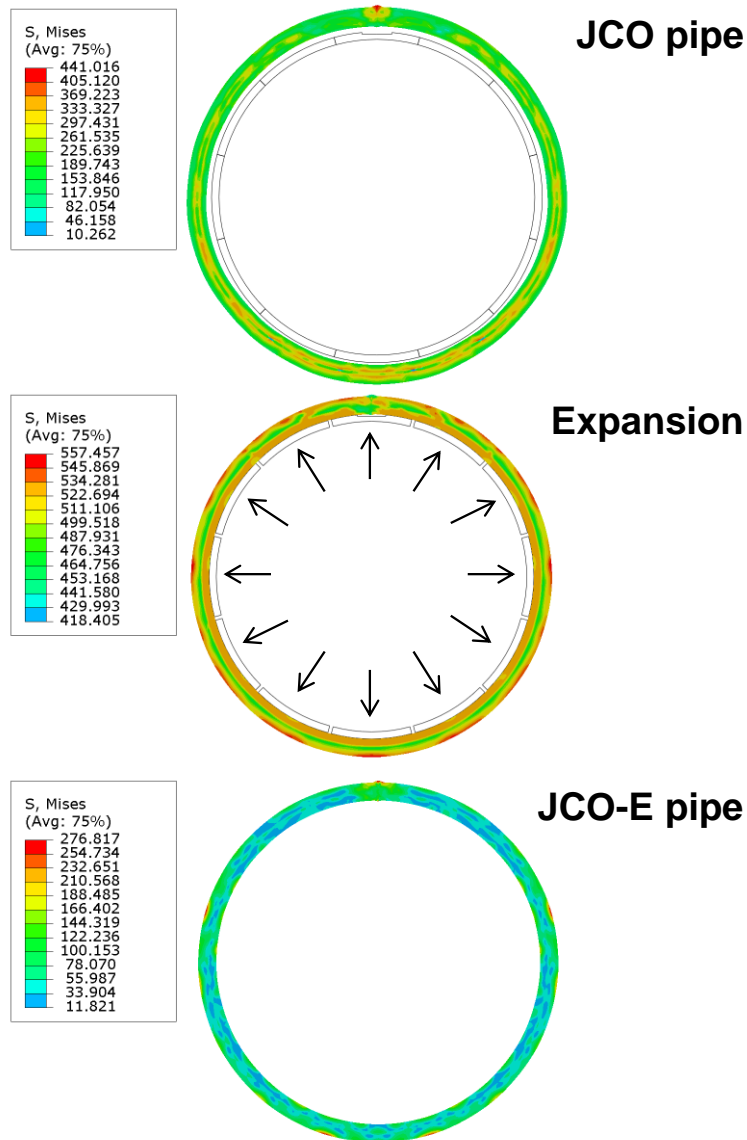


Figure 3.32: Expansion of the JCO pipe.

Table 3.7: Pipe inner diameter

| inner diameter | pipe mill measurements (mm) | FEM (mm) |
|----------------|-----------------------------|----------|
| JCO pipe       | 0-degree position           | 675-677  |
|                | 45-degree position          | 678-681  |
|                | 90-degree position          | 683-689  |
| JCO-E pipe     | 0-degree position           | 684-686  |
|                | 45-degree position          | 686-687  |
|                | 90-degree position          | 686-688  |

### 3.2.3 Mechanical properties of JCO-E pipe

The mechanical behavior of JCO-E line pipe material is evaluated both experimentally and numerically, according to the methodology described in Section 2.5. The stress-strain response of the outer part in the longitudinal direction (L-OUT) is shown in Figure 3.33. In the transverse direction of pipe, compressive and tensile stress-strain responses are depicted in Figure 3.34 and Figure 3.35, respectively. The predictions are obtained from elements, whose locations correspond to the locations of specimens extracted from the JCO-E pipe.

The results show that in the longitudinal direction, the yield strength  $R_{t0.5}$  is higher compared to the one of plate material, both in the compressive and the tensile stress-strain responses. In the transverse direction, the yield strength  $R_{t0.5}$  obtained from compressive responses at the outer part of pipe wall is lower with respect to the yield strength of plate material, due to Bauschinger effect. In contrary, a significant increase of the tensile yield strength  $R_{t0.5}$  of pipe material is observed due to strain hardening. The comparison between numerical and experimental results is considered quite satisfactory and, to a certain extent, conservative regarding the tensile response of the inner part of pipe wall. The values of yield strength  $R_{t0.5}$  measured from specimens extracted from the transverse direction of JCO-E pipe are summarized in Table 3.8.

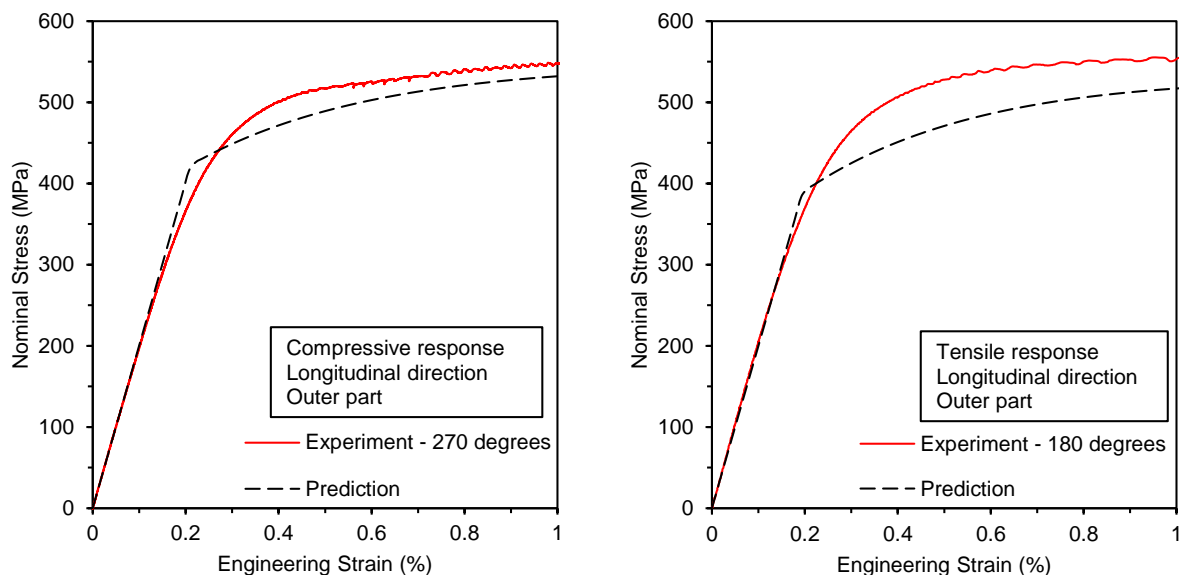


Figure 3.33: Measured and predicted stress-strain responses in the longitudinal direction of the pipe.



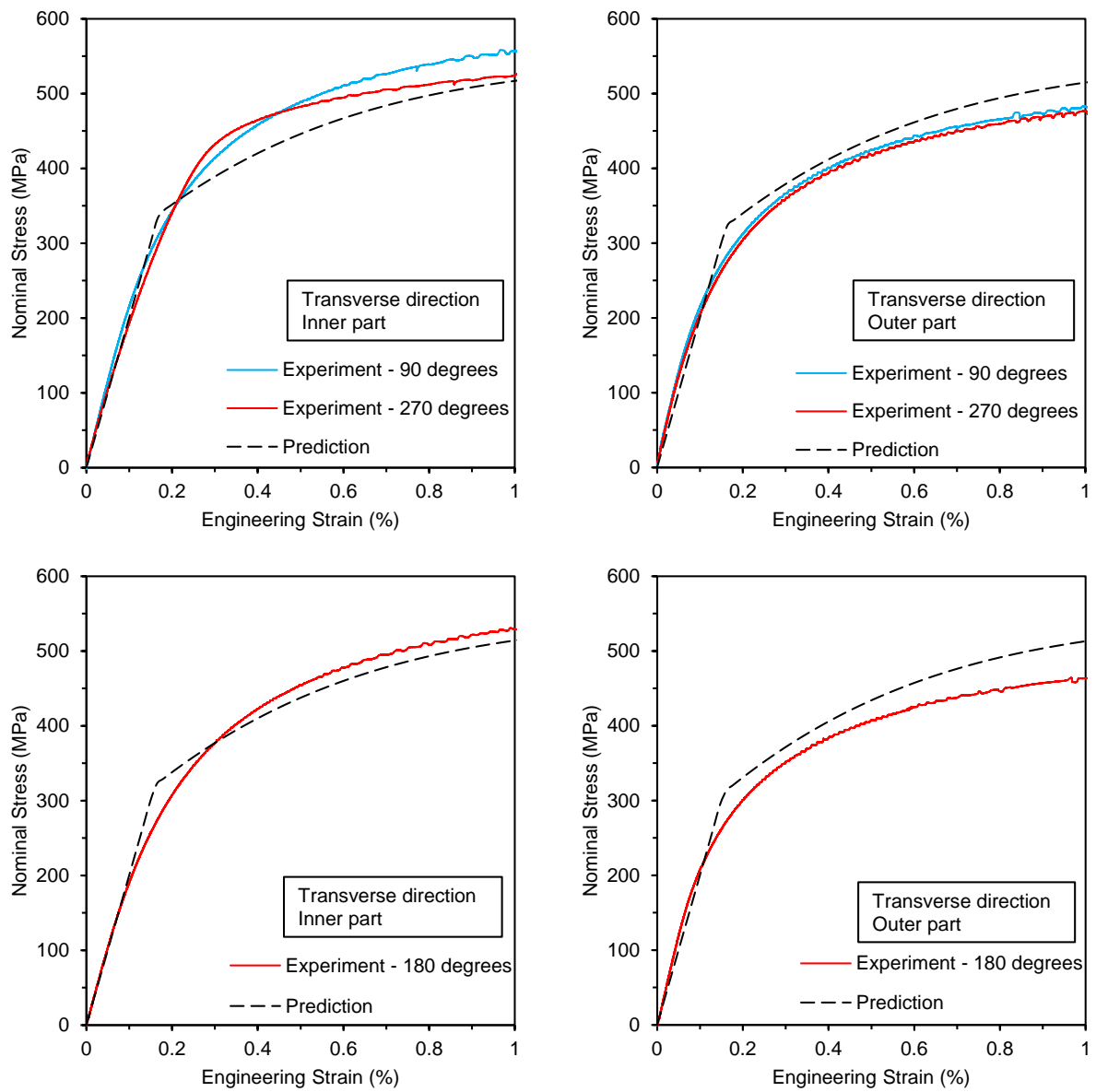


Figure 3.34: Measured and predicted compressive stress-strain response in the transverse direction of the pipe.

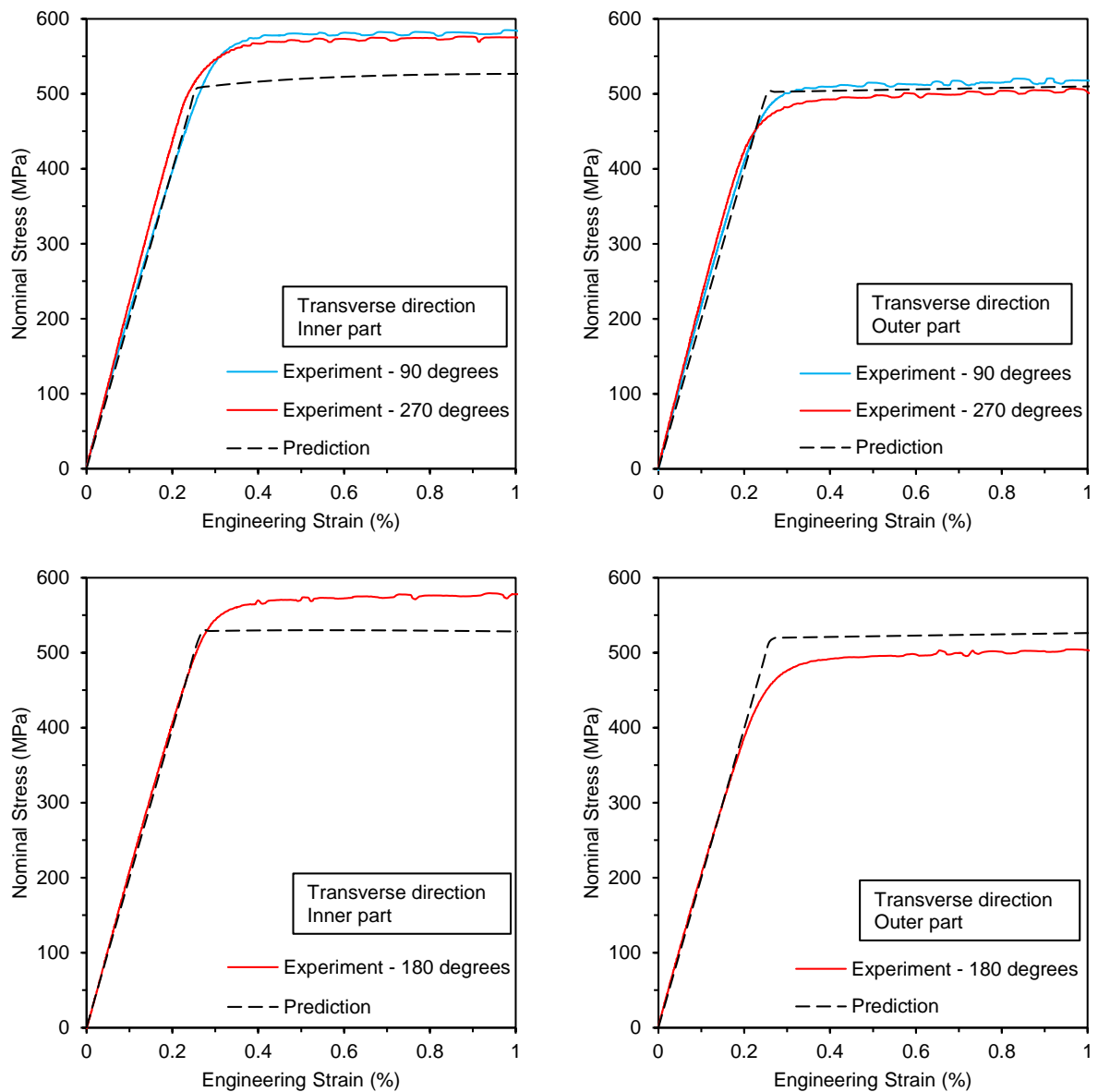


Figure 3.35: Measured and predicted tensile stress-strain response in the transverse direction of the pipe.

Table 3.8: Measured yield strength  $R_{t0.5}$  in the transverse direction of the JCO-E pipe

| JCO-E pipe          | yield strength $R_{t0.5}$ (MPa) in transverse (T) direction |             |            |             |
|---------------------|---|-------------|------------|-------------|
|                     | compression   |             | tension    |             |
|                     | inner (IN)  | outer (OUT) | inner (IN) | outer (OUT) |
| 90-degree position  | 489   | 425         | 580        | 515         |
| 180-degree position | 454   | 407         | 574        | 495         |
| 270-degree position | 482   | 418         | 570        | 497         |
| mean value          | 475   | 417         | 575        | 502         |

### 3.2.4 Effect of expansion on pipe thickness and residual stresses

The average thickness of pipe  $t_{\text{average}}$  is computed at the end of JCO-E process (including the unloading from expansion phase) and the results are shown in Figure 3.36 with respect to the expansion strain  $\epsilon_E$ . The expansion strain is defined by the following expression:

$$\epsilon_E = \frac{C_{\text{after,E}} - C_{\text{before,E}}}{C_{\text{before,E}}} \quad (3.3)$$

which is similar to equation (3.1).  $C_{\text{after,E}}$  and  $C_{\text{before,E}}$  are the mid-surface lengths of the pipe circumference after and before the expansion phase, respectively. The plot indicates that the average thickness of the formed pipe, accounting for the thickness at the 90-degree, 180-degree and 270-degree position, decreases with increasing the value of expansion strain. The average thickness of JCO pipe is equal to 38.91mm, very close to the plate thickness. Increasing the expansion level, the pipe thickness is reduced in an almost linear manner; for  $\epsilon_E = 2.22\%$ , the JCO-E pipe has an average thickness  $t_{\text{average}}$  of 38.48mm (1.33% reduction compared to the plate thickness).

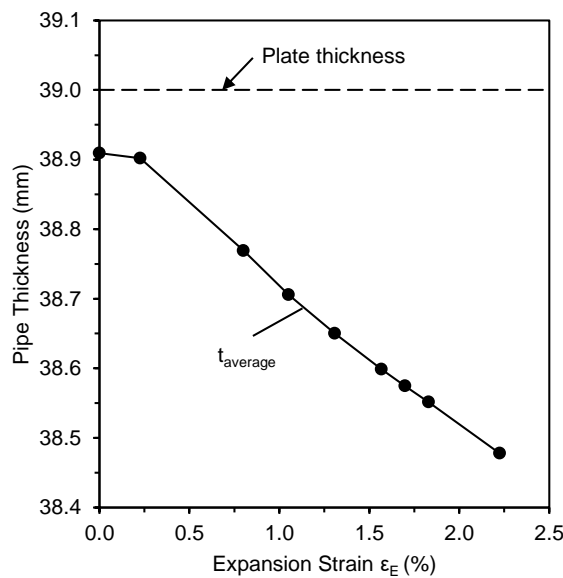


Figure 3.36: Effect of the expansion strain  $\epsilon_E$  on the average thickness  $t_{\text{average}}$  of JCO pipe.

Considering four cases of expansion strain, the residual circumferential stresses calculated at the 180-degree position of JCO-E pipe are presented in Figure 3.37. The maximum value of stress is denoted by  $\sigma_{c,max}$  and expressed in terms of  $\sigma_y$ . The value of  $\sigma_y$  is equal to 539MPa and corresponds to the mean value of yield strength  $R_{t0.5}$  measured in the tensile tests (Table 3.8). Starting from zero expansion (JCO pipe), the maximum residual circumferential stress is 84% of yield stress  $\sigma_y$ , while increasing expansion the value of maximum residual stress is decreased. For the pipe under consideration, this reduction is observed up to expansion strain  $\epsilon_E = 1.70\%$ , where  $\sigma_{c,max} = 0.18\sigma_y$ .

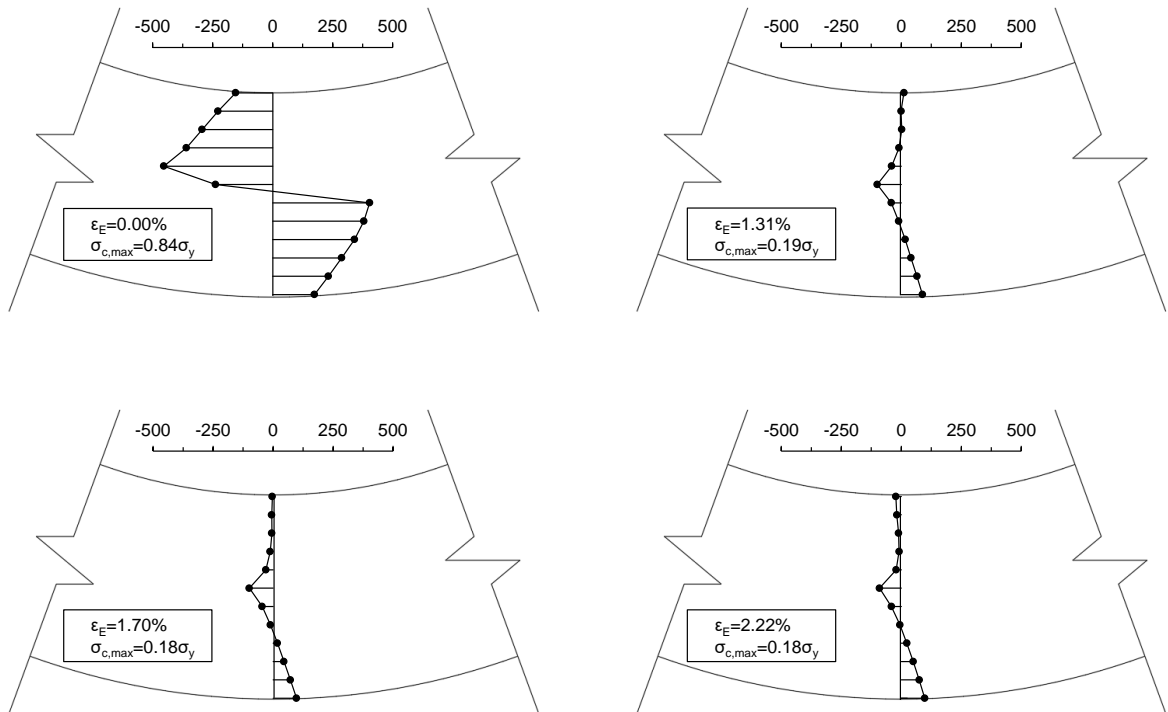

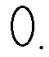


Figure 3.37 Calculated circumferential (residual) stress distribution of the JCO-E pipe at 180-degree position, for different expansion levels.

### 3.2.5 Effect of expansion on pipe ovality and collapse pressure

Following the simulation of forming process, the JCO-E pipe at the last stage of analysis procedure is subjected to external pressure under plane strain conditions. A numerical study is conducted for the effects of expansion strain  $\epsilon_E$  on the initial ovalization  $\Delta_0$  and the

ultimate external pressure capacity of line pipe; the value of initial ovalization parameter  $\Delta_0$  is obtained from equation (3.2). The predicted initial ovalization  $\Delta_0$  and the collapse pressure  $P_{CO}$  are presented in Figure 3.38 in terms of the  $\varepsilon_E$  value. Before expansion is applied ( $\varepsilon_E = 0.00\%$ ), the ovalization  $\Delta_0$  is 0.40%. Upon application of expansion, the initial ovalization drops rapidly and obtains quite small values (less than 0.05%) for  $\varepsilon_E$  greater than 1.05%.

Expanding the JCO pipe, the value of  $P_{CO}$  increases until  $\varepsilon_E$  is equal to 1.70% (optimum expansion), where  $P_{CO} = 37.72\text{MPa}$ . Further increase of expansion does not lead to smaller residual stresses (see Figure 3.37), while the value of the initial ovalization obtains an almost constant value of 0.02%. However, for  $\varepsilon_E$  greater than 1.70%, the resistance of JCO-E pipe against external pressure is decreased. This reduction of collapse pressure is attributed mainly to the degradation of compressive material properties (Bauschinger effect); for  $\varepsilon_E = 2.22\%$ ,  $P_{CO}$  is reduced by 2.96% with respect to the 37.72MPa value (maximum  $P_{CO}$ ). Furthermore, for  $\varepsilon_E$  greater than 1.70%, the failure mode switches from flattening in the direction of the horizontal plane, depicted in Figure 3.38 as , to flattening in the direction of the vertical plane, which is shown in Figure 3.38 as . This switch is attributed to the change in the circumferential location of maximum outer diameter of JCO-E pipe, which is calculated before the application of external pressure. In particular, before the external pressure is applied, the calculated maximum diameter of JCO-E pipe is located near the 90-270° direction for  $\varepsilon_E$  values smaller than 1.70%, whereas this location corresponds to the 0-180° direction for  $\varepsilon_E$  values greater than 1.70%. The above observation is directly associated with the initial ovalization (initial imperfection) of pipe, and leads to its corresponding buckle mode upon application of external pressure. Finally, for two cases of expansion level, the resulting pressure-ovalization ( $P-\Delta$ ) responses are shown in Figure 3.39, and the corresponding collapse modes are depicted in Figure 3.40 and Figure 3.41.

At this point, a “fictitious” two-dimensional pipe model is developed, similar to the one described in Section 3.1.5, to examine the effect of forming process on the ultimate external pressure capacity of JCO-E pipe. The thickness of fictitious pipe is equal to the plate thickness (39mm), the outer diameter of this pipe corresponds to the nominal value of JCO-E

pipe (30inches) and its initial ovalization  $\Delta_0$  is 0.02%, which is a value calculated at optimum expansion of JCO-E pipe. It is also assumed that the fictitious pipe is stress-free and its material behavior is identified by the plate material parameters shown in Table 3.6. Applying uniform external pressure, under plane strain conditions, the collapse pressure of fictitious pipe is 48.45MPa, while the maximum predicted collapse pressure of JCO-E pipe is 37.72MPa. Therefore, it is evident that the reliable calculation of collapse pressure requires the simulation of the entire history of deformation during the JCO-E process, using a suitable cyclic plasticity model.

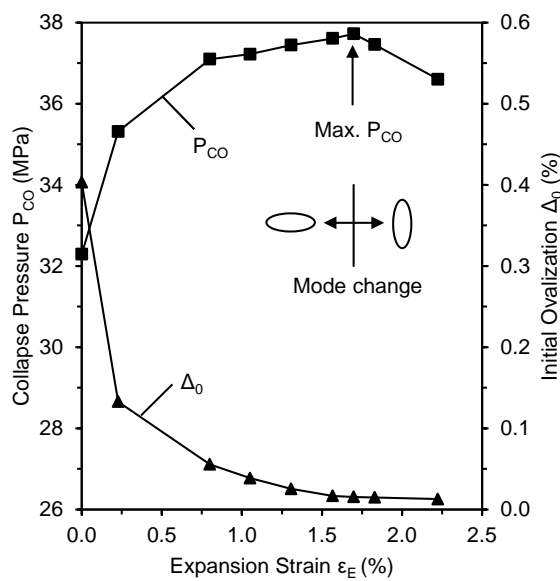


Figure 3.38: Ultimate external pressure capacity  $P_{CO}$  and the corresponding initial ovalization  $\Delta_0$  of JCO-E pipe for different values of expansion strain  $\epsilon_E$ .

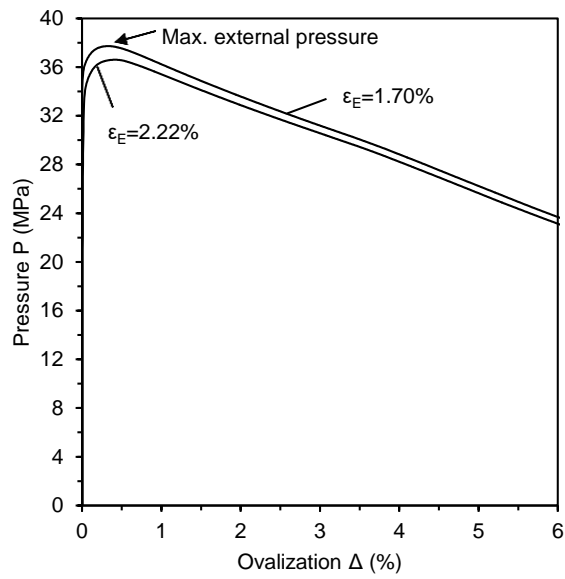


Figure 3.39: Predicted pressure-ovalization response of the pipe.

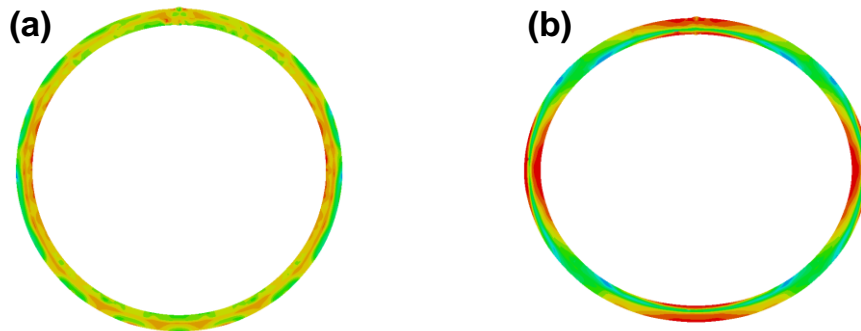


Figure 3.40: Cross-sectional shapes of the JCO-E pipe expanded with  $\epsilon_E = 1.70\%$  after the application of external pressure; (a) configuration at maximum external pressure corresponding to ovalization  $\Delta = 0.33\%$ ; (b) post-buckling configuration corresponding to ovalization  $\Delta = 6.00\%$ .

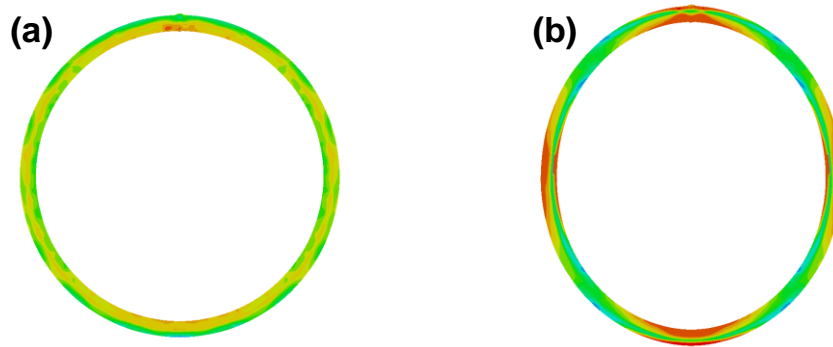


Figure 3.41: Cross-sectional shapes of the JCO-E pipe expanded with  $\varepsilon_E = 2.22\%$  after the application of external pressure; (a) configuration at maximum external pressure corresponding to ovalization  $\Delta = 0.41\%$ ; (b) post-buckling configuration corresponding to ovalization  $\Delta = 6.00\%$ .

The maximum value of the predicted  $P_{CO}$  of JCO-E pipe is compared with corresponding values calculated using the DNVGL-ST-F101 [7] and API 1111 [8] standards. The parameters adopted in these standards and the corresponding results for the collapse pressure of pipe are shown in Table 3.9; safety factors/margins proposed by the standards are not taken into account. The collapse pressure predictions, shown in Table 3.9, are approximately 9% lower compared to the maximum collapse pressure obtained from the finite element model.

Table 3.9: External pressure (collapse) design

| JCO-E pipe parameters   | collapse pressure equation |          |
|---|----------------------------|----------|
|   | DNVGL-ST-F101              | API 1111 |
| <ul style="list-style-type: none"> <li>• <math>E=200\text{GPa}</math>, <math>\nu=0.3</math></li> <li>• for DNVGL-ST-F101 calculations: <math>\alpha_{fab} = 0.85</math>, <math>O_0 = 0.5\%</math></li> <li>• yield strength <math>R_{10.5}</math>: <math>440\text{MPa}</math> (obtained from the compressive stress-strain response of plate material)</li> <li>• nominal pipe wall thickness: <math>38.7\text{mm}</math></li> <li>• nominal outer diameter of pipe: <math>762\text{mm}</math></li> </ul> | 33.74MPa                   | 35.31MPa |



### 3.2.6 Effect of JCO punching steps on pipe ovality and collapse pressure

During the JCO punching steps, the JCO press forces the plate to obtain an open-seam circular shape. The set of the values of JCO press displacement is provided by pipe mill. This set is symmetric with respect to O-step (last punching step), but it does not contain the same values for all the JCO punching steps. A parametric analysis is conducted to examine the influence of the displacement of JCO press on the ovality of JCO-E pipe and its collapse pressure. More specifically, it is assumed that the displacement of JCO press is the same during the entire JCO process, and the other (input) forming parameters correspond to those provided by the pipe mill.

Figure 3.42 shows the initial ovalization and the ultimate external pressure capacity of JCO-E pipe obtained from the analysis, assuming same punching during the JCO process, and the “as-received” analysis (Section 3.2.2). In the “same punching” analysis, both after the JCO and the finishing process, the gap between the edges obtains higher value, which leads to a JCO pipe with greater initial ovalization compared to the one calculated following the as-received analysis (see Figure 3.42a). For expansion strains  $\varepsilon_E$  greater than 0.25%, the initial ovalization calculated from both analyzes is identical. Based on the numerical results, the choice of the displacement of JCO press may not be significant for the ultimate external pressure capacity; in Figure 3.42b, the maximum values of  $P_{CO}$  are indicated with arrows. In the “same punching” analysis, the maximum predicted  $P_{CO}$  value is 0.89% lower with respect to the corresponding one obtained from the as-received analysis, and corresponds to  $\varepsilon_E = 1.33\%$ .

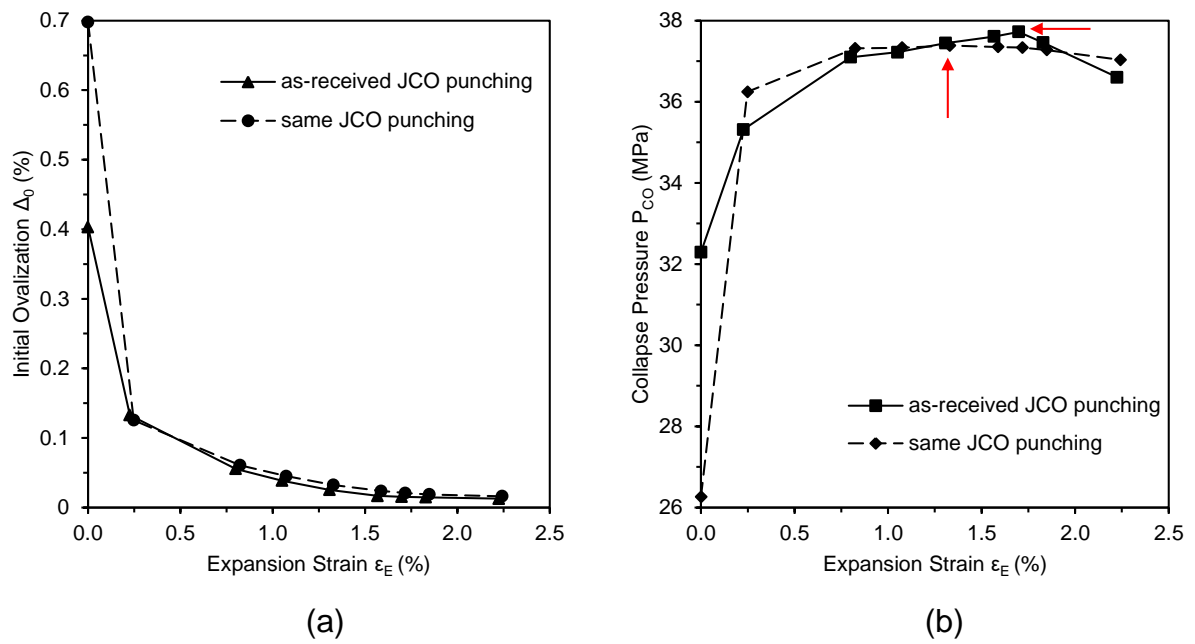


Figure 3.42: Variation of (a) initial ovalization  $\Delta_0$  and (b) collapse pressure  $P_{Co}$  in terms of expansion strain.

### 3.3 Conclusions

The finite element model is applied first to an JCO-E X65 steel pipe, with nominal diameter of 26in and nominal wall thickness 0.75in (19.05mm) and a diameter-to-thickness ratio equal to 34.67, adopting the manufacturing parameters provided by the pipe mill. Strip specimens are extracted from the raw material (steel plate) and subjected to cyclic loading, so that the stress-strain curves use to calibrate the anisotropic material model. From these curves, the ratio of the yield stress in the longitudinal to the yield stress in the transverse direction is set equal to 0.94, which implies that plate anisotropy is rather small. The prediction of collapse pressure of the JCO-E pipe is strongly affected by the choice of steel plate material model parameters related to the simulation of Bauschinger effect. In particular, two sets of material parameters have been examined (MAT1, MAT2). However, for that set which provides better comparisons with experimental data (MAT1), it is found that expansion is beneficial for the collapse pressure resistance of JCO-E pipe up to a limit value ( $\epsilon_E = 1.02\%$ ), referred to as optimum expansion. On contrary, steel plate anisotropy may not be a major factor for the value of collapse pressure, for the range of anisotropy measured in coupons,

extracted from the plate. Furthermore, the effect of welding residual stresses-strains on the collapse pressure of JCO-E pipe is rather small.

Based on the above conclusion for the effect of welding on collapse performance, the finite element model of JCO-E forming process is then applied to an X60 30-inch-diameter JCO-E pipe with nominal thickness 1.52in (38.70mm) and a diameter-to-thickness ratio equal to 19.69, using the forming parameters provided by pipe mill. Similar to the methodology described in Section 2.3, specimens are extracted from the plate and subjected to monotonic and cyclic loading tests. The plate material is considered isotropic, and the experimental stress-strain curves are used for the calibration of material model parameters. Upon simulation of forming, a numerical analysis is conducted on the effects of expansion on the overall pipe behavior against external pressure. The calculated optimum expansion  $\epsilon_E$  is 1.70%, which corresponds to the maximum collapse pressure. Furthermore, the effect of displacement of JCO press is investigated through a numerical study. Considering same displacement during the punching steps, the ultimate external pressure capacity of JCO-E pipe is slightly decreased, and it is achieved at a smaller expansion strain compared to the optimum expansion strain of JCO-E pipe formed following the pipe mill input data.

In both applications, the results show that the geometry of JCO-E pipe is quite close to the pipe mill measurements. The comparison between the material properties of pipe measured from experiments and the corresponding numerical predictions has also been quite satisfactory. Furthermore, the effects of expansion on pipe geometry, pipe material properties, residual stresses and pipe collapse strength have been investigated, and following the basic conclusions are summarized:

- the increase of expansion leads to minimization of pipe (initial) ovality.
- the JCO-E pipe thickness is reduced in a quasi-linear manner with respect to expansion level (expansion strain).
- the expansion increases the tensile strength of the JCO pipe in transverse direction, while degrades the corresponding compressive strength.
- the increase of expansion reduces the residual stresses of JCO pipe until the optimum expansion level, where the residual stresses minimization is achieved.

- for expansion strain values greater than optimum expansion, the degradation of compressive strength, due to Bauschinger effect, becomes dominant leading to reduction of the ultimate external pressure capacity.

As a final conclusion, the finite element model developed in the present research constitutes a very useful tool, capable of predicting geometrical and material properties of the JCO-E pipe, as well as its structural response within a good level of accuracy.

## **Chapter 4 - Idealized Analytical Modelling of the JCO-E Forming Process**

The use of the finite element modelling of the JCO-E forming process requires the definition of the forming parameters. This is a set of parameters identified by the pipe mill, and corresponds to a specific final product (JCO-E pipe). Changing the diameter-to-thickness ratio ( $D/t$ ) of the final product, this set should be revised, so that it constitutes the input for the finite element simulation of the corresponding JCO-E process for the new pipe. To simplify the modelling procedure, and understand better the influence of forming process on the residual stresses of the JCO-E pipe, the mechanical steps of JCO-E process have been idealized, following a procedure similar yet enhanced to the one reported in [5]. Using this approach, the modelling of JCO-E process is significantly less dependent on the specific details of the forming parameters, offering a simple and efficient tool for predicting material properties and the collapse pressure.

The dimensions of the plate, the circumferential expansion and the material model parameters, used to represent the elastic-plastic mechanical behavior of the plate during JCO-E forming process, are provided as input in the idealized model. The initial state (undeformed state) refers to a stress-free steel plate. During its deformation, the axial strain is considered constant ( $\varepsilon_z = \text{const.}$ ). This consideration has also been employed for the finite element modelling of JCO-E forming process and implies that the process is conducted under generalized plane strain conditions, or equivalently, the axial force developed during the forming process of pipe is zero. The idealized analysis, shown schematically in Figure 4.1, is conducted in five steps as follows:

- (1) pure bending of the plate into a cylinder
- (2) uniform “small” circumferential expansion of the cylinder
- (3) elastic unloading

- (4) circumferential expansion of the cylinder, associated with the expansion process
- (5) elastic unloading

In the finite element analysis, the mid-surface length of JCO pipe circumference is slightly greater than the plate width. To enable the idealized model to take into account the above increase of circumferential length, during the second step (2), the cylinder is expanded circumferentially up to a “small” strain, and in the next step (3), the circumferential tensile force developed is released to zero. Hence, at the end of third step, the pipe circumference essentially corresponds to the JCO pipe circumference obtained from the finite element analysis. Finally, the expansion stage (E) is simulated, similar to the second step (2), and after elastic unloading, the simulation of the JCO-E process is completed. Both the JCO and the finished pipe (JCO-E pipe) are circular with no variation of material properties around the circumference.

#### **4.1 Formulation of the idealized analytical model**

In this idealized model, the plate is assumed to deform uniformly along the longitudinal direction of pipe. In the transverse direction, the plate is subjected to pure bending and uniform expansion and, as a result, every position around the circumference of the pipe undergoes the same loading path. To predict the stresses of pipe during the idealized forming, an in-house program is developed, which it is sufficient in determining the state of stress and strain at specific points through the thickness  $t$ .

##### **4.1.1 Kinematics**

The kinematic relations proposed in the book by Brush and Almroth [34] are adopted, which are referred to the deformation of a circumferential line element considering in-plane bending. The strain of the line element  $\boldsymbol{\varepsilon}$  is decomposed in two parts as follows:

$$\boldsymbol{\varepsilon} = \bar{\boldsymbol{\varepsilon}}^0 + \frac{1}{2} \bar{\boldsymbol{\beta}}^2 \quad (4.1)$$

where  $\bar{\boldsymbol{\varepsilon}}^0$  is the extensional strain and  $\bar{\boldsymbol{\beta}}$  expresses the rotation of the element. It is assumed that plane sections originally normal to centroidal surface remain plane and normal during

deformation. As a result, equation (4.1) can be written with respect to the strain of a line element on the centroidal surface as:

$$\boldsymbol{\varepsilon} = \boldsymbol{\varepsilon}^0 + y\boldsymbol{\kappa} \quad (4.2)$$

where the curvature change  $\boldsymbol{\kappa}$  can be considered as the rate of change of the rotation  $\bar{\boldsymbol{\beta}}$  in the transverse direction and  $y$  is a coordinate variable that refers to the distance of the point from the centroidal surface ( $-t/2 \leq y \leq t/2$ ). The strain increment  $\dot{\boldsymbol{\varepsilon}}$  is identified by the rate form of equation (4.2) as follows:

$$\dot{\boldsymbol{\varepsilon}} = \dot{\boldsymbol{\varepsilon}}^0 + y\dot{\boldsymbol{\kappa}} \quad (4.3)$$

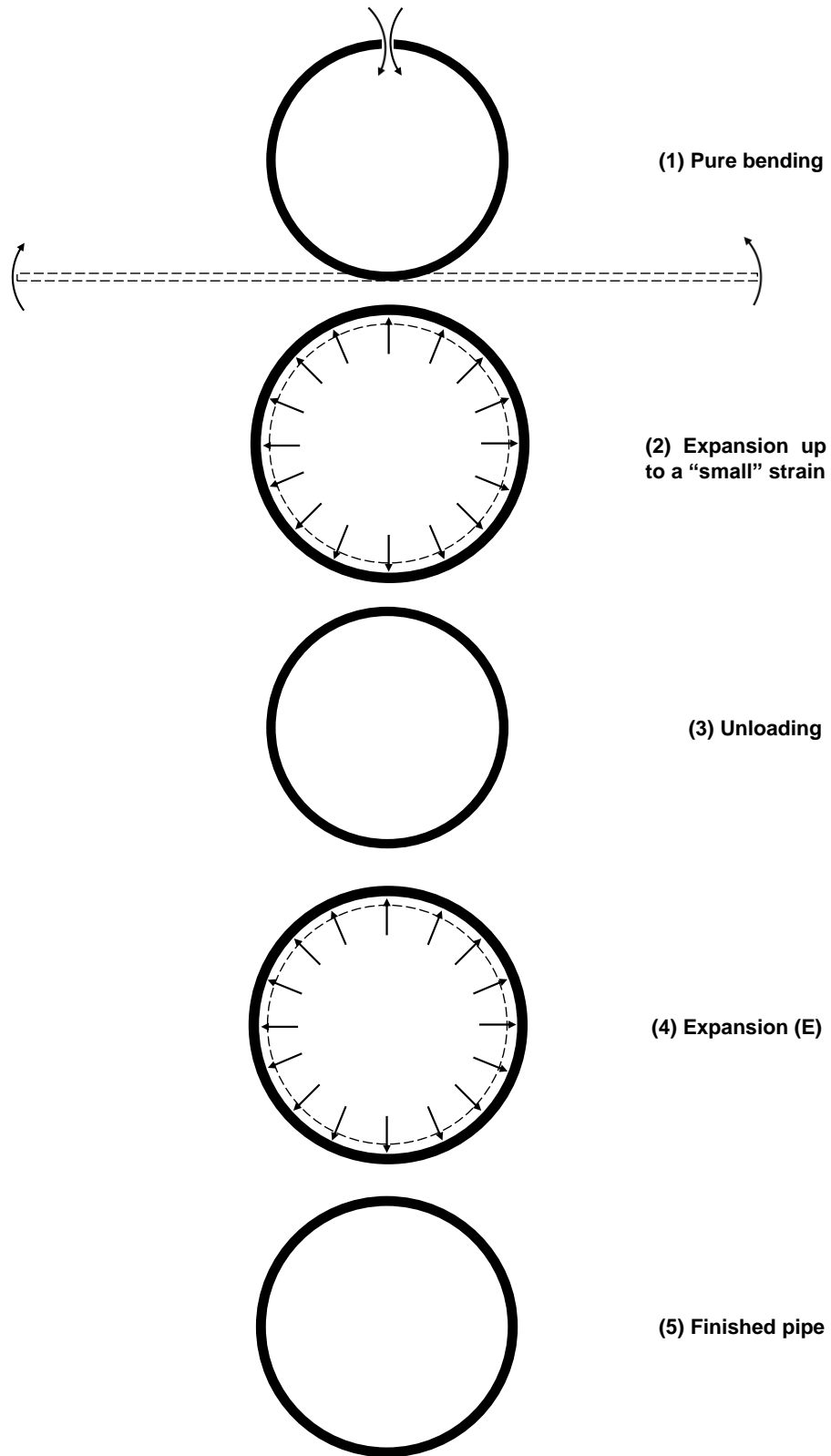


Figure 4.1: Steps used in the idealized modelling of the JCO-E forming process.



#### 4.1.2 Constitutive model

The nonlinear kinematic/isotropic (combined) hardening material model outlined in Section 2.2.1 is employed in the present analytical model in a form that refers to stress-strain relationships for the specific case of isotropic plasticity. This choice has been done, because for the plates examined in the present research, the effect of anisotropy on the structural performance of the corresponding JCO-E pipes is quite small; for the “relatively thin-walled” pipe, this effect is shown in Table 3.5, while the plate material of the “thick-walled” pipe is considered isotropic. Considering equation (2.1) and taking into account the values of  $N_{ij}$  in equation (2.11), the yield criterion results in the von Mises yield criterion, which is expressed as:

$$f_y = \frac{1}{2} \xi \cdot \xi - \frac{k^2(\varepsilon_q)}{3} = 0 \quad (4.4)$$

$$\xi \equiv \mathbf{s} - \mathbf{a}$$

Considering a cylindrical coordinate system is more convenient to prescribe the strain increment  $\dot{\boldsymbol{\varepsilon}}$  than a Cartesian coordinate system. In this curvilinear system, the vector form of the stress tensor  $\boldsymbol{\sigma}$  and the back stress tensor  $\boldsymbol{\alpha}$  is given by:

$$\boldsymbol{\sigma} = (\sigma_r, \sigma_\theta, \sigma_z)$$

$$\boldsymbol{\alpha} = (\alpha_r, \alpha_\theta, \alpha_z) \quad (4.5)$$

where  $(r, \theta, z)$  are the radial, circumferential, and longitudinal coordinates, respectively. The plate thickness is considered thin enough, so that the stress component in the radial/thickness direction  $\sigma_r$  is neglected. Therefore, the yield criterion (4.4) can be formulated as:

$$f_y = \sigma_e - k(\varepsilon_q) = 0 \quad (4.6)$$

where  $\sigma_e = \sqrt{\hat{\sigma}_\theta^2 - \hat{\sigma}_\theta \hat{\sigma}_z + \hat{\sigma}_z^2}$  and  $\hat{\sigma}_i$  denotes the difference  $\sigma_i - \alpha_i$ .

Considering that the equivalent plastic strain rate is equal to

$$\dot{\varepsilon}_q = \sqrt{\frac{2}{3} \dot{\boldsymbol{\varepsilon}}^p \cdot \dot{\boldsymbol{\varepsilon}}^p} \quad (4.7)$$

and utilizing the following relationship

$$\sigma_e^2 = \frac{3}{2} \xi \cdot \xi \quad (4.8)$$

the plastic flow is defined as:

$$\dot{\boldsymbol{\varepsilon}}^p = \dot{\lambda} \frac{\partial f_y}{\partial \boldsymbol{\sigma}} = \dot{\lambda} \frac{3}{2\sigma_e} \xi = \dot{\varepsilon}_q \frac{3}{2\sigma_e} \xi \quad (4.9)$$

Enforcing the consistency condition  $\dot{f}_y = 0$ , one results in the following expression for the equivalent plastic strain rate  $\dot{\varepsilon}_q$ :

$$\begin{aligned} \frac{\partial f_y}{\partial \boldsymbol{\sigma}} \cdot \dot{\boldsymbol{\sigma}} + \frac{\partial f_y}{\partial \mathbf{a}} \cdot \dot{\mathbf{a}} + \frac{\partial f_y}{\partial k} \cdot \dot{k} &= 0 \\ \frac{3}{2\sigma_e} \xi \cdot \dot{\boldsymbol{\sigma}} - \frac{3}{2\sigma_e} \xi \cdot \dot{\mathbf{a}} - \frac{dk(\varepsilon_q)}{d\varepsilon_q} \dot{\varepsilon}_q &= 0 \end{aligned} \quad (4.10)$$

$$\dot{\varepsilon}_q = \frac{(2\hat{\sigma}_\theta - \hat{\sigma}_z)(\dot{\sigma}_\theta - \dot{\alpha}_\theta) + (2\hat{\sigma}_z - \hat{\sigma}_\theta)(\dot{\sigma}_z - \dot{\alpha}_z)}{2\sigma_e \frac{dk(\varepsilon_q)}{d\varepsilon_q}}$$

Taking into account the kinematic hardening rule in equation (2.16) and using the following relationship, which relate the components of the back stress tensor and the corresponding components of its deviatoric part

$$\begin{Bmatrix} \dot{\alpha}_\theta \\ \dot{\alpha}_z \end{Bmatrix} = \begin{Bmatrix} 2\dot{a}_\theta + \dot{a}_z \\ 2\dot{a}_z + \dot{a}_\theta \end{Bmatrix} \quad (4.11)$$

the equivalent plastic strain rate  $\dot{\varepsilon}_q$  in equation (4.10) can be rewritten as:

$$\dot{\varepsilon}_q = \frac{1}{H} \left[ (2\hat{\sigma}_\theta - \hat{\sigma}_z) \dot{\sigma}_\theta + (2\hat{\sigma}_z - \hat{\sigma}_\theta) \dot{\sigma}_z - 3C(\varepsilon'_q) (\hat{\sigma}_\theta \dot{\varepsilon}_\theta^p + \hat{\sigma}_z \dot{\varepsilon}_z^p) \right] \quad (4.12)$$

where

$$H = 2\sigma_e \frac{dk(\varepsilon_q)}{d\varepsilon_q} - 3\gamma [\hat{\sigma}_\theta a_\theta + \hat{\sigma}_z a_z] \quad (4.13)$$

Substituting the  $\dot{\varepsilon}_q$  term from equation (4.12) in to equation (4.9), the incremental stress-strain relationships are given as follows:

$$\begin{Bmatrix} \dot{\hat{\sigma}}_{\theta} \\ \dot{\hat{\sigma}}_z \end{Bmatrix} = \begin{bmatrix} C_{11} & C_{12} \\ C_{12} & C_{22} \end{bmatrix} \begin{Bmatrix} \dot{\hat{\epsilon}}_{\theta} \\ \dot{\hat{\epsilon}}_z \end{Bmatrix} \quad (4.14)$$

where the instantaneous constitutive tensor  $\mathbf{D} = \mathbf{C}^{-1}$  is expressed as:

$$\mathbf{D} = \frac{1}{E} \begin{bmatrix} 1 + P(2\hat{\sigma}_{\theta} - \hat{\sigma}_z)^2 & -\nu + P(2\hat{\sigma}_{\theta} - \hat{\sigma}_z)(2\hat{\sigma}_z - \hat{\sigma}_{\theta}) \\ -\nu + P(2\hat{\sigma}_{\theta} - \hat{\sigma}_z)(2\hat{\sigma}_z - \hat{\sigma}_{\theta}) & 1 + P(2\hat{\sigma}_z - \hat{\sigma}_{\theta})^2 \end{bmatrix} \quad (4.15)$$

and  $P = \frac{E}{2\sigma_e [H + 3\sigma_e C(\epsilon'_q)]}$  for plastic loading and otherwise  $P = 0$ .

### 4.1.3 Numerical implementation

The numerical implementation of the above constitutive model follows the “elastic predictor – plastic corrector” scheme; this scheme has been described in Section 2.2.2. However, the out-of-plane strain in the plane stress problem of Section 4.1.2 is not defined kinematically. Decomposing the total strain increment  $\Delta\boldsymbol{\epsilon}$  in two parts, it can be written as:

$$\Delta\boldsymbol{\epsilon} = \Delta\bar{\boldsymbol{\epsilon}} + \Delta\epsilon_r \mathbf{b} \quad (4.16)$$

where  $\Delta\bar{\boldsymbol{\epsilon}}$ ,  $\mathbf{b}$  are defined as:

$$\begin{aligned} \Delta\bar{\boldsymbol{\epsilon}} &= \Delta\epsilon_{\theta} (\mathbf{e}_{\theta} \otimes \mathbf{e}_{\theta}) + \Delta\epsilon_z (\mathbf{e}_z \otimes \mathbf{e}_z) \\ \mathbf{b} &= (\mathbf{e}_r \otimes \mathbf{e}_r) \end{aligned} \quad (4.17)$$

The out-of-plane strain increment  $\Delta\epsilon_r$  is considered as an unknown.

Writing the total strain increment according to equation (4.16) and following a direct integration of the elasticity equation, elastic prediction can be stated as:

$$\begin{aligned} \boldsymbol{\sigma}_{n+1} &= \boldsymbol{\sigma}_n + \mathbf{D}\Delta\bar{\boldsymbol{\epsilon}} + \Delta\epsilon_r \mathbf{D}\mathbf{b} \\ \boldsymbol{\sigma}^{(e)} &\equiv \boldsymbol{\sigma}_{n+1} \end{aligned} \quad (4.18)$$

The restriction  $\sigma_r = 0$  has to be satisfied and, as a result, the strain increment  $\Delta\epsilon_r$  equals to:

$$\Delta\epsilon_r = \frac{-\nu}{1-\nu} (\Delta\epsilon_{\theta} + \Delta\epsilon_z) \quad (4.19)$$

Therefore, substituting the  $\Delta\epsilon_r$  term in to equation (4.18), one obtains:

$$\boldsymbol{\sigma}^{(e)} = \begin{Bmatrix} \sigma_{\theta,n} \\ \sigma_{z,n} \end{Bmatrix} + \mathbf{D}^{\text{ps}} \begin{Bmatrix} \Delta \varepsilon_{\theta} \\ \Delta \varepsilon_z \end{Bmatrix} \quad (4.20)$$

where  $\mathbf{D}^{\text{ps}}$  is the plane stress stiffness tensor:

$$\mathbf{D}^{\text{ps}} = \frac{E}{1-\nu^2} \begin{bmatrix} 1 & \nu \\ \nu & 1 \end{bmatrix} \quad (4.21)$$

Since no plastic loading takes place during the elastic step:

$$\begin{aligned} \mathbf{a}_{n+1} &= \mathbf{a}_n \\ \varepsilon_{q,n+1} &= \varepsilon_{q,n} \\ \varepsilon'_{q,n+1} &= \varepsilon'_{q,n} \end{aligned} \quad (4.22)$$

The elastic stress prediction is valid as long as the yield criterion  $f_y \leq 0$  (equation (4.6)) is satisfied at the end of the increment “n+1”.

If the above check in the yield criterion is not satisfied, the new state parameters are determined in detail in the following (plastic correction step). Using the Euler-backward numerical integration scheme, the integrated form of the flow rule (4.9) is written as:

$$\Delta \boldsymbol{\varepsilon}^p = \frac{3}{2} \frac{\Delta \varepsilon_q}{k(\varepsilon_{q,n+1})} (\mathbf{s}_{n+1} - \mathbf{a}_{n+1}) \quad (4.23)$$

Assuming that the total strain tensor is decomposed into elastic and plastic part, the integration of the general elasticity equation provides:

$$\boldsymbol{\sigma}_{n+1} = \boldsymbol{\sigma}_n + \mathbf{D} \Delta \boldsymbol{\varepsilon} - \mathbf{D} \Delta \boldsymbol{\varepsilon}^p \quad (4.24)$$

or equivalently,

$$\boldsymbol{\sigma}_{n+1} = \boldsymbol{\sigma}_n + \mathbf{D} \Delta \boldsymbol{\varepsilon} - \frac{3}{2} \frac{\Delta \varepsilon_q}{k(\varepsilon_{q,n+1})} \mathbf{D} (\mathbf{s}_{n+1} - \mathbf{a}_{n+1}) \quad (4.25)$$

In the above equation, the product  $\mathbf{D}(\mathbf{s}_{n+1} - \mathbf{a}_{n+1})$  is equal to  $2G(\mathbf{s}_{n+1} - \mathbf{a}_{n+1})$ , since the stress difference  $(\mathbf{s} - \mathbf{a})$  is a deviatoric tensor. Therefore, using this property and equation (4.16), equation (4.25) can be written as:

$$\boldsymbol{\sigma}_{n+1} = \bar{\boldsymbol{\sigma}}^{(e)} + \Delta\varepsilon_r \mathbf{D}\mathbf{b} - \frac{3G}{k(\varepsilon_{q,n+1})} \Delta\varepsilon_q (\mathbf{s}_{n+1} - \mathbf{a}_{n+1}) \quad (4.26)$$

where

$$\bar{\boldsymbol{\sigma}}^{(e)} = \boldsymbol{\sigma}_n + \mathbf{D}\Delta\bar{\boldsymbol{\varepsilon}} \quad (4.27)$$

The product  $\mathbf{D}\mathbf{b}$  can be decomposed in a hydrostatic and a deviatoric part as follows:

$$\begin{aligned} \mathbf{D}\mathbf{b} &= \mathbf{D} \left[ \frac{1}{3} \mathbf{I} + \mathbf{b}' \right] \\ \mathbf{D}\mathbf{b} &= \mathbf{K}\mathbf{I} + 2G\mathbf{b}' \end{aligned} \quad (4.28)$$

and using this decomposition and equation (4.26), the hydrostatic and the deviatoric part of the stress at the end of the increment  $\boldsymbol{\sigma}_{n+1}$  are computed as follows:

$$\begin{aligned} \mathbf{p}_{n+1} &= \bar{\mathbf{p}}^{(e)} + \Delta\varepsilon_r \mathbf{K}\mathbf{I} \\ \mathbf{s}_{n+1} &= \bar{\mathbf{s}}^{(e)} + 2\Delta\varepsilon_r G\mathbf{b}' - \frac{3G}{k(\varepsilon_{q,n+1})} \Delta\varepsilon_q (\mathbf{s}_{n+1} - \mathbf{a}_{n+1}) \end{aligned} \quad (4.29)$$

Using equation (4.23), the integration of kinematic hardening rule (equation (2.16)) results in:

$$\mathbf{a}_{n+1} = \frac{1}{1 + \gamma\Delta\varepsilon_q} \left[ \mathbf{a}_n + \frac{3C(\varepsilon'_{q,n+1})}{2k(\varepsilon_{q,n+1})} \Delta\varepsilon_q (\mathbf{s}_{n+1} - \mathbf{a}_{n+1}) \right] \quad (4.30)$$

At the end of the increment  $n+1$ , the state parameters should satisfy the von Mises yield criterion (equation (4.4)). Therefore, using equations (4.29) and (4.30), one results in the following algebraic equation for the von Mises criterion:

$$\begin{aligned} & \frac{1}{3} \left( \frac{1}{\text{AFACT}} \right)^2 \left[ \frac{3}{2} (\bar{\mathbf{s}}^{(e)} \cdot \bar{\mathbf{s}}^{(e)}) + 4\Delta\varepsilon_r^2 G^2 + \frac{3}{2} \left( \frac{1}{1 + \gamma\Delta\varepsilon_q} \right)^2 (\mathbf{a}_n \cdot \mathbf{a}_n) \right] + \\ & + \left( \frac{1}{\text{AFACT}} \right)^2 \left[ 2\Delta\varepsilon_r G (\bar{\mathbf{s}}^{(e)} \cdot \mathbf{b}') - \frac{1}{1 + \gamma\Delta\varepsilon_q} (\bar{\mathbf{s}}^{(e)} \cdot \mathbf{a}_n) - 2\Delta\varepsilon_r G (\mathbf{b}' \cdot \mathbf{a}_n) \right] = \\ & = \frac{k^2(\varepsilon_{q,n+1})}{3} \end{aligned} \quad (4.31)$$

where

$$\text{AFACT} = 1 + \frac{3}{k(\varepsilon_{q,n+1})} \left[ G + \frac{C(\varepsilon'_{q,n+1})}{2(1 + \gamma\Delta\varepsilon_q)} \right] \Delta\varepsilon_q \quad (4.32)$$

In equation (4.31), the increment of equivalent plastic strain  $\Delta\varepsilon_q$  and the strain increment  $\Delta\varepsilon_r$  are the two unknowns for our scheme. For the determination of  $\Delta\varepsilon_r$  and  $\Delta\varepsilon_q$ , an additional equation is required. This equation should stem from the plane stress condition. Requiring plane stress condition to apply at increment  $n+1$ :

$$\begin{aligned} \sigma_{r,n+1} &= 0 \\ s_{r,n+1} + p_{r,n+1} &= 0 \end{aligned} \quad (4.33)$$

With the use of equation (4.29) and equation (4.30), the stress component  $s_{r,n+1}$  can be written by eliminating the term  $a_{r,n+1}$  as follows:

$$s_{r,n+1} = B \left( \bar{s}_r^{(e)} + \frac{4}{3} \Delta\varepsilon_r G + \frac{3G}{k(\varepsilon_{q,n+1})} \Gamma \Delta\varepsilon_q \frac{1}{1 + \gamma\Delta\varepsilon_q} a_{r,n} \right) \quad (4.34)$$

where

$$\begin{aligned} \Gamma &= \frac{1}{1 + \frac{3C(\varepsilon'_{q,n+1})}{2k(\varepsilon_{q,n+1})} \Delta\varepsilon_q \frac{1}{1 + \gamma\Delta\varepsilon_q}} \\ B &= \frac{1}{1 + \frac{3G}{k(\varepsilon_{q,n+1})} \Delta\varepsilon_q \left( 1 - \frac{3C(\varepsilon'_{q,n+1})}{2k(\varepsilon_{q,n+1})} \Gamma \Delta\varepsilon_q \frac{1}{1 + \gamma\Delta\varepsilon_q} \right)} \end{aligned} \quad (4.35)$$

Therefore, taking into account equation (4.29) and equation (4.30), the final form of equation (4.33) results in:

$$B \left( \bar{s}_r^{(e)} + \frac{4}{3} \Delta\varepsilon_r G + \frac{3G}{k(\varepsilon_{q,n+1})} \Gamma \Delta\varepsilon_q \frac{1}{1 + \gamma\Delta\varepsilon_q} a_{r,n} \right) + \bar{p}_r^{(e)} + \Delta\varepsilon_r K = 0 \quad (4.36)$$

Equations (4.31) and (4.36) are solved as a system of two equations with two unknowns ( $\Delta\varepsilon_r$ ,  $\Delta\varepsilon_q$ ) using the Newton-Raphson method. To initiate this iterative procedure, it is assumed that the initial value for both  $\Delta\varepsilon_r$  and  $\Delta\varepsilon_q$  are zero. At the end of the increment, the

equivalent plastic strain  $\varepsilon_{q,n+1}$  and the equivalent cumulative strain  $\varepsilon'_{q,n+1}$  are computed as follows:

$$\begin{aligned}\varepsilon_{q,n+1} &= \varepsilon_{q,n} + \Delta\varepsilon_q \\ \varepsilon'_{q,n+1} &= \varepsilon'_{q,n} + \Delta\varepsilon_q\end{aligned}\tag{4.37}$$

Finally, taking into consideration equation (4.37), the corresponding stress  $\mathbf{s}_{n+1}$  and back stress  $\mathbf{a}_{n+1}$  are calculated using equations (4.29) and (4.30), respectively.

## 4.2 Steps of the idealized analytical model

During the idealized process, the incremental stress-strain relationships reported in Section 4.1.3 are incorporated in an in-house computer code written in FORTRAN programming language. The algorithm of the code is briefly presented in the flowchart shown in Figure 4.2. The loading history is obtained by calculating and monitoring the state parameters (i.e. stresses, solution dependent variables) at several points  $k$  through the thickness in an iterative manner. Initially, the values of state parameters at points  $k$  are set equal to zero. At each forming step  $m$ , where  $m=1,\dots,5$ , the strain increment in the transverse direction  $\Delta\varepsilon_\theta$  and the strain increment in the longitudinal direction  $\Delta\varepsilon_z$  are prescribed for a point across the thickness with coordinate  $y_j$ , where  $-t/2 \leq y_j \leq t/2$ , and subsequently the corresponding state parameters are computed through the subroutine “ASPC” (Algorithm for State Parameters Computation). This subroutine is employed to solve the equations reported in Section 4.1.3. The above computation is performed for all points  $k$ . Once the state parameters are computed for all points  $y_j, j=1,\dots,k$ , at the end of increment  $n+1$ , they are stored in matrix  $\mathbf{State}_{m,n+1}(y_j)$  and constitute the updated initial state parameters for the next increment. The iterative procedure is continued until the index  $n+1$  becomes equal to the total number of the increments  $inc$ . The input variables are:

- the plate width
- the plate thickness
- the material model parameters
- the circumferential expansion
- the total number of points through the thickness  $k$

- the total number of increments inc

The last two variables are directly related to the accuracy of the calculations.

During the forming process, the pipe is free to deform in the longitudinal direction and this is achieved imposing zero axial force:

$$\Delta N_z = 0 \quad (4.38)$$

where

$$\Delta N_z = \int_{-t/2}^{t/2} \Delta \sigma_z dy \quad (4.39)$$

Substituting the integrated form of equations (4.3) and (4.14) into the equation (4.38), one can express the above equation as:

$$\int_{-t/2}^{t/2} \left[ C_{12} (\Delta \varepsilon_\theta^0 + y \Delta \kappa_\theta) + C_{22} (\Delta \varepsilon_z^0 + y \Delta \kappa_z) \right] dy = 0 \quad (4.40)$$

Furthermore, during the forming process, there is no change in curvature in the longitudinal direction. Therefore, equation (4.40) can be simplified as follows:

$$\int_{-t/2}^{t/2} \left[ C_{12} (\Delta \varepsilon_\theta^0 + y \Delta \kappa_\theta) + C_{22} \Delta \varepsilon_z^0 \right] dy = 0 \quad (4.41)$$

Similar to equation (4.38), the incremental form of circumferential force  $N_\theta$  is defined as follows:

$$\Delta N_\theta = \int_{-t/2}^{t/2} \Delta \sigma_\theta dy \quad (4.42)$$



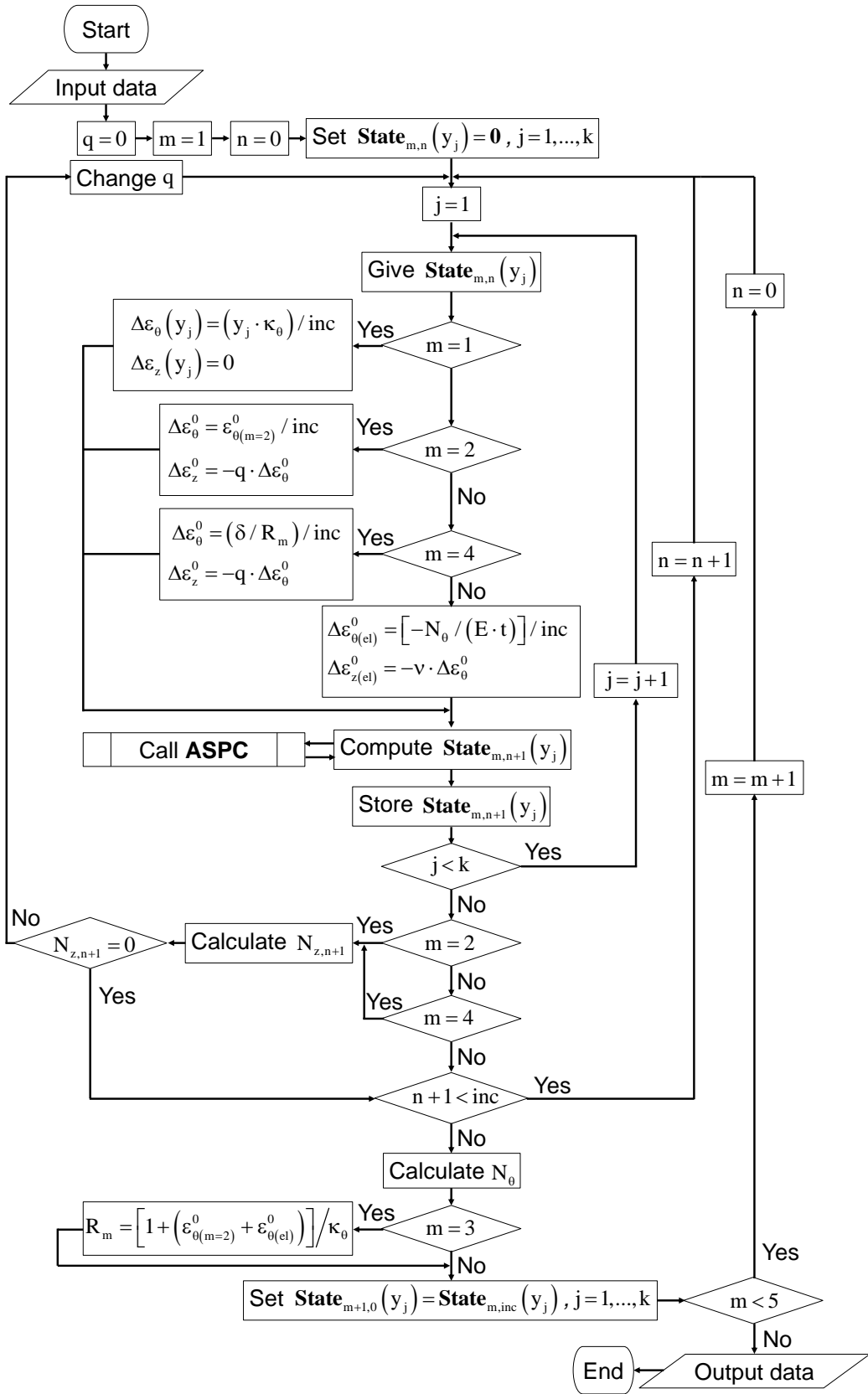


Figure 4.2: Flowchart of the computer code representing the idealized forming steps.

### 4.2.1 First step: bending

In the first step ( $m=1$ ), the plate is bent into a circular configuration. The total curvature change in the transverse direction  $\kappa_0$  is calculated dividing the value  $2\pi$  by the width of the plate, while the extensional strain  $\varepsilon_0^0$  during this process is considered zero. Equation (4.41) is the condition to be fulfilled for having zero axial force during bending, which means that the strain in the longitudinal direction  $\varepsilon_z^0$  should be zero. At the end of the step, the circumferential force  $N_0$  takes zero value, because only bending deformation is applied during this step.

### 4.2.2 Second step: small expansion

In the second step ( $m=2$ ), shown in the flowchart of Figure 4.2, the circular pipe configuration is subjected to a uniform circumferential “small” expansion  $\varepsilon_{\theta(m=2)}^0$ ; for each point  $y_j$ , the total strain in the transverse direction is equal to  $\varepsilon_{\theta(m=2)}^0$ . The strain increment in the longitudinal direction  $\Delta\varepsilon_z^0$  is determined by equation (4.41). Hence, in this case,  $\Delta\varepsilon_z^0$  is expressed as:

$$\Delta\varepsilon_z^0 = -q\Delta\varepsilon_0^0 = -q\left(\frac{\varepsilon_{\theta(m=2)}^0}{\text{inc}}\right) \quad (4.43)$$

where  $\text{inc}$  is the total number of increments and

$$q = \frac{\int_{-t/2}^{t/2} C_{12} dy}{\int_{-t/2}^{t/2} C_{22} dy} \quad (4.44)$$

The strain increment  $\Delta\varepsilon_z^0$  is a function of  $q$ , which is an integral found using the variables  $C_{12}$  and  $C_{22}$  of equation (4.14). Because this integral accounts for the state parameters of all points  $y_j$ ,  $j=1, \dots, k$ , an iterative procedure is required, so that  $q$  is implicitly calculated, or equivalently,  $q$  results in zero axial force at the end of the increment ( $N_{z,n+1} = 0$ ). The steps of this iterative procedure are described below:

It is assumed first that  $\Delta\varepsilon_z^0$  is zero (trial value). Subsequently, the state parameters are computed at the end of the increment  $n+1$ . The value of  $N_{z,n+1}$  is calculated according to equation (4.39), and a zero check is performed. If the check is valid, the assumed value of  $\Delta\varepsilon_z^0$  is correct, the state parameters are stored and the procedure is continued to the next increment. Otherwise, a new trial value for  $\Delta\varepsilon_z^0$  is assumed and the above iteration procedure is repeated until the trial value of  $\Delta\varepsilon_z^0$  fulfills the criterion of zero axial force at the end of the increment  $n+1$ .

At the end of the step, the circumferential force  $N_{\theta(m=2)}$  is computed using equation (4.45) and the analysis proceeds to the next step ( $m = 3$ ).

$$N_{\theta} = \int_{-t/2}^{t/2} \sigma_{\theta} dy \quad (4.45)$$

### 4.2.3 Third step: unloading

During the third step, the pipe is incrementally unloaded, and its final configuration corresponds to the idealized JCO pipe. Considering elastic unloading, the integrated form of the stress-strain relationships presented in equation (4.14) is simplified to the following form:

$$\begin{Bmatrix} \Delta\sigma_{\theta} \\ \Delta\sigma_z \end{Bmatrix} = \frac{E}{1-\nu^2} \begin{bmatrix} 1 & \nu \\ \nu & 1 \end{bmatrix} \begin{Bmatrix} \Delta\varepsilon_{\theta} \\ \Delta\varepsilon_z \end{Bmatrix} \quad (4.46)$$

Using equation (4.46) and the condition of zero axial force, expressed in equation (4.38), the strain increment in the longitudinal direction is determined:

$$\Delta\varepsilon_z^0 = -\nu\Delta\varepsilon_{\theta}^0 \quad (4.47)$$

Combining equations (4.42), (4.46) and (4.47), the incremental form of  $N_{\theta}$  is obtained:

$$\Delta N_{\theta} = (E \cdot t) \Delta\varepsilon_{\theta}^0 \quad (4.48)$$

At the end of elastic unloading, the circumferential force should be zero and, as a result, the strain increment in the transverse direction is given by

$$\Delta \varepsilon_{\theta}^0 = - \left( \frac{N_{\theta(m=2)}}{E \cdot t} \right) \frac{1}{\text{inc}} \quad (4.49)$$

The mean radius of JCO pipe can be readily defined as follows:

$$R_{m(\text{JCO})} = \frac{1 + \varepsilon'_E}{\kappa_{\theta}} \quad (4.50)$$

In the above expression (4.50), the expansion strain  $\varepsilon'_E$  is calculated, so that it accounts for the elastic rebound and defined as:

$$\varepsilon'_E = \varepsilon_{\theta(m=2)}^0 - \frac{N_{\theta(m=2)}}{E \cdot t} \quad (4.51)$$

The value of expansion strain  $\varepsilon'_E$  corresponds to the one calculated at the end of the finite element simulation of JCO forming process, which is computed as follows:

$$\varepsilon'_E = \frac{C_{\text{before,E}} - W}{W} \quad (4.52)$$

where  $C_{\text{before,E}}$  and  $W$  are the mid-surface length of JCO pipe circumference and the plate width, respectively.

#### 4.2.4 Fourth and fifth steps: expansion and unloading

The calculations of the fourth ( $m=4$ ) and the fifth ( $m=5$ ) step are similar to the second and third step, respectively. During the expansion step, the pipe (JCO pipe) is incrementally subjected to a circumferential tension, which is introduced by the user as an input parameter. The imposed total circumferential strain for each point  $y_j$ ,  $j=1, \dots, k$ , is equal to

$$\varepsilon_{\theta(m=4)}^0 = \frac{\delta}{R_{m(\text{JCO})}} \quad (4.53)$$

where the variable “ $\delta$ ” is an input parameter that refers to the radial displacement of the JCO pipe mid-surface due to the outward displacement of the expander segments. At the end of the expansion step ( $m=4$ ), the circumferential force developed  $N_{\theta(m=4)}$  is calculated.

Subsequently, the analysis proceeds to the unloading step (last step), as described in Section 4.2.3.

Finally, the mean radius of the JCO-E pipe is given by

$$R_{m(\text{JCO-E})} = R_{m(\text{JCO})} (1 + \varepsilon_E) \quad (4.54)$$

where the expansion strain  $\varepsilon_E$  is defined as:

$$\varepsilon_E = \varepsilon_{\theta(m=4)}^0 - \frac{N_{\theta(m=4)}}{E \cdot t} \quad (4.55)$$

The pipe thickness  $t_{\text{JCO-E}}$  is considered uniform and approximated by:

$$t_{\text{JCO-E}} = \frac{t_{\text{JCO}}}{\sqrt{1 + \varepsilon_E}} \quad (4.56)$$

where

$$t_{\text{JCO}} = \frac{t_{\text{plate}}}{\sqrt{1 + \varepsilon'_E}} \quad (4.57)$$

The derivation of equations (4.56) and (4.57) takes into account the thickness reduction due to expansion assuming that at the end of bending step (step 1), the plastic zone covers the entire pipe thickness. Therefore, the volume change  $dV$  of a material element after expansion, which is computed as follows:

$$dV = V (\varepsilon_r^p + \varepsilon_\theta^p + \varepsilon_z^p) \quad (4.58)$$

should be zero, because the plastic strain rate tensor  $\boldsymbol{\varepsilon}^p$  is deviatoric. Furthermore, it is considered that the change in length of a material element in the thickness direction  $r$ , due to expansion, is equal to the corresponding one in the longitudinal direction  $z$ , so that:

$$\frac{dr - dr_0}{dr_0} = \frac{dz - dz_0}{dz_0} \quad (4.59)$$

The considerations discussed above for the pipe thickness calculation are shown in more detail in the sketches of Figure 4.3. In addition, in following Sections, these considerations are demonstrated capable of calculating the thickness of JCO-E pipe in accordance with the average thickness of pipe calculated from the finite element model.

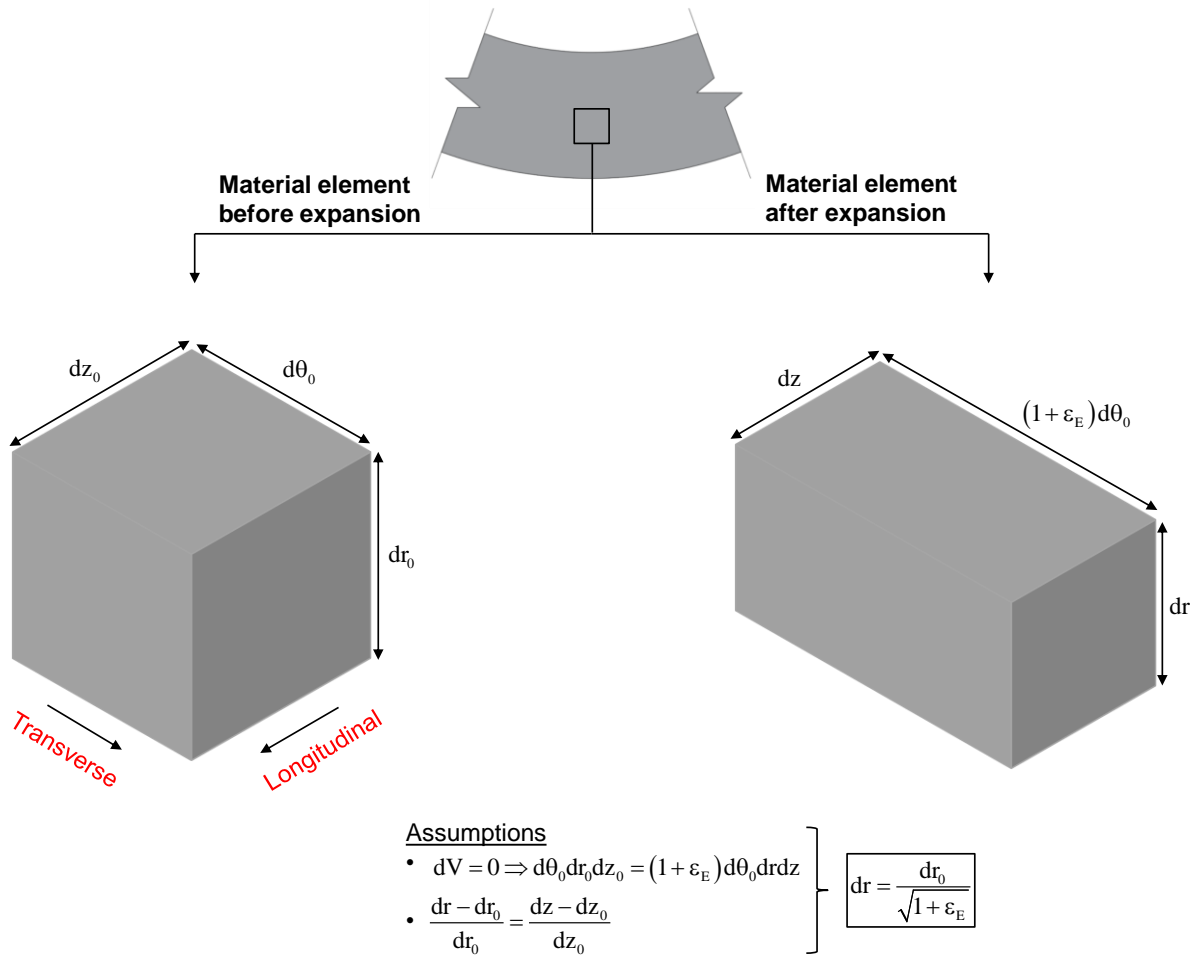


Figure 4.3: Deformation of a material element of the idealized pipe due to (uniform) expansion.

During the idealized analysis and at the end of increment  $n+1$ , the integration of forces  $N_{z,n+1}$  and  $N_{\theta,n+1}$  is discretized using the trapezoidal rule for the interval  $\Delta y$ . Upon completion of the iterative procedure, the output data provide (a) the stress-strain history during forming process and (b) the state parameters at the end of simulation, for  $k$  points through the thickness.

### 4.3 Pipe material properties

At the end of JCO-E forming process, the stress-strain response of line pipe is modified with respect to the one of plate material. To experimentally evaluate the JCO-E pipe material properties in transverse direction, test coupons are extracted from the transverse

direction of JCO-E pipe (circumferential coupons) and tested in uniaxial compression or tension. Based on the above experimental procedure, a one-dimensional model is established for the simulation of a circumferential coupon, which is extracted from the idealized JCO-E pipe, and subsequently, subjected to uniaxial compression or tension. This model takes into account the material model parameters (input data) and is shown in the flowchart of Figure 4.4.

Initially, the one-dimensional model represents the extraction of one circumferential coupon. It is assumed that the position where the actual coupon is extracted from is near the through thickness position of point  $y_j$ , where  $-t/2 \leq y_j \leq t/2$  and  $t$  is the thickness of idealized JCO-E pipe. It is noted that the state parameters locked into this point has been recorded in matrix  $\mathbf{State}_{s,inc}(y_j)$ . Furthermore, elastic unloading is considered during extraction. Hence, the residual stresses are reduced to zero ( $\boldsymbol{\sigma}(y_j) = 0$ ), as well as the state parameters that change during an elastic event.

Subsequently, the point  $y_j$  is incrementally loaded in the transverse direction to a uniaxial compression or tension strain  $\varepsilon_\theta$ . The state parameters are calculated in each strain increment  $\Delta\varepsilon_\theta$ . The incremental stress-strain relationships that refer to elastic uniaxial loading in transverse direction can be described by the incremental form of Hooke's law as follows:

$$\begin{Bmatrix} \dot{\sigma}_r \\ \dot{\sigma}_\theta \\ \dot{\sigma}_z \end{Bmatrix} = \begin{Bmatrix} 0 \\ E\dot{\varepsilon}_\theta \\ 0 \end{Bmatrix} \quad (4.60)$$

In addition,

$$\dot{\varepsilon}_z = \dot{\varepsilon}_r = -\nu\dot{\varepsilon}_\theta \quad (4.61)$$

Integrating equation (4.60), one results in:

$$\begin{aligned} \sigma_{r,n+1} &= \sigma_{z,n+1} = 0 \\ \sigma_{\theta,n+1} &= \sigma_{\theta,n} + E\Delta\varepsilon_\theta \end{aligned} \quad (4.62)$$

Since no plastic loading occurs during the elastic step:

$$\begin{aligned}
\mathbf{a}_{n+1} &= \mathbf{a}_n \\
\varepsilon_{q,n+1} &= \varepsilon_{q,n} \\
\varepsilon'_{q,n+1} &= \varepsilon'_{q,n}
\end{aligned} \tag{4.63}$$

In the present study, at the end of the increment  $(n + 1)$ , a check is performed by substituting the state parameters of equations (4.62) and (4.63) into equation (4.4). Elastic loading is valid, if the yield criterion  $f_{y,n+1} \leq 0$  is satisfied. Otherwise, if the yield criterion is not satisfied, a plastic correction should be performed.

In case of the plane stress problem discussed in Section 4.1.3, the plastic correction is expressed by equations (4.23) – (4.37). Herein, the strain increment  $\Delta\varepsilon_z$  is set equal to the strain increment  $\Delta\varepsilon_r$ , so that equations (4.23) – (4.37) are transformed and correspond to the plastic correction of the present problem (uniaxial loading in transverse direction). It is noted that the plastic strain increment in the transverse direction  $\Delta\varepsilon_\theta^p$  is known, while the strain increments in the thickness and the longitudinal direction can be computed using the following equation:

$$\text{tr}(\Delta\boldsymbol{\varepsilon}^p) = 0 \tag{4.64}$$

which expresses the fact that the plastic strain rate tensor is deviatoric (incompressibility of plastic deformation). Therefore, the plastic strain rate tensor can be written in vector form as follows:

$$\Delta\boldsymbol{\varepsilon}^p = (\Delta\varepsilon_r^p, \Delta\varepsilon_\theta^p, \Delta\varepsilon_z^p) = \left( -\frac{1}{2}\Delta\varepsilon_\theta^p, \Delta\varepsilon_\theta^p, -\frac{1}{2}\Delta\varepsilon_\theta^p \right) \tag{4.65}$$

and the equivalent plastic strain increment is given by:

$$\Delta\varepsilon_q = \sqrt{\frac{2}{3}\Delta\boldsymbol{\varepsilon}^p \cdot \Delta\boldsymbol{\varepsilon}^p} = \Delta\varepsilon_\theta^p \tag{4.66}$$

At the end of the iterative procedure, the resultant monotonic circumferential stress-strain curve is obtained. The prediction of the one-dimensional model is independent of the location of point  $y_j$  in the circumferential direction, because the idealized model does not assume any variation around the pipe cross-section.



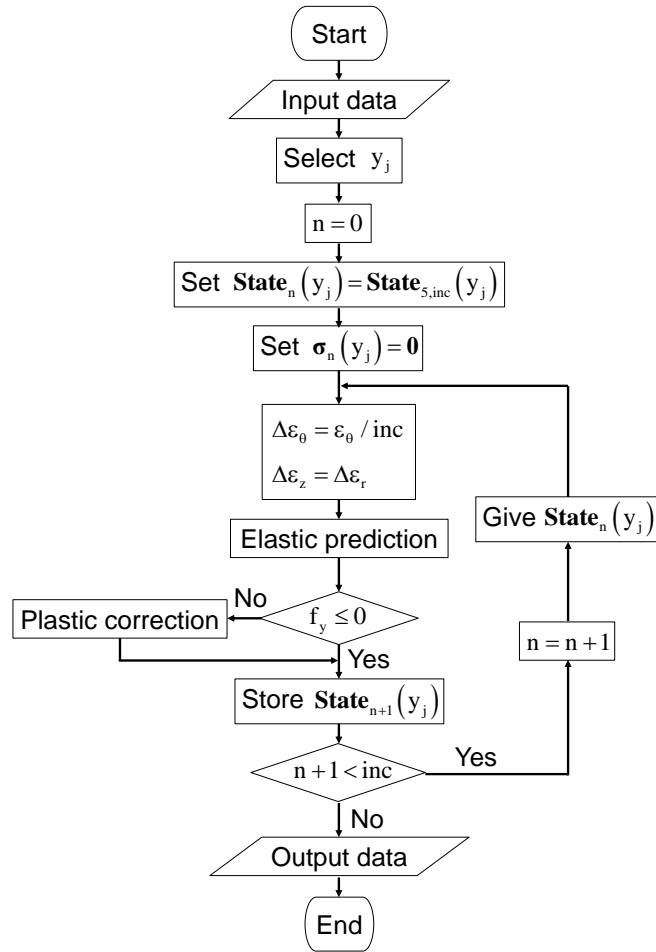


Figure 4.4: Flowchart of the code corresponding to the one-dimensional model.

#### 4.4 Application of idealized model to relatively thin-walled JCO-E pipe

In the idealized model, a total of nine points ( $k=9$ ) are selected through the plate thickness. Furthermore, the dimensions of plate are shown in Figure 3.1 and its elastoplastic material behavior is described by MAT1 material parameters, presented in Table 3.1, assuming isotropic plasticity ( $\sigma_{0,x} = \sigma_{0,y} = \sigma_{0,z} = 520\text{MPa}$ ). Figure 4.5 presents the predicted thickness of idealized pipe, calculated from equation (4.56), and the average thickness of pipe obtained from the corresponding finite element simulation  $t_{\text{average,FEM}}$ , with respect to the applied expansion strain; the average thickness  $t_{\text{average,FEM}}$  refers to the mean value of pipe thickness at 90, 180 and 270 degrees.

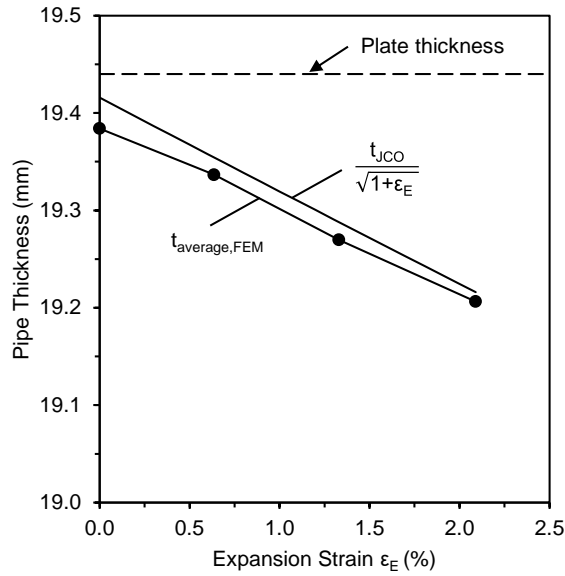


Figure 4.5: Predicted thickness of the relatively thin-walled JCO-E pipe in terms of expansion strain, obtained from equation (4.56) and from finite element model.

Considering expansion strain  $\epsilon_E$  equal to 1.33%, stress-strain histories in the transverse and the longitudinal direction of JCO-E pipe are depicted in Figure 4.6 and Figure 4.7, respectively. These are obtained from the idealized model (IM) and the finite element model (FEM), and refer to the extreme points (i.e. the inner and the outer point of pipe wall). One should underline that in the idealized model, the stress-strain history of a point is independent of its circumferential position. On the contrary, in the finite element model, the stress-strain path of a point depends on its position with respect to the forming tools. Hence, for a fair comparison between the models, in Figure 4.6 and in Figure 4.7, the FEM results refer to points, whose strains at the end of JCO process are almost identical with the corresponding ones calculated from idealized model. The stress-strain states corresponding to the JCO and JCO-E pipe are indicated in the stress-strain curves with arrows, where the color of arrow refers to the model adopted.

Following the idealized analysis of JCO-E forming process, accounting for  $\epsilon_E = 1.33\%$ , the one-dimensional model is used to predict the stress-strain response of pipe material in transverse direction, for the inner and the outer point of pipe wall (extreme points). To assess the ability of one-dimensional model to predict the material properties, similar calculations based on the finite element model have also been performed.

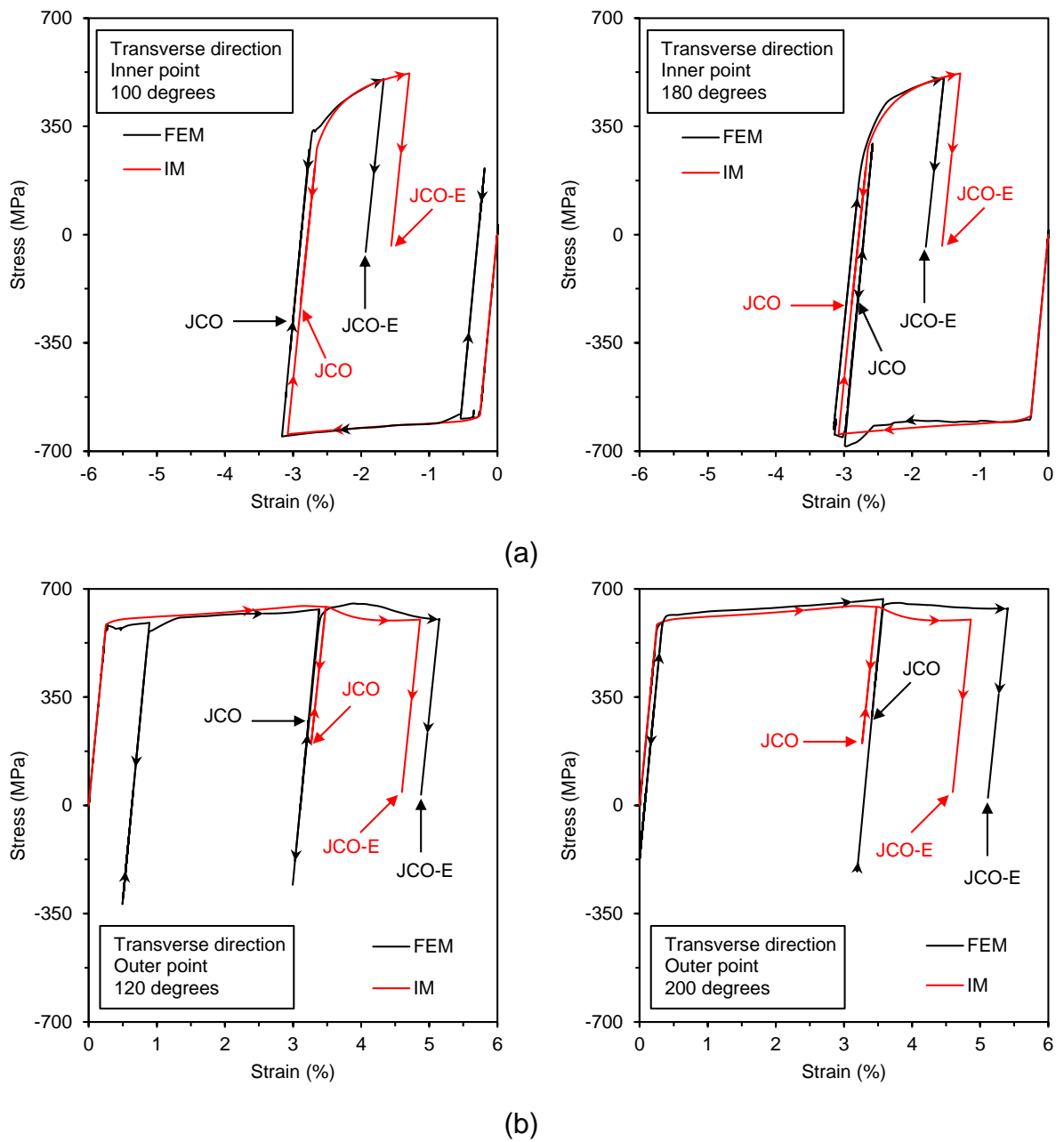


Figure 4.6: Stress-strain history in the transverse direction of JCO-E pipe ( $\epsilon_E = 1.33\%$ ), calculated at (a) the inner and (b) the outer points of pipe wall.

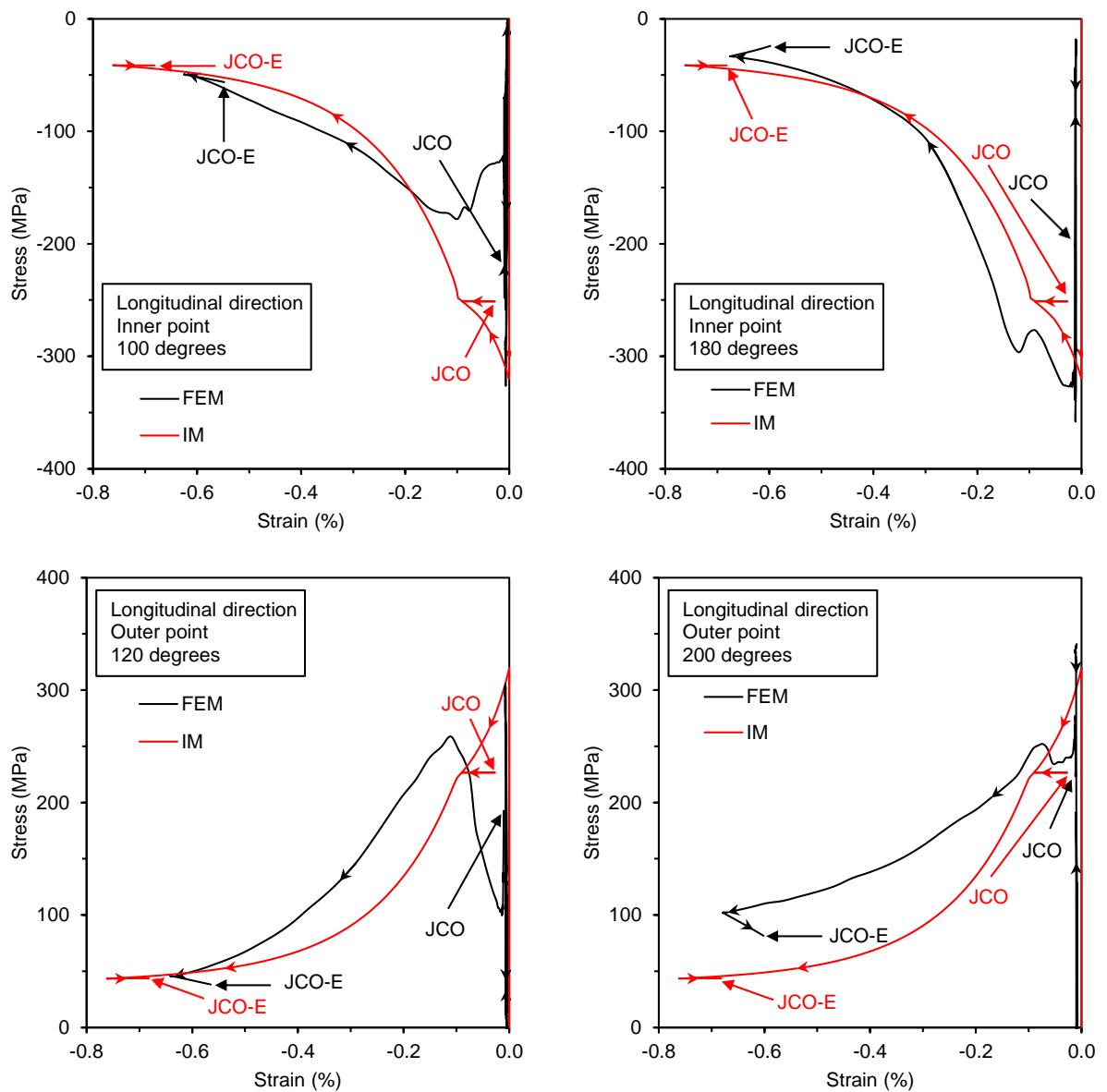


Figure 4.7: Stress-strain history during the JCO-E forming process in the longitudinal direction; the value of expansion strain  $\epsilon_E$  is 1.33%.

These calculations are conducted using the finite element procedure described in Section 2.5, for the positions around the pipe circumference shown in Figure 4.6 (or Figure 4.7). In this case, according to the numbering of elements in Figure 3.15, the stress-strain response of an extreme inner or extreme outer integration point is referred to as “prediction - 1” or “prediction - 8”, respectively. The compressive and the tensile responses are depicted in Figure 4.8 and Figure 4.9, respectively. In both one-dimensional model and finite element procedure, the elastic and the post-yielding hardenings are identical. There is also a small

variation of the values of yield strength calculated from the finite element model, which is attributed to the non-uniform expansion applied to JCO pipe, during the expansion process.

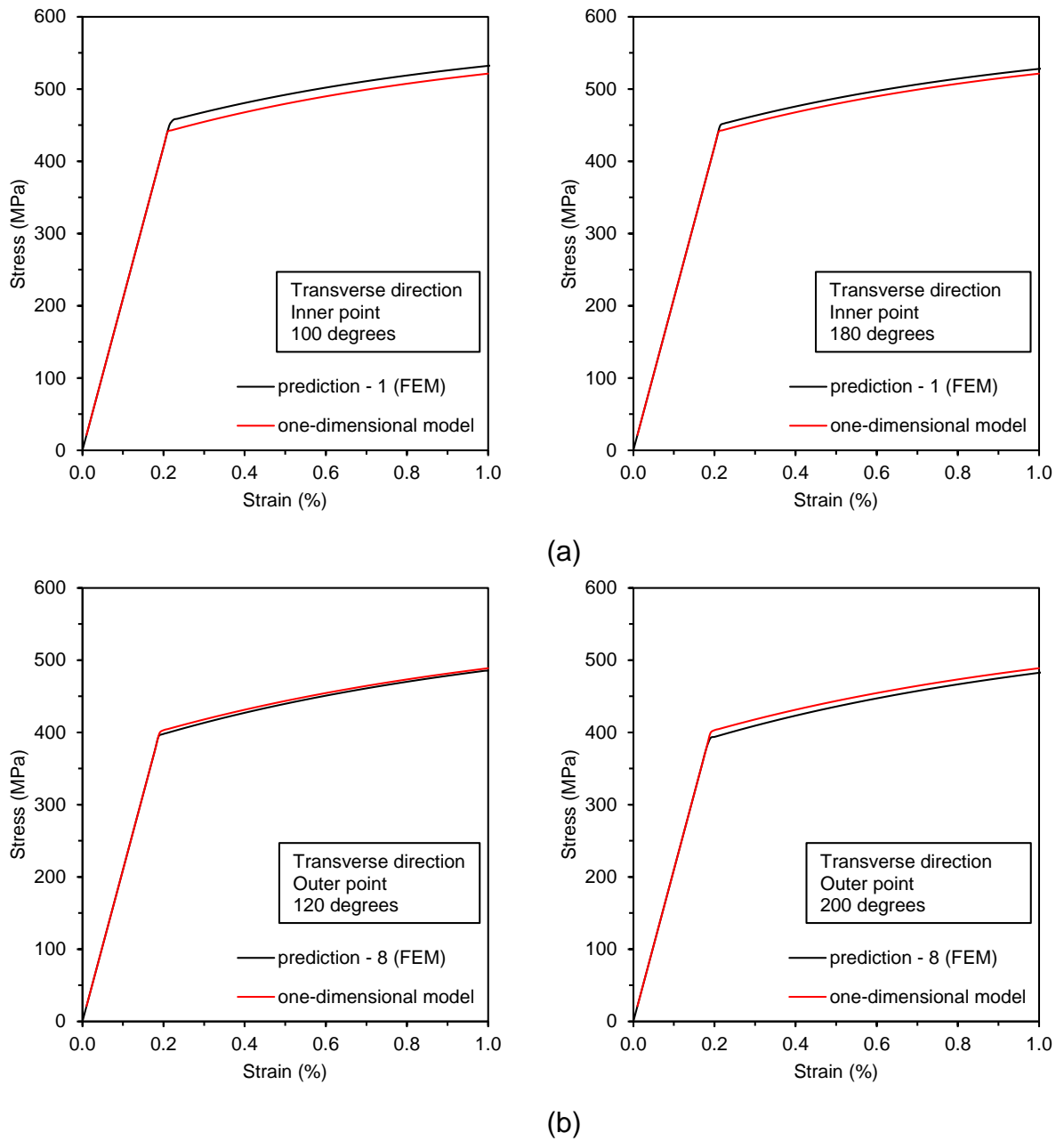


Figure 4.8: Predicted compressive stress-strain responses in the transverse direction of pipe.

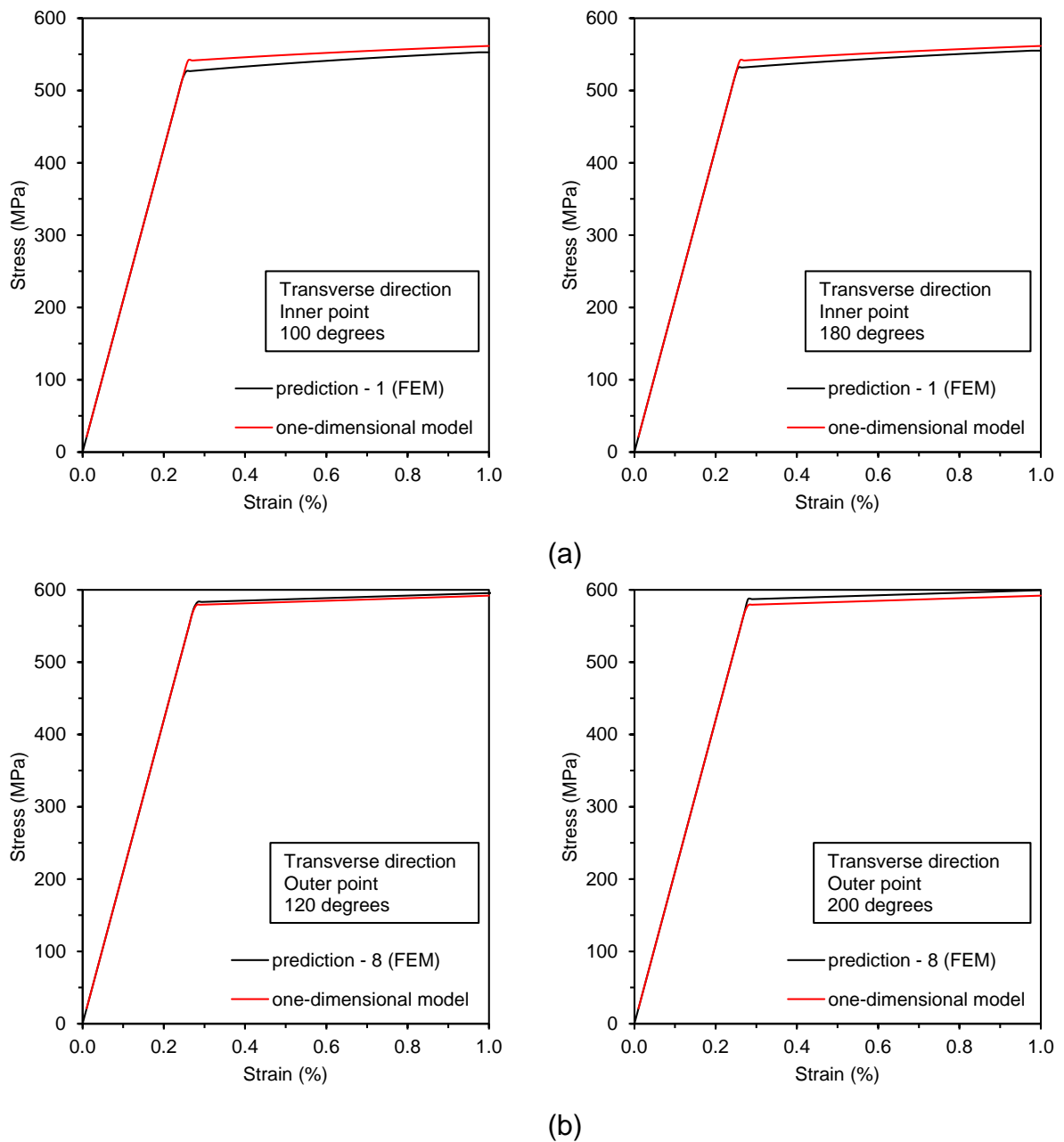


Figure 4.9: Predicted tensile stress-strain responses in the transverse direction of pipe.

#### 4.4.1 Collapse performance

For the case of  $\epsilon_E = 1.33\%$ , the collapse pressure of JCO-E pipe obtained from the idealized forming steps is evaluated performing a nonlinear analysis in ABAQUS/Standard. This collapse analysis refers to the finite element modelling of a pipe cross-section, externally pressurized under generalized plane strain conditions until it collapses. Before the application of external pressure, the pipe mean radius  $R_{m(JCO-E)}$  and the pipe thickness  $t_{JCO-E}$  are

calculated from equations (4.54) and (4.56), respectively, and the initial ovalization of pipe is considered equal to  $\Delta_0 = 0.02\%$ ; this value refers to initial ovalization of the corresponding JCO-E pipe obtained from the finite element simulation (Section 2.1). Figure 4.10 shows the geometry and the finite element mesh adopted in the collapse analysis model.

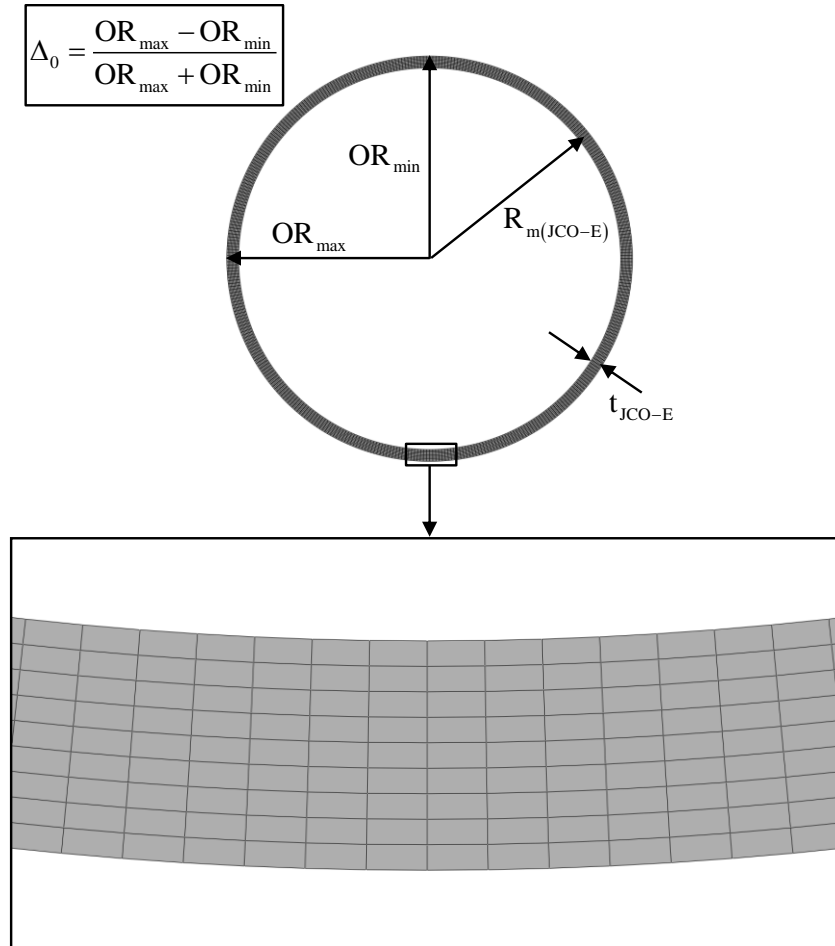


Figure 4.10: The un-deformed geometry and the finite element mesh used in collapse analysis model.

Following the determination of JCO-E pipe geometry, four different collapse calculations are performed using: (a) the residual stresses of JCO-E pipe, obtained from the idealized model, and (b) different material properties obtained from the one-dimensional model. The residual stresses of idealized JCO-E pipe constitute the “initial stresses” of the pipe in collapse analysis model; for  $\varepsilon_E = 1.33\%$ , these are shown in Figure 4.6 and Figure 4.7. In the collapse calculations, a different consideration of pipe material properties is adopted. More specifically, the pipe is assumed to have the stress-strain response: (a) of the inner point

subjected to compression (Figure 4.8a), referred to as “C-IN”, (b) of the outer point subjected to compression (Figure 4.8b), referred to as “C-OUT”, (c) of the inner point subjected to tension (Figure 4.9a), referred to as “T-IN”, (d) of the outer point subjected to tension (Figure 4.8b), referred to as “T-OUT”. For all cases, von Mises plasticity with isotropic hardening is used. The collapse pressures from the four sets of calculations are shown in Table 4.1.

Table 4.1: Collapse pressure of the pipe, obtained from the collapse analysis model

|                         | C-IN  | C-OUT | T-IN  | T-OUT |
|-------------------------|-------|-------|-------|-------|
| collapse pressure (MPa) | 12.42 | 12.37 | 12.48 | 12.50 |

For the four collapse calculations examined, and shown in Table 4.1, the absence of initial stresses (residual stresses of the pipe after the idealized steps) causes an increase in collapse pressure that ranges from 0.08% to 0.22%. The effect of initial stresses on collapse pressure is quite small, as they derived from the idealized JCO-E pipe, which has relatively small residual stresses; for  $\epsilon_E = 1.33\%$ , the maximum circumferential stress of idealized JCO-E pipe is 8.22% of the yield stress  $\sigma_y$ , which is defined in Section 3.1.4, and located at the outer point (see Figure 4.6). To evaluate the performance of the above collapse analysis, the values listed in Table 4.1 are compared with the value of 12.43MPa, which is the collapse pressure of a JCO-E pipe obtained from the finite element modelling of the corresponding JCO-E forming process ( $\epsilon_E = 1.33\%$ ). It appears that there is very good comparison between the values, given in Table 4.1, and the finite element value.

The collapse pressure predicted from the “C-IN” collapse analysis has the smallest difference compared to the numerical value 12.43MPa, and as a result, all the following numerical results refer to the collapse analysis model, where the C-IN stress-strain response is used to describe the pipe material properties. The stresses-strains developed in the transverse direction of pipe during the external pressure loading are shown in Figure 4.11. These are referred to the extreme integration points (IN, OUT) located at 3 (Figure 4.11a) and 6 (Figure 4.11b) o'clock position. Before the start of pressurization phase, the initial stress-state at these points is indicated with “A”. In Figure 4.11, state “B” indicates the circumferential stress-strain state that corresponds to the ultimate external pressure capacity. In this case where



collapse occurred, the pipe ovalization has been increased from 0.02% (initial ovalization) to 1.24%, and the inner point (IN) at the 3 o'clock position enters the plastic range.

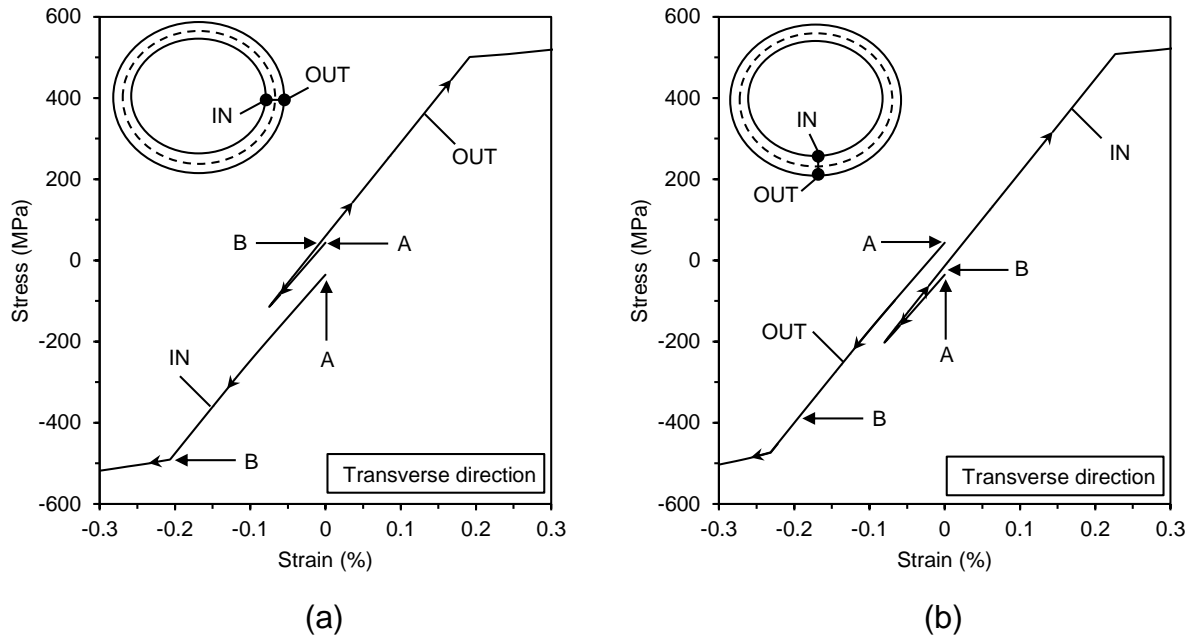


Figure 4.11: Stress-strain paths in the transverse direction of pipe during the application of external pressure.

In the above collapse analysis, the initial stresses and the material properties of JCO-E pipe have been resulted from the idealized model and the one-dimensional model, respectively, for expansion strain  $\epsilon_E = 1.33\%$ . For the case of C-IN stress-strain response, two additional scenarios for the level of expansion are examined. The objective of this short parametric study is to identify the effect of residual stresses on collapse pressure and, as a result, it is assumed that the pipe geometry is unaffected by the different expansion levels. Hence, in these collapse analyzes, the initial geometry of the pipe remains the same with initial ovalization equal to 0.02%, mean radius and thickness of the pipe taken from equations (4.54) and (4.56), respectively, considering an expansion level  $\epsilon_E = 1.33\%$ .

The first scenario refers to expansion strain  $\epsilon_E = 1.02\%$ . Using the idealized model presented in Section 4.2, the (residual) stresses at the end of JCO-E forming process are calculated; the maximum circumferential stress of JCO-E pipe is  $0.09\sigma_y$ . Inserting the final state parameters of inner point in the one-dimensional model, as described in Section 4.3, the corresponding C-IN material response is obtained. Finally, performing the collapse pressure

analysis, the calculated collapse pressure is 12.42MPa. If the initial stresses are excluded in the collapse analysis, the value of the collapse pressure is found to be 12.45MPa, which corresponds to the difference of about 0.24%. In the second scenario, the forming process of idealized JCO pipe ( $\epsilon_E = 0.00\%$ ) is considered. The maximum value of the residual circumferential stress of JCO pipe, located at the inner point and shown in Figure 4.6, corresponds to 43.14% of the yield stress  $\sigma_y$ . Considering the C-IN response of JCO pipe material, the maximum pressure capacity, as calculated from the collapse analysis, is 12.37MPa. Assuming that the residual stresses of the JCO pipe are excluded in the collapse analysis, the collapse pressure of this artificial “stress-free” JCO pipe is 12.49MPa, which is a value close to the 12.37MPa value, obtained earlier accounting for the residual stresses due to the forming steps.

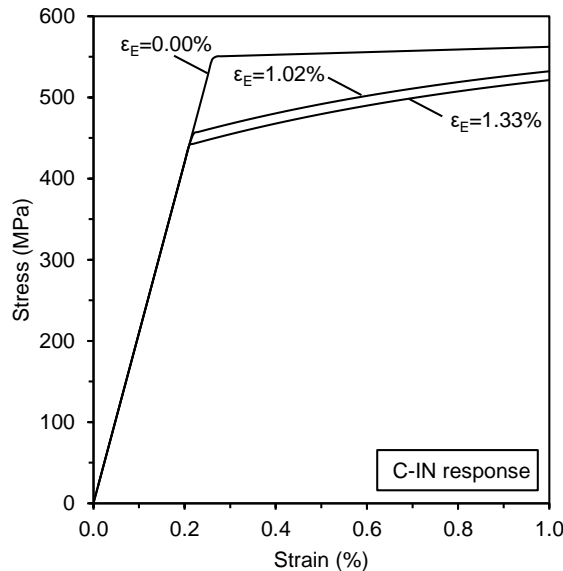


Figure 4.12: Predicted compressive stress-strain response of the inner point of the idealized JCO-E pipe wall for three cases of expansion strain.

Figure 4.12 shows the C-IN stress-strain curve of idealized JCO-E pipe material for  $\epsilon_E = 0.00\%$  (JCO pipe),  $\epsilon_E = 1.02\%$  and  $\epsilon_E = 1.33\%$ . In Figure 4.12, although the yield strength of JCO pipe material is higher than the corresponding strength of JCO-E pipe material, the collapse pressure of JCO pipe (12.37MPa) is slightly lower than that of JCO-E pipe (12.42MPa). This is attributed to the fact that the residual stresses of JCO pipe are significantly higher than those of JCO-E pipe. Therefore, if one could make a rounded JCO

pipe, its response under external pressure would not be superior to a JCO-E pipe with same geometry, and made from the same plate material.

#### 4.5 Application of idealized model to thick-walled JCO-E pipe

In idealized analytical modelling of the thick-walled JCO-E pipe, eleven points ( $k = 11$ ) are selected in the thickness direction of plate, the width and the thickness of plate correspond to those reported in Section 3.2, and the set of material parameters are shown in Table 3.6. The thickness of idealized JCO-E pipe is computed according to equation (4.56), which is shown in Figure 4.13 for different expansion levels. Furthermore, Figure 4.13 shows the average thickness of JCO-E pipe  $t_{\text{average,FEM}}$  obtained from the corresponding finite element simulation of JCO-E forming process (Section 3.2.4).

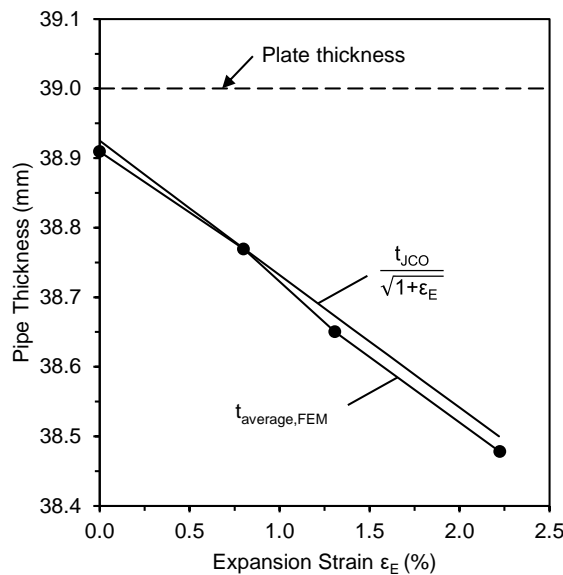


Figure 4.13: Predicted thickness of the thick-walled JCO-E pipe for different values of expansion strain, obtained from equation (4.56) and from finite element model.

Using the idealized model and considering expansion strain  $\epsilon_E = 1.70\%$ , the stress-strain history of the inner point of pipe wall in the transverse direction is depicted in Figure 4.14. A corresponding stress-strain history obtained from the finite element model is also shown in Figure 4.14, so that the differences of stress-strain paths between the idealized and finite element model can be observed. For example, at the end of idealized analysis, the

circumferential stress is approximately 0.3% of yield stress  $\sigma_y$ , while at the end of finite element analysis, the corresponding stress at the 200-degree position is approximately 10% of yield stress  $\sigma_y$ ; the definition and the value of  $\sigma_y$  are given in Section 3.2.4.

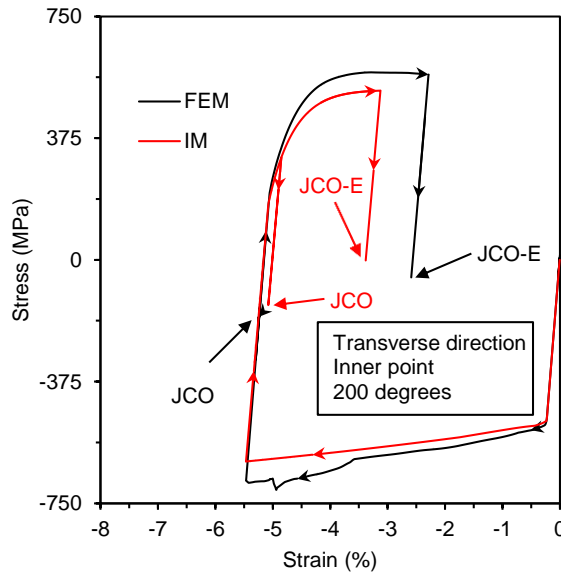


Figure 4.14: Calculated stress-strain history of the inner point of pipe wall in transverse direction for  $\epsilon_E = 1.70\%$  .

Subsequently, taking into account the residual state parameters of the inner point of idealized JCO-E pipe wall, the one-dimensional model (Section 4.3) is utilized to predict its compressive (C-IN) and tensile (T-IN) stress-strain response in transverse direction. Furthermore, the residual state parameters of the inner point of pipe wall obtained from the finite element analysis, at the 200-degree position, are used as input for assessing the C-IN and the T-IN responses, following the finite element procedure described in Section 2.5. The numerical results for the compressive C-IN and the tensile T-IN responses are shown in Figure 4.15, where the stress-strain responses of inner point calculated from one-dimensional model are identical to those computed from the above finite element procedure.

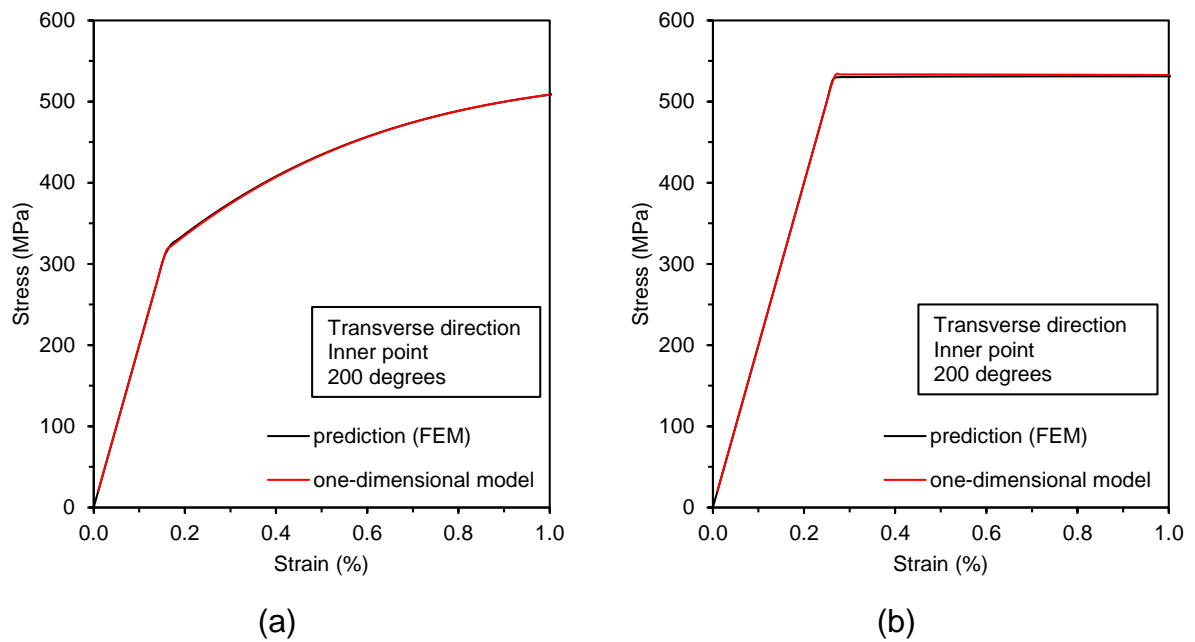


Figure 4.15: Transverse stress-strain responses of the inner point of JCO-E pipe wall; (a) under compressive, and (b) under tensile uniaxial loading.

#### 4.5.1 Collapse performance

For expansion strain  $\varepsilon_E = 1.70\%$ , the collapse pressure of idealized JCO-E pipe is predicted based on a ring collapse analysis performed in ABAQUS/Standard. Before application of external pressure, the geometry of pipe is determined by equations (4.54) and (4.56) accounting for initial ovalization  $\Delta_0 = 0.02\%$ ; the value of  $\Delta_0$  corresponds to the value of initial ovalization of JCO-E pipe calculated from the finite element model (Section 3.2.5) for expansion strain  $\varepsilon_E = 1.70\%$ . The finite element mesh and the geometry of idealized JCO-E pipe are shown in Figure 4.16. In the initial configuration, i.e. before the application of external pressure, the pipe also accounts for the residual stresses obtained from idealized model (Section 4.2) for the case of  $\varepsilon_E = 1.70\%$ .

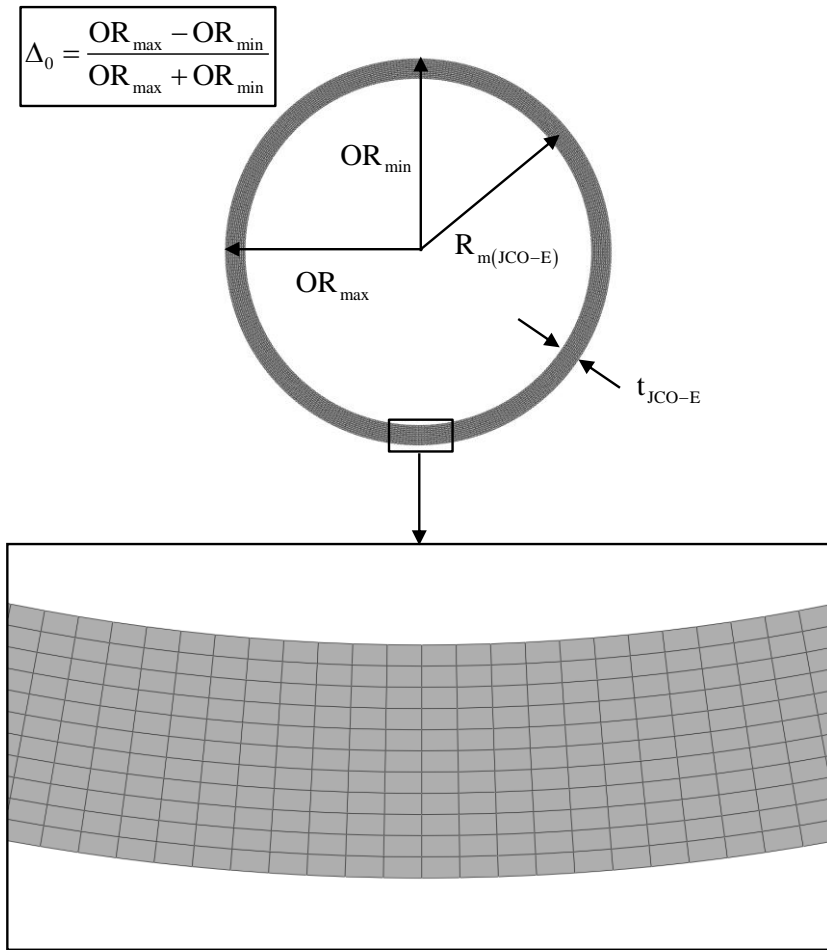


Figure 4.16: The geometry and the finite element mesh adopted in collapse analysis model.

Adopting the C-IN stress-strain response to represent the material properties, and applying external pressure under plane strain conditions, similar to Section 3.2.5, the ultimate external pressure capacity calculated from the collapse analysis model is 36.97MPa. Excluding the initial stresses from the collapse analysis, there is an increase of 0.20% with respect to the above value (36.97MPa). In contrast, the collapse analysis results in a  $P_{CO}$  value of 55.80MPa, if the T-IN response has been adopted. One can readily verify that the value of collapse pressure obtained from the collapse analysis using the C-IN response (36.97MPa) is very close to the corresponding one obtained from the finite element modelling of JCO-E forming process for  $\varepsilon_E = 1.70\%$ , where  $P_{CO} = 37.72\text{MPa}$  (see Figure 3.38). Therefore, this is a clear indication that the collapse of JCO-E pipe, under external pressure, is primarily governed by its compressive (material) response in the transverse direction.

## 4.6 Conclusions

The idealized analytical model developed in the present study has been demonstrated to be an effective tool to simulate JCO-E forming process, providing results in very good agreement with corresponding results from the finite element model. It aims at simulating the forming process of JCO-E pipe in a simple and efficient manner, significantly less computationally expensive than the finite element model. The forming steps of the simplified model, described in Section 4.2, are capable of reproducing the stresses-strains at specific points through the JCO-E pipe thickness, which are in accordance with the finite element model.

After the idealized analytical simulation of the cold forming process, and taking into account the state parameters of any point across the thickness of the pipe, its response under uniaxial loading can be evaluated using a simple one-dimensional model (Section 4.3), so that its mechanical properties are identified. This latter model simulates the uniaxial test of a circumferential coupon extracted from a part of the JCO-E pipe wall (pipe material characterization). The predicted mechanical properties obtained at several locations of the pipe agree very well with those obtained by the corresponding rigorous finite element analysis (Section 2.5).

Furthermore, the collapse pressure of a pipe formed by the idealized JCO-E process can be evaluated by performing a standard collapse analysis in a ring model under uniform external pressure, without the bulk of information associated with the manufacturing process. Instead of this detailed information, in this collapse analysis, one should provide: (a) the geometry of idealized JCO-E pipe, including a value for its initial ovalization, (b) the initial stresses corresponding to those obtained from the idealized JCO-E pipe, and (c) the compressive stress-strain response of idealized JCO-E pipe material. In the present study, the value of initial ovalization used in the ring model is considered equal to the initial ovalization calculated from the rigorous finite element simulation of JCO-E forming process, for the expansion strain  $\varepsilon_E$  that corresponds to the one of idealized JCO-E pipe; alternatively, one could utilize the initial ovalization of the actual JCO-E pipe. Comparisons with the collapse pressure predicted from the finite element simulation, indicated that the compressive stress-strain curve of the inner point of pipe wall (C-IN) provide the best results.

## **Chapter 5 - Summary and Conclusions**

The present thesis focuses on the simulation of JCO-E pipe process, and its effect on residual stresses, geometry and material properties of the line pipe product. Furthermore, the numerical results of this simulation are aimed at predicting in a direct manner the strength of JCO-E pipe against external pressure, which is a parameter of major importance relating to the design of offshore applications. For reliable predictions, an essential issue is the development of a suitable constitutive model for describing the elastic-plastic behavior of raw material during JCO-E process. Herein, an improvement of the constitutive model capabilities used in previous works [6], [18] for the special case of an isotropic plate (raw) material is developed, so that the anisotropy of plate material can be taken into account. The numerical implementation of this special-purpose anisotropic cyclic plasticity (constitutive) model with combined hardening is presented in detail, using an Euler-backward (implicit) integration scheme. Furthermore, the review indicates that uniaxial tests have to be conducted on specimens extracted from both the raw material and the as-fabricated line pipe product. Simulations of these tests need to be performed to calibrate the parameters of constitutive model, and verify the efficiency of JCO-E process simulation, respectively.

In the present research, the above predictions can be obtained using: (a) a finite element methodology, or (b) an idealized model. In the first case, a two-dimensional generalized plane strain model is developed to simulate the JCO-E forming stages, employing input data from the pipe mill. The simulation of welding (SAW) process can also be performed through an auxiliary finite element analysis, which is coupled with the quasi two-dimensional model. It is important to underline that the present finite element model enables the collapse prediction of the JCO-E pipe using the same model, which takes into account rigorously the effects of its fabrication process. Apart from the finite element simulation of JCO-E fabrication process, a simple and efficient numerical tool is presented, where the JCO-E forming steps are simulated through an idealized model. This model may be useful for



preliminary studies on the production of an arbitrary D/t line pipe. The idealized model provides predictions of the geometry, the residual stresses, and the material properties of JCO-E pipe, for several expansion levels, in a simple and unified manner; these predictions are associated with the strength of pipe against external pressure.

In Chapter 2, the finite element methodology is applied first to the JCO-E manufacturing (forming and the SAW welding) of a “relatively thin-walled” X65 pipe, using the input data provided by the pipe mill. Two sets of constitutive model parameters (MAT1, MAT2) have been examined. The choice of these parameters is not a trivial issue, because it has been demonstrated to affect the geometry, the final material properties and the collapse pressure of the line pipe product. Hence, the finite element simulation of JCO-E manufacturing process is conducted selecting the set that provides a better compromise between predictions and experimental results of the pipe material (MAT1). At the end of simulation, the JCO-E pipe is subjected to uniform external pressure to predict the collapse pressure. It is concluded that the value of collapse pressure is not significantly affected by: (a) the presence of welding residual stresses-strains, and (b) the range of anisotropy that characterizes the plate material.

Subsequently, and based on the above conclusion for the effect of welding on collapse pressure of the “relatively thin-walled pipe”, the finite element methodology is applied to the JCO-E forming process of a “thick-walled” X60 pipe, using the forming parameters provided by the pipe mill, and without taking into account the simulation of welding (SAW) process. For the adopted set of material parameters, the predicted stress-strain behaviors of the pipe material, in terms of stress-strain curves, are in good agreement with the ones measured experimentally. In addition, the effect of JCO punching steps on collapse is rather small for the consideration reported in Section 3.2.6. The following major conclusions can be drawn from the above applications, using the finite element methodology:

- The JCO-E fabrication process induces changes in the mechanical properties of plate material, which affect the collapse performance of the as-fabricated pipe product.
- The thickness of JCO pipe is almost reduced linearly in proportion to expansion level.
- The expansion stage reduces the residual stresses and the initial ovalization of JCO pipe. Simultaneously, expansion reduces the compressive strength of JCO pipe, due to Bauschinger effect. Therefore, from the point of view of collapse, JCO-E pipe is

superior to JCO pipe up to a specific expansion level (optimum expansion). Beyond that level, the degradation of the compressive strength of pipe material overshadows the improvement in initial ovalization and the minimization of residual stresses.

- The collapse pressure of the JCO-E pipes predicted from the finite element simulation is quite higher than that predicted by relevant design standards.
- The developed finite element analysis can be used for optimizing the JCO-E fabrication process in terms of the structural performance of pipe, quantified with the value of the collapse pressure.

In the last part of the study, a strain-based idealized model is developed for the simulation of JCO-E forming process. The idealized model provides quicker and similar predictions compared to corresponding predictions obtained from the rigorous finite element model. Finally, taking into account the results obtained from the idealized model, the collapse pressure of JCO-E pipe can be predicted in a simple and efficient manner, performing a standard collapse analysis in a ring-type finite element model under external pressure, bypassing the finite element simulation of forming process.

To extend the results of the present thesis on the simulation of JCO-E process the following topics are suggested for future investigation:

- Conduct a three-dimensional simulation of the actual line pipe fabrication, to investigate global distortions caused by the multi-electrode (SAW) welding process, as well as the effects of gradual expansion of the pipe on geometry and collapse of JCO-E pipe; in the pipe mill, the expansion process is performed step-by-step along the pipe length.
- Investigate the performance of other plasticity models on the prediction of material properties and collapse. The plasticity model used in the present research belongs to the category of “coupled models”, where the plastic modulus is defined through the consistency property of the flow rule. Recent works of our research team on the so-called “uncoupled models”, in which the plastic modulus is defined explicitly, offers some advantages in describing inelastic response under reverse loading and may describe the material stress-strain response closer to experimental stress-strain curves.
- Investigate the positive effect of heat-treatment due to coating process, which usually takes place after expansion process, on the external pressure capacity of the as-

fabricated JCO-E pipe. This study may be facilitated performing compression tests on specimens extracted from JCO-E pipe, before and after coating process; in the present thesis, it has been shown that the compressive material properties of an as-fabricated JCO-E pipe is strongly related to its collapse pressure.

## References

- [1] Chandel, J. D. and N. L. Singh (2011) “Formation of X-120 M Line Pipe through J-C-O-E Technique”, *Engineering*, 3, 400-410.
- [2] Kyriakides, S. and E. Corona (2007) *Mechanics of Offshore Pipelines, Buckling and Collapse*, 1, Elsevier.
- [3] Timoshenko, S. and J.M. Gere (1961) *Theory of Elastic Stability*, 2<sup>nd</sup> Edition, McGraw-Hill, New York.
- [4] Murphey, C.E. and Langner, C.G. (1985) “Ultimate Pipe Strength Under Bending, Collapse and Fatigue”, *Proceedings of the 4th International Conference on Offshore Mechanics and Arctic Engineering*, 1, 467–477, Dallas, USA.
- [5] Kyriakides, S., Corona, E. and F. J. Fischer (1991) “On the Effect of the UOE Manufacturing Process on the Collapse Pressure of Long Tubes”, *Offshore Technology Conference*, 4, 531–543, Houston, Texas.
- [6] Chatzopoulou, G., Karamanos, S. A. and G. E. Varelis (2016) “Finite Element Analysis of UOE Manufacturing Process and its Effect on Mechanical Behavior of Offshore Pipes”, *International Journal Solids and Structures*, 83, 13–27.
- [7] DNVGL-ST-F101 STANDARD (2017) “Submarine Pipeline Systems”, DNVGL, Oslo, Norway.
- [8] API Recommended Practice 1111 (1999) “Design, Construction, Operation and Maintenance of Offshore Hydrocarbon Pipelines (Limit State Design)”, American Petroleum Institute, Washington, DC, USA.
- [9] Gresnigt, A.M., Van Foeken, R.J. and S. Chen (2000) “Collapse of UOE Manufactured Steel Pipes”, *Proceedings of the Tenth International Offshore and Polar Engineering Conference*, 2, 170-181, Seattle, Washington.

- [10] DeGeer, D. and J.J. Cheng (2000) “Predicting Pipeline Collapse Resistance”, *International Pipeline Conference*, Alberta, Canada.
- [11] Herynk, M.D., Kyriakides, S., Onoufriou, A. and H.D. Yun (2007) “Effects of the UOE/UOC Pipe Manufacturing Processes on Pipe Collapse Pressure”, *International Journal of Mechanical Sciences*, 49, 533–553.
- [12] Toscano, R. G., Raffo, J., Mantovano, L., Fritz, M. and R. C. Silva (2007) “On the Influence of the UOE Process on Collapse and Collapse Propagation Pressure of Steel Deep-Water Pipelines under External Pressure”, *Offshore Technology Conference*, Houston, Texas.
- [13] Fan, L. F., Yan, J. X., Gao, Y. and J. B. Yun (2016) “Research on Deformation Characteristics of JCOE Forming in Large Diameter Welding Pipe”, *Advances in Manufacturing*, 4, 268–277.
- [14] Gao, Y., Li, Q. and L. Xiao (2009) “Numerical Simulation of JCO/JCOE Pipe Forming”, *World Congress on Computer Science and Information Engineering*, Los Angeles, CA, USA.
- [15] Kathayat, T., Goyal, R. and Shant, J. (2014) “Collapse Behavior of As-Fabricated & Thermal Aged JCOE Line Pipe - Experimental Study by External Pressure Ring Collapse Testing and FE Analysis”, *Offshore Technology Conference*, Asia, Kuala Lumpur.
- [16] Krishnan, V.R. and D.A. Baker (2014) “Enhanced Collapse Resistance of Compressed Steel Pipes”, *Proceedings of the 33rd International Conference on Ocean, Offshore and Arctic Engineering*, San Francisco, California, USA.
- [17] Reichel, T., Pavlyk, V., Beissel, J., Kyriakides, S. and W.Y., Jang (2011) “New Impander Technology for Improved Collapse Resistance of Large Diameter Pipe for Deepwater Applications”, *Offshore Technology Conference*, Houston, Texas.
- [18] Antoniou, K., Chatzopoulou, G., Karamanos, S. A., Tazedakis, A., Palagas, C. and E. Dourdounis (2019) “Numerical Simulation of JCO-E Pipe Manufacturing Process and Its Effect on the External Pressure Capacity of the Pipe”, *ASME Journal of Offshore Mechanics and Arctic Engineering*, 141 (1).

- [19] Kojic, M., Grujovic, N., Slavkovic, R. and M. Zivkovic (1996) “A General Orthotropic Von Mises Plasticity Material Model with Mixed Hardening: Model Definition and Implicit Stress Integration Procedure”, *Journal of Applied Mechanics*, 63 (2), 376-382.
- [20] Hill, R. (1950) *The Mathematical Theory of Plasticity*, Oxford University Press, London.
- [21] Armstrong, P.J. and C.O. Frederick (1966) “A mathematical representation of the multiaxial Bauschinger effect”, *Materials at High Temperatures*, 24 (1), 1-26.
- [22] Abaqus Analysis User’s Guide, Version 6.14, Dassault Systèmes Simulia Corp., Providence, RI.
- [23] Wen, S.W., Hilton, P. and D.C.J. Farrugia (2001) “Finite Element Modelling of a Submerged Arc Welding Process”, *Journal of Materials Processing Technology*, 119, 203-209.
- [24] Horn, T. (2003) *Cyclic Plastic Deformation and Welding Simulation*, Doctoral Thesis, Faculty of Materials Science, Delft University of Technology Press.
- [25] Ren, Y. (2018) *Investigation of Residual Stresses in X65 Narrow-Gap Pipe Girth Welds*, PhD Thesis, Department of Mechanical, Aerospace and Civil Engineering, Brunel University London.
- [26] ISO/TR 17671-1 (2002) “Welding – Recommendations for Welding of Metallic Materials”, International Standardization Organization (ISO), Geneva, Switzerland.
- [27] Goldak, J., Chakravarti, A. and M. Bibby (1984) “A New Finite Element Model for Welding Heat Sources”, *Metallurgical Transactions B*, 15, 229-305.
- [28] Yaghi, A. H., Tanner, D. W. J., Hyde, T. H., Becker, A. A. and W. Sun (2012) “Finite element thermal analysis of the fusion welding of a P92 steel pipe”, *Mechanical Sciences*, 3, 33-42.
- [29] Bai, Y. and Q. Bai (2005) *Subsea Pipelines and Risers*, Elsevier.
- [30] Bang, I.W., Son, Y.P., Oh, K.H., Kim, Y.P. and W.S. Kim (2002) “Numerical Simulation of Sleeve Repair Welding of In-Service Gas Pipelines”, *Welding Journal*, 81, 273–282.
- [31] Stahl-Eisen-Prüfblätter (2006) “Testing and Documentation Guideline for the Experimental Determination of Mechanical Properties of Steel Sheets for CAE-

Calculations”, SEP 1240, Research Association for Steel Application, Wuppertal/Germany.

- [32] ISO 6892-1 (2016) “Metallic Materials - Tensile Testing - Part 1: Method of Test at Room Temperature”, International Standardization Organization (ISO), Geneva, Switzerland.
- [33] Nezamdost, M. R., Nekouie Esfahani, M. R., Hashemi, S. H. and S. A. Mirbozorgi (2016) “Investigation of Temperature and Residual Stresses Field of Submerged Arc Welding by Finite Element Method and Experiments”, *International Journal of Advanced Manufacturing Technology*, 87, 615–624.
- [34] Brush, D. O. and B., O. Almroth (1975) *Buckling of Bars, Plates, and Shells*, McGraw-Hill, New York.